

## Perspectives on SARS-CoV-2 Main Protease Inhibitors

Kaifu Gao, Rui Wang, Jiahui Chen, Jetze J. Tepe, Faqing Huang, and Guo-Wei Wei\*

Cite This: *J. Med. Chem.* 2021, 64, 16922–16955

Read Online

ACCESS |



Metrics &amp; More

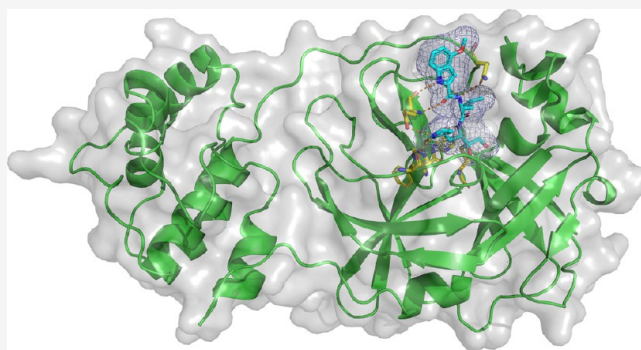


Article Recommendations



Supporting Information

**ABSTRACT:** The main protease ( $M^{pro}$ ) plays a crucial role in severe acute respiratory syndrome coronavirus 2 (SARS-CoV-2) replication and is highly conserved, rendering it one of the most attractive therapeutic targets for SARS-CoV-2 inhibition. Currently, although two drug candidates targeting SARS-CoV-2  $M^{pro}$  designed by Pfizer are under clinical trials, no SARS-CoV-2 medication is approved due to the long period of drug development. Here, we collect a comprehensive list of 817 available SARS-CoV-2 and SARS-CoV  $M^{pro}$  inhibitors from the literature or databases and analyze their molecular mechanisms of action. The structure–activity relationships (SARs) among each series of inhibitors are discussed. Additionally, we broadly examine available antiviral activity, ADMET (absorption, distribution, metabolism, excretion, and toxicity), and animal tests of these inhibitors. We comment on their druggability or drawbacks that prevent them from becoming drugs. This Perspective sheds light on the future development of  $M^{pro}$  inhibitors for SARS-CoV-2 and future coronavirus diseases.



## 1. INTRODUCTION

Developing effective drugs or therapies against severe acute respiratory syndrome coronavirus 2 (SARS-CoV-2) is an urgent task for scientific and pharmaceutical communities. SARS-CoV-2 has an unprecedented high infection and prevalence rate, as well as a long incubation period.<sup>1</sup> Up to October 5, 2021, 236 million SARS-CoV-2 cases had already brought 4.8 million deaths worldwide. This reminds us that although 21 distinct SARS-CoV-2 vaccines have already been approved for full or emergency use globally,<sup>2</sup> the battle against SARS-CoV-2 is still far from the end because of various vaccine escape mutations on the spike protein.<sup>3</sup> In comparison, mutations on enzyme active sites are rare.<sup>4</sup> Thus, to finally control SARS-CoV-2 and return to normalcy, we must develop effective medications against the virus.

However, there is no approved SARS-CoV-2 medication due to the inherently long period of drug discovery. Pfizer has released two drug candidates PF-07321332 and PF-07304814 inhibiting the SARS-CoV-2 main protease ( $M^{pro}$ ), which are now in clinical trials.<sup>5,6</sup> Notably, PF-07321332 is now in phase 3 clinical trials and appears to be on its way to becoming the first  $M^{pro}$  drug to treat SARS-CoV-2. Traditionally, developing a new drug can take about 10–15 years,<sup>7</sup> from initial design to entering the marketplace. Considering the urgency of the current pandemic, the drug discovery for SARS-CoV-2 must be expedited.

SARS-CoV-2 is a  $\beta$ -coronavirus belonging to the Coronaviridae family.  $\beta$ -Coronaviruses seriously threaten human health. During the first two decades of the 21st century alone,  $\beta$ -

coronaviruses have triggered three major outbreaks of deadly pneumonia: SARS-CoV (2002), Middle East respiratory syndrome coronavirus (MERS-CoV) (2012), and SARS-CoV-2 (2019).<sup>8</sup> SARS-CoV-2's infection rate is even higher than SARS-CoV and MERS-CoV.<sup>9,10</sup>

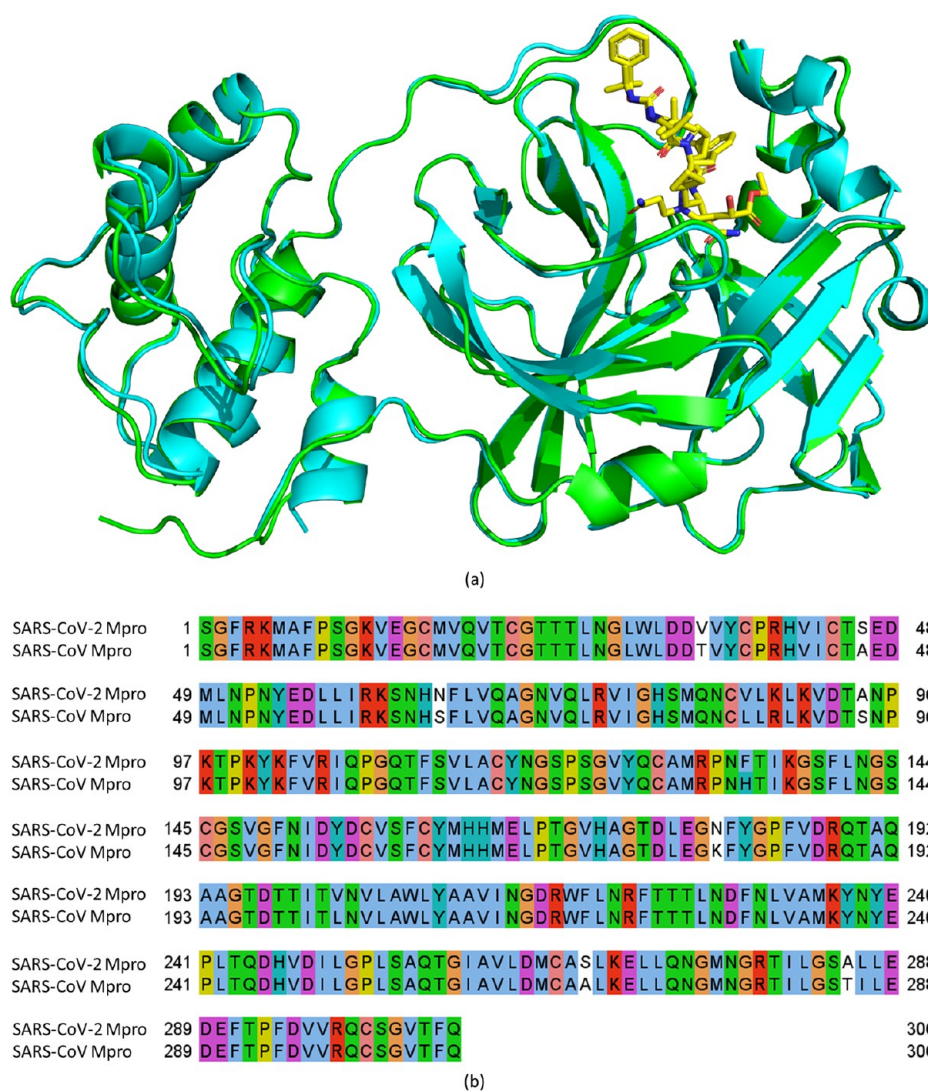
A great number of drug targets of SARS-CoV-2 have been identified.<sup>11</sup> Among them,  $M^{pro}$ , also called 3-chymotrypsin-like protease ( $3CL^{pro}$ ), is an attractive target for small-molecule inhibitors.<sup>12–20</sup>

First,  $M^{pro}$  is an indispensable enzyme for viral replication and transcription. Coronaviruses possess the largest known RNA genomes with a length of about 30 kb.<sup>21</sup> Their genomes consist of multiple open-reading frames (ORFs). Among them, two overlapping ORFs (ORF1a and ORF1ab) are translated into two large polyproteins, pp1a and pp1ab, via a  $-1$  translation frameshift mechanism. Then,  $M^{pro}$  and papain-like protease ( $PL^{pro}$ )<sup>22</sup> cleave pp1a and pp1ab into 16 mature nonstructural proteins (NSPs).<sup>23</sup>  $M^{pro}$  formed from NSP5 cleaves the two polyproteins at 11 recognition sites and creates NSP4 to NSP10 and NSP12 to NSP16 (NSP11 is the N terminal end of NSP12), while  $PL^{pro}$  cleaves the other 3 sites to generate NSP1 to NSP3. Notably, NSP4 to NSP16 cleaved by  $M^{pro}$  contain many

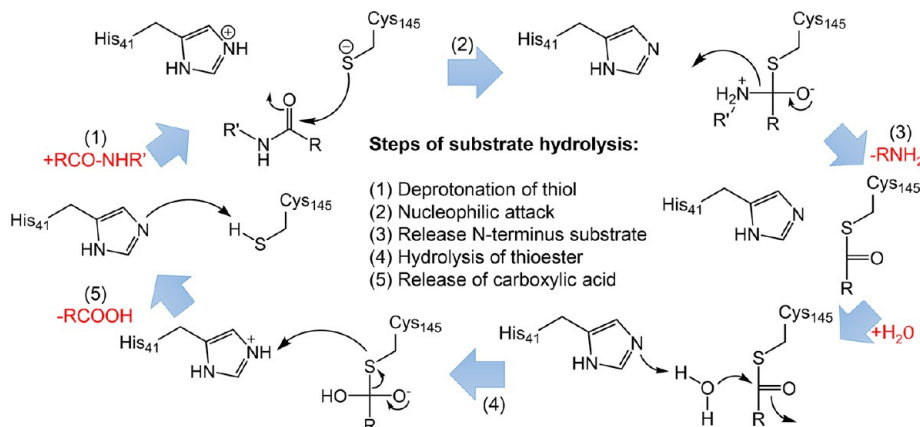
Received: March 7, 2021

Published: November 19, 2021





**Figure 1.** 3D conformation alignment (a) and 2D sequence alignment (b) of SARS-CoV-2 and SARS-CoV main proteases ( $M^{pro}$ ). The sequences and structures are from the Protein Data Bank (PDB) ID 7C6S (SARS-CoV-2  $M^{pro}$ , cyan in part a) and 2A5I (SARS-CoV  $M^{pro}$ , green in part a).



**Figure 2.** Overall scheme of SARS-CoV/SARS-CoV-2  $M^{pro}$  catalytic mechanism by Cys145 and His41 at the active site.

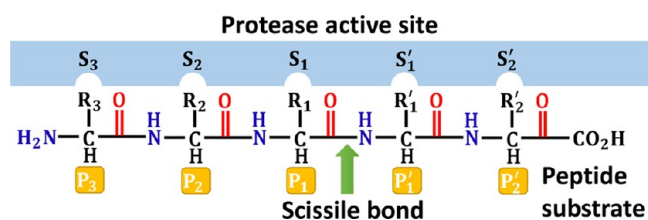
essential viral proteins, especially the RNA-dependent RNA polymerase (NSP12), RNA binding proteins (NSP9), helicase (NSP13), exoribonuclease (NSP14), and methyltransferase (NSP16).<sup>24,25</sup> Therefore, effectively blocking  $M^{pro}$  could stop SARS-CoV-2 replication in human bodies and cure the disease.

Second, according to the data from the global initiative on sharing all influenza data (GISAID), SARS-CoV-2  $M^{pro}$  is highly conserved. The mutation rate on its binding domain is lower than 0.001 (see section 3.2). Thus, mutations will not broadly impact the efficacy of SARS-CoV-2  $M^{pro}$  inhibitors.

Last but not least, the M<sup>Pro</sup> enzymes of SARS-CoV-2 and SARS-CoV share a very high 2D sequence identity of 96.1% and a very low 3D RMSD of 0.42 Å (see Figure 1). Their binding-site sequence identity is even as high as 100%.<sup>26</sup> Therefore, previous SARS-CoV M<sup>Pro</sup> inhibitors are still effective against SARS-CoV-2 M<sup>Pro</sup>, providing a useful resource for developing SARS-CoV-2 M<sup>Pro</sup> drugs. For instance, PF-00835231, a SARS-CoV-2 M<sup>Pro</sup> inhibitor currently in clinical trials, was originally designed by Pfizer during the 2002–2003 outbreak of SARS-CoV to target SARS-CoV M<sup>Pro</sup>.<sup>6</sup>

The active site of SARS-CoV-2 and SARS-CoV M<sup>Pro</sup> consists of Cys145 and His41, which form a catalytic dyad. Cys145 is the common nucleophile in the proteolytic process.<sup>17,27</sup> Figure 2 depicts the five-step process of M<sup>Pro</sup> hydrolyzing a substrate. The first step is the deprotonation of the Cys145-thiol, in which the proton of Cys145-thiol is transferred to His41. In the second step, the resulting anionic sulfur nucleophilically attacks the substrate carbonyl carbon to form a C–S bond. Then, in the third step, the peptide substrate is protonated and cleaved, and the product with an amino terminus is released, leaving the His41 in its deprotonated form. Next, in the fourth step, the resulting thioester is hydrolyzed to release a carboxylic acid. In the last step, the free enzyme is formed again.

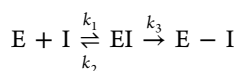
The subsite nomenclature is a popular representation of a proteolytic enzyme and its interactions with a peptide substrate or inhibitor (Figure 3). From N-terminus to C-terminus, the



**Figure 3.** Subsite nomenclature for proteolytic enzymes. Amino acid residues to the left of the polypeptide scissile amide bond are numbered sequentially, beginning with P<sub>1</sub> and increasing toward the N-terminus. Amino acid residues to the right of the scissile bond are numbered sequentially, beginning with P<sub>1</sub>' and increasing toward the C-terminus. Complementary regions of the protease active site employ the corresponding S numbering.

amino acids in a substrate are numbered as P<sub>3</sub>, P<sub>2</sub>, P<sub>1</sub>, P<sub>1</sub>', P<sub>2</sub>', etc. The amide bond between P<sub>1</sub> and P<sub>1</sub>' represents the scissile bond, where peptide substrates are hydrolyzed.<sup>17</sup> The protease active sites are correspondingly numbered as S<sub>3</sub>, S<sub>2</sub>, S<sub>1</sub>, S<sub>1</sub>', and S<sub>2</sub>'. This work adopts this subsite nomenclature.

Notably, for covalent inhibitors of SARS-CoV-2 and SARS-CoV M<sup>Pro</sup>, the kinetic scheme of covalent inhibition is illustrated as follows:



where E, I, EI, and E–I represent enzyme, inhibitor, enzyme–inhibitor complex, and covalently bonded enzyme and inhibitor, respectively. At first, the inhibitor binds to the protease noncovalently. Then, a nucleophilic attack by Cys145 triggers the protease to form a stable covalent bond with the inhibitor.<sup>28,29</sup> Therefore, the rate of the interaction is determined by both the equilibrium-binding constant  $k_i$  (designated as  $k_1/k_2$ ) and the inactivation rate constant for covalent bond formation  $k_3$ . For a covalent inhibitor, the

reported binding affinity refers to the one from the noncovalent binding in the first step.

Additionally, the existing crystal structures of SARS-CoV-2 M<sup>Pro</sup> and inhibitor complexes reveal many inhibitor binding sites. However, the major inhibitory site is at the enzyme catalytic center.<sup>30</sup>

Motivated by the pressing need for effective SARS-CoV-2 medications and the data in machine learning-based drug repositioning and generation for M<sup>Pro</sup> inhibitors,<sup>30–32</sup> we collected 817 available SARS-CoV-2 and SARS-CoV M<sup>Pro</sup> inhibitors from the literature or databases in this Perspective. The inhibitors with enzyme inhibitory activities in sub-micromolar range are highlighted. We classify these inhibitors into different categories based on their binding mechanisms and illustrate their covalent or noncovalent binding interactions with M<sup>Pro</sup>. In each category, the structure–activity relationship (SAR) of the inhibitors and the potential path to improve potency are analyzed. Since the antiviral activities of the inhibitors are also critical, we analyze their antiviral potentials and the relationships with enzymatic activities. Moreover, we analyze their ADMET (absorption, distribution, metabolism, excretion, and toxicity), pharmacokinetics (PK), druggability data, and *in vivo* results, when available. More importantly, we comment on their druggable potential and possible issues preventing them from becoming drugs. Finally, we forecast the M<sup>Pro</sup> mutation impact on inhibitor efficacy as well. The data collection and perspectives in this work will provide a starting point to screen and discover drug candidates against SARS-CoV-2 M<sup>Pro</sup>.

## 2. SARS-COV-2 AND SARS-COV M<sup>PRO</sup> INHIBITORS WITH INHIBITORY POTENCY IN SUB-MICROMOLAR RANGE

### 2.1. Peptidomimetic Covalent Inhibitors. 2.1.1. Ketone-Based Covalent Inhibitors.

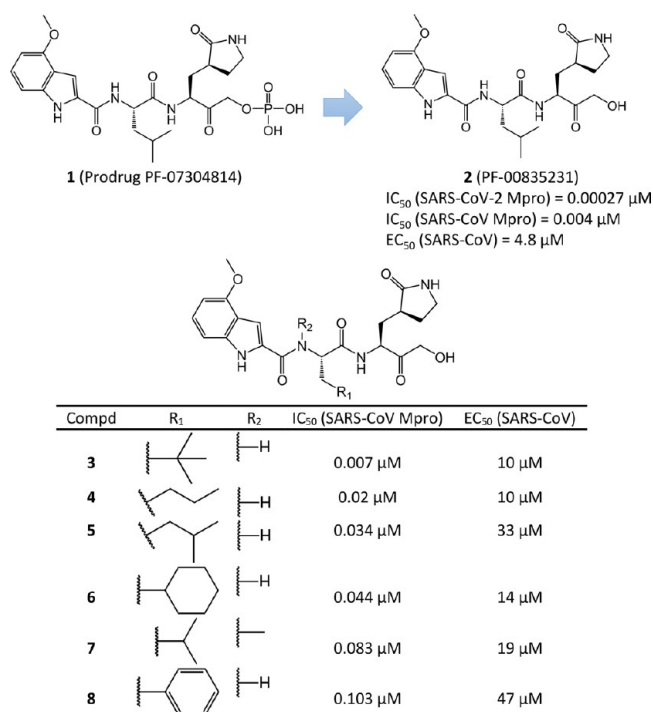
So far, the SARS-CoV-2 and SARS-CoV M<sup>Pro</sup> inhibitors with the strongest enzyme inhibitory activities are among the ketone-based covalent inhibitors developed by Hoffman et al. from Pfizer,<sup>26</sup> especially the P<sub>2</sub>-modified hydroxymethylketone (HMK) inhibitors.

#### 2.1.1.1. P<sub>2</sub>-Modified Hydroxymethylketone (HMK) Inhibitors.

A series of P<sub>2</sub>-modified HMK inhibitors developed by Hoffman et al.<sup>26</sup> show strong inhibition of SARS-CoV-2 and SARS-CoV M<sup>Pro</sup> (Figure 4). HMKs are reversible cysteine protease inhibitors.

Notably, among them, 2 (PF-00835231) is the most potent SARS-CoV-2 and SARS-CoV M<sup>Pro</sup> inhibitor in enzymatic assays so far. Actually, PF-00835231 is the active metabolite of its prodrug PF-07304814 (1). PF-07304814 contains a phosphate group to improve the solubility of the compound. After entering into tissues, the phosphate group is cleaved by alkaline phosphatase enzymes and active antiviral PF-00835231 is released. Pfizer chemists originally designed it to target SARS-CoV M<sup>Pro</sup> during the 2002–2003 outbreak of SARS-CoV. At the end of the 2003 pandemic, its clinical advancement was suspended. Recently, the prodrug PF-07304814 completed a phase 1 clinical trial to treat SARS-CoV-2. PF-00835231 demonstrates efficacy against multiple strains of SARS-CoV-2 as a single agent and even demonstrates additive/synergistic activity in combination with remdesivir. Its drawbacks include its route of administration (intravenously) and its relatively high effective dose.<sup>6</sup>

PF-00835231 has an IC<sub>50</sub> of 0.004 μM against SARS-CoV M<sup>Pro</sup>. A recent survey reported even higher efficacy against



**Figure 4.** P<sub>2</sub>-modified hydroxymethylketone (HMK) covalent inhibitors.

SARS-CoV-2 M<sup>Pro</sup> with an IC<sub>50</sub> of 0.00027 μM.<sup>26</sup> However, its antiviral activity toward SARS-CoV is much lower, with an EC<sub>50</sub> of 4.8 μM. Other *in vitro* and *in vivo* assays indicated that PF-00835231 possesses high metabolic stability in liver microsomes (half-life time = 107 min), acceptable solubility (4.6 mg/mL), and low clearance (20.6 (mL/min)/kg in monkeys).

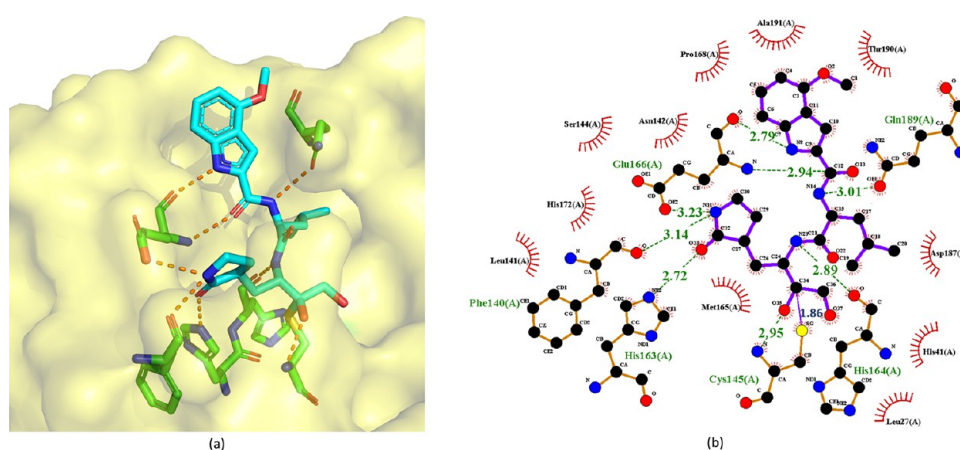
The crystal structures of 2 bound to the SARS-CoV-2 M<sup>Pro</sup> and SARS-CoV-2 M<sup>Pro</sup> were solved at 1.47 and 1.26 Å resolutions (PDB ID 6XHL and 6XHM, respectively).<sup>26</sup> As expected, since the ligand-binding domains of SARS-CoV-2 M<sup>Pro</sup> and SARS-CoV-2 M<sup>Pro</sup> are highly conserved, their interactions with 2 are also very similar. Figure 5 shows the covalent adduct of 2 with SARS-CoV-2 M<sup>Pro</sup>. The electrophilic carbonyl C atom of 2 forms a covalent bond with the S atom of the M<sup>Pro</sup> active-site Cys145, which leads to a tetrahedral hemithioacetal adduct (The C–S bond is 1.86 Å). Bridged by a water molecule, hydrogen bonds

are formed between the carbinol hydroxyl of 2 and the amide NH group of Gly143, as well as the backbone NH group of Cys145. Another essential hydrogen bond is between the primary alcohol moiety of the compound and catalytic His41. Additionally, the lactam carbonyl of 2 forms a strong hydrogen bond (2.72 Å) with the side chain of His163. The NH and C2-carbonyl of the indole in the compound interact with the backbone carbonyl and NH of Glu166 via β-sheet-like hydrogen bonds. The NH group of its P<sub>2</sub> Leu accepts a hydrogen bond (3.01 Å) from the side chain of Gln189. Another NH group of 2 also has a strong hydrogen bond (2.89 Å) with the backbone carbonyl of His164.

Hoffman et al. also analyzed the structure–activity relationship (SAR) of these inhibitors. Notably, as revealed by Figure 4, 7 and 2 only differ by a CH<sub>3</sub> group at the P<sub>2</sub> site. However, the binding affinity of 7 is largely attenuated (IC<sub>50</sub> from 0.004 μM to 0.083 μM). The explanation is, first, in the crystal structure in Figure 5, the NH group at the P<sub>2</sub> site of 2 has a hydrogen bond with the side-chain amide of Gln189, but the CH<sub>3</sub> substitution in 7 prevents the formation of this hydrogen bond. Second, this CH<sub>3</sub> substitution deforms the 4-methoxy indole cap and, thus, perturbs the whole M<sup>Pro</sup>–ligand hydrogen bond network present in 2. Other potency reduction from 3 to 6 and 8 suggests a preference of smaller groups at the P<sub>2</sub> moiety (the R<sub>1</sub> group in Figure 4). This is probably because the S<sub>2</sub> pocket of M<sup>Pro</sup> more easily accommodates smaller groups as seen from the crystal structure in Figure 5. Larger groups could lead to spatial contradiction and thus loosen the binding.

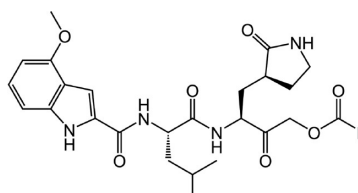
The antiviral activities of 2–8 reported by Hoffman et al.<sup>26</sup> in terms of EC<sub>50</sub> are shown in Figure 4 as well. It turns out that 2 has the lowest IC<sub>50</sub> as well as the lowest EC<sub>50</sub>. These data also indicate that the antiviral EC<sub>50</sub>/enzyme IC<sub>50</sub> ratios of 2–8 are high due to poor cell permeability. These HMK inhibitors exhibit very low permeability and high levels of efflux beyond the sensitivity of the Caco-2 *in vitro* assay. Currently, efforts to reduce efflux by active transporters, such as P-glycoprotein, are being attempted to decrease high EC<sub>50</sub>/IC<sub>50</sub> ratios. An analysis of the physicochemical properties of 2 suggests that increasing log *P*, reducing polar surface area, and reducing the number of hydrogen bond donors and acceptors are feasible strategies to improve its cellular permeability and reduce efflux.<sup>26</sup>

**2.1.1.2. Acyloxymethylketone Inhibitors.** Substituting the hydroxyl group of a HMK inhibitor with an acyloxy group results



**Figure 5.** Cocrystal structure of the covalent adduct of 2 bound to SARS-CoV-2 M<sup>Pro</sup> (PDB ID 6XHM) (a) and its corresponding 2D interaction diagram (b).

in an acyloxymethylketone inhibitor. Since the nucleophilic attack of a cysteine protease detaches the acyloxy group of an acyloxymethylketone inhibitor, acyloxymethylketone inhibitors are irreversible. As depicted in Figure 6, the acyloxymethylke-



Compd	R	IC <sub>50</sub> (SARS-CoV M <sup>pro</sup> )
9		0.017 μM
10		0.053 μM
11		0.074 μM
12		0.079 μM
13		0.082 μM
14		0.086 μM
15		0.087 μM
16		0.097 μM
17		0.182 μM
18		0.205 μM
19		0.205 μM
20		0.230 μM

**Figure 6.** Acyloxymethylketone covalent inhibitors against SARS-CoV M<sup>pro</sup>.

tone inhibitors reported by Hoffman et al.<sup>26</sup> exhibit strong enzymatic potency against SARS-CoV M<sup>pro</sup>. Especially, **9** possesses the lowest IC<sub>50</sub> of 0.017 μM against SARS-CoV. The crystal structure (PDB ID 6XHN) of **9** in complex with SARS-CoV M<sup>pro</sup> is depicted in Figure 7.

In stark contrast to HMK inhibitors, here **9** is bound to the S atom of M<sup>pro</sup> Cys145 via an irreversible covalent bond (1.88 Å C–S bond length) at its α-methylene. The inactivation of cysteine proteases by these acyloxymethylketones can proceed via two possible mechanisms. One possibility is the direct displacement of the cyanobenzoate group by the cysteine to form the covalent thioether adduct. The second possibility involves the formation of the hemithioacetal, followed by a three-membered sulfonium intermediate that rearranges to form the thioether adduct.<sup>33</sup> The cyanobenzoate moiety serves as the leaving group. As shown in Figure 6, increasing electron density of the leaving group decreases enzymatic activity. Other critical

interactions include the hydrogen bonds of the ketone carbonyl inside the oxyanion hole with the backbone NH groups of Gly143 and Cys145.

**2.1.1.3. P<sub>3</sub>- and P<sub>2</sub>-Modified HMK and Alkoxyethylketone Inhibitors.** The P<sub>3</sub>- and P<sub>2</sub>-modified HMK and alkoxyethylketone inhibitors also from Hoffman et al.<sup>26</sup> are illustrated in Figure 8.

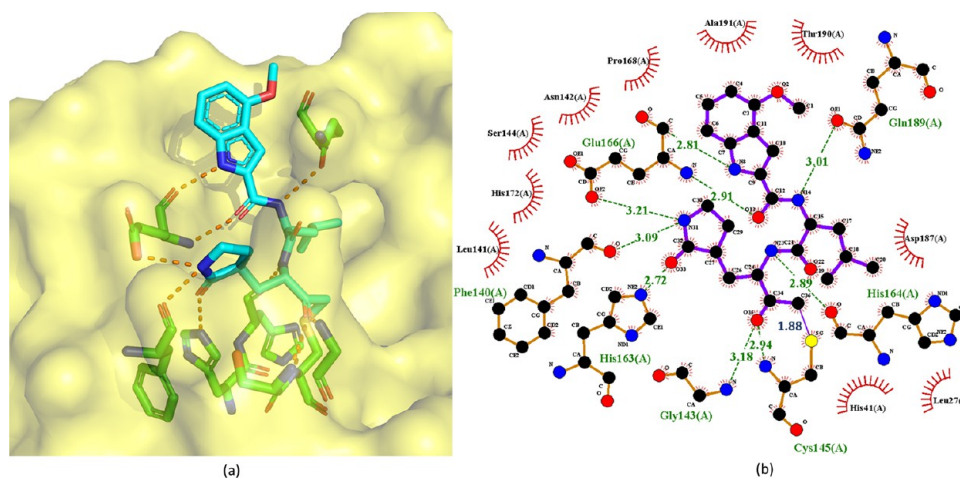
Considering the poor leaving group ability of the alkoxy moiety, it is likely that the attack of Cys145 is on the carbonyl C atom as seen with the HMK inhibitors. The comparison between the compounds in Figures 8 and 4 suggests that, first, a noteworthy reduction in enzymatic and antiviral potency can be found for each hydroxymethylketone derivative and its corresponding ether counterpart, such seen with **22** vs **3**, **26** vs **21**, **24** vs **2**, and **28** vs **23**. Second, removing the methoxy group from the indole while maintaining the two optimal P<sub>2</sub> residues (Leu and β-tert-butyl-Ala) generally leads to slightly weaker potency in both the enzymatic and antiviral assays, such as seen with **21** vs **3**, **26** vs **22**, **28** vs **24**, and **23** vs **2**. Overall, the findings reveal that the 4-methoxy group in the indole does not play a very significant role in the P<sub>3</sub> cap other than improving the solubility characteristics of the inhibitors.

**2.1.1.4. α-Ketoamide Inhibitors.** Zhang et al. designed and synthesized several peptidomimetic α-ketoamides as broad-spectrum inhibitors against β-coronavirus, α-coronavirus, and enterovirus M<sup>pro</sup> enzymes.<sup>34,35</sup> The ones with both high M<sup>pro</sup> enzymatic activity and high antiviral activity against SARS-CoV and SARS-CoV-2 are depicted in Figure 9.

Zhang et al.<sup>35</sup> performed the SAR analysis. Comparing **29**, **30**, and **31**, which differ only in terms of the nature of the P<sub>2</sub> groups, suggests that the binding affinities depend on the size of the P<sub>2</sub> substituent. Unlike the enterovirus M<sup>pro</sup>, the S<sub>2</sub> pocket of SARS-CoV-2 M<sup>pro</sup> displays substantial plasticity and can adapt to the shape of a smaller cyclopropane moiety. The smaller P<sub>2</sub> group leads to lower IC<sub>50</sub> and consequently higher efficacy. To lengthen the half-life time in plasma and prevent cellular proteases from accessing and cleaving the bond, the P<sub>3</sub>–P<sub>2</sub> amide bond is hidden inside a pyridone ring. In addition, to increase the solubility in plasma and to reduce the binding to plasma proteins, the hydrophobic cinnamoyl moiety is replaced by a Boc-substituted amino-pyridone.

The crystal structures of **29** and **32** bound to SARS-CoV and SARS-CoV-2 M<sup>pro</sup> are available with PDB ID 5NSO and 6Y2G, respectively (see Figure 10). These crystal structures reveal that the nucleophilic attack of M<sup>pro</sup> Cys145 onto the α-keto group of an α-ketoamide inhibitor results in a hemithioacetal. The hydroxyl group of this hemithioacetal is stabilized by a hydrogen bond with His41. In addition, the carbonyl O atom of the amide accepts a hydrogen bond from the main-chain amide of Cys145. The amide O atom of **29** also forms a hydrogen bond with the main-chain amide of Gly143. This is a great merit of the α-ketoamides. Their warhead could generate multiple hydrogen-bonding interactions with the catalytic center of the target proteases, which may add an advantage over other warheads such as aldehydes<sup>36</sup> or Michael acceptors.<sup>37</sup>

To determine the ADMET properties of **32**, mice were administered **32** subcutaneously at 20 mg/kg. The mean residence time is 2.7 h, and the plasma half-life is 1.8 h. Especially, its lung tissue level is promising. After 4 h, **32** still has a concentration at approximately 13 ng/g in lung tissue, which is quite beneficial since COVID-19 infects lungs. Mice do not show any adverse effects after inhalation, which suggests that **32** could be administered directly to the lungs.<sup>35</sup>



**Figure 7.** Cocrystal structure of the covalent adduct of **9** bound to SARS-CoV M<sup>pro</sup> (PDB ID 6XHN) (a) and its corresponding 2D interaction diagram (b).

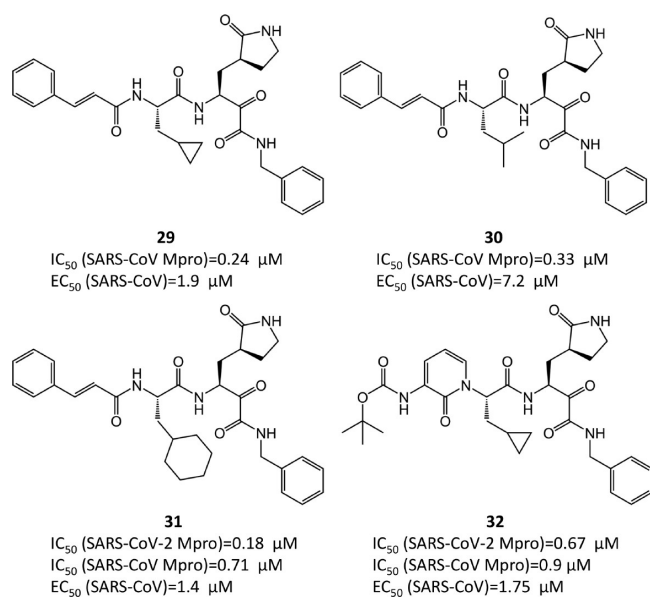
Compd	R <sub>1</sub>	R <sub>2</sub>	R <sub>3</sub>	IC <sub>50</sub> (SARS-CoV M <sup>pro</sup> )	EC <sub>50</sub> (SARS-CoV)
21				0.02 μM	17 μM
22				0.035 μM	32 μM
23				0.038 μM	20 μM
24				0.053 μM	31 μM
25				0.091 μM	33 μM
26				0.105 μM	46 μM
27				0.112 μM	20 μM
28				0.131 μM	45 μM

**Figure 8.** P<sub>3</sub>- and P<sub>2</sub>-modified HMK and alkoxyethylketone covalent inhibitors.

**2.1.1.5. Benzothiazole-Containing Ketone Inhibitors.** Hayashi et al.<sup>38–40</sup> developed tens of benzothiazole-containing ketone inhibitors against SARS-CoV M<sup>pro</sup>. Compounds **33–52** with enzyme inhibitory potency in sub-micromolar range are shown in Figures 11 and 12.

Hayashi et al. explored the SAR of this class of compounds.<sup>38</sup> As a starting point for the compounds in Figure 11, **39** exhibits promising inhibition with a  $K_i$  value of 0.022 μM, which suggests that the benzothiazole unit is a suitable chemical warhead group for occupying the S<sub>1</sub>'-site. Thus, **39** was advanced as a lead

compound for further development of **33–38**. The phenyl group of the P<sub>4</sub>-moiety of **39** was functionalized with various electron-donating and -withdrawing groups. The inhibitors that contain electron-donating substituents such as methoxy, hydroxyl, or *N,N'*-dimethylamino at the *o*-, *p*- or *m*-positions were found to be more active than **39**. Especially, the *m*-methoxy and *p*-*N,N'*-dimethylamino substituted analogs were found to strongly inhibit SARS-CoV M<sup>pro</sup>. Notably, the *m*-*N,N'*-dimethylamino derivative **33** has a  $K_i$  of 0.003 μM and is the most potent inhibitor of this series. These results confirm that an



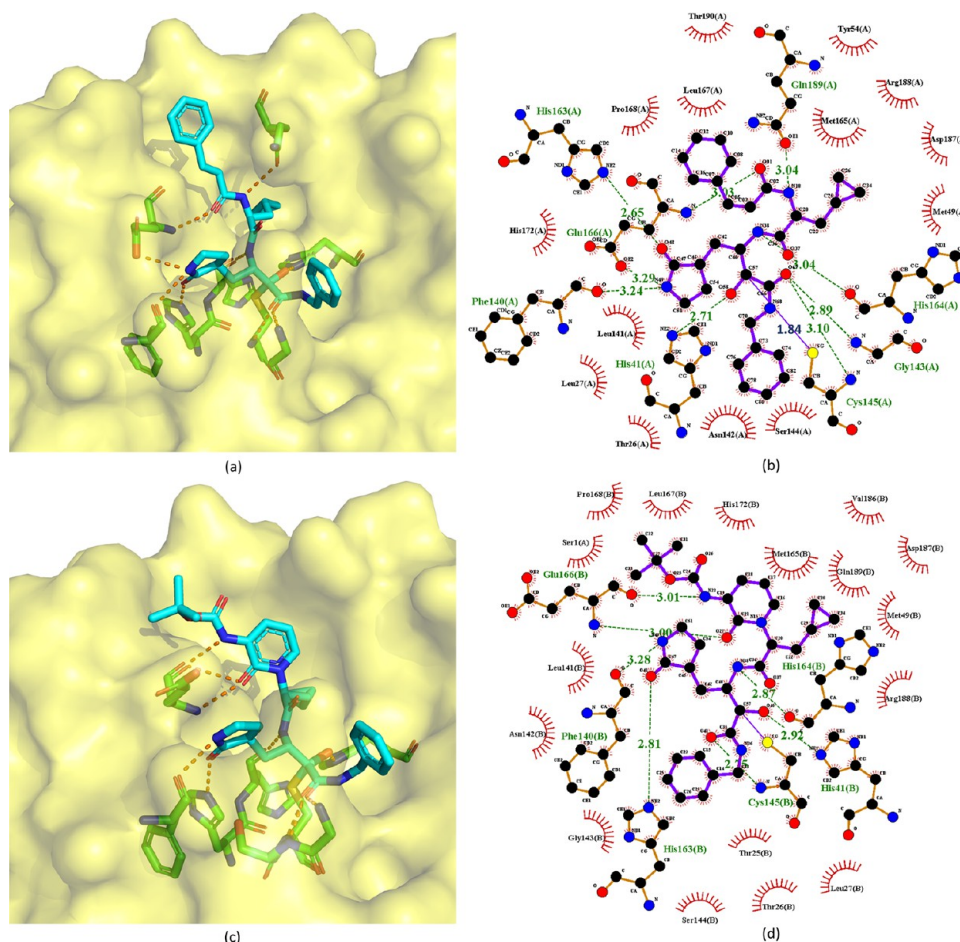
**Figure 9.**  $\alpha$ -Ketoamide covalent inhibitors.

electron-donating substituent on the phenyl ring of the  $P_4$ -moiety typically increases the activity of the compounds. In the case of the 4-*N,N*-dimethylamino phenoxy acetyl group, Hayashi et al.'s docking studies suggested a different folding

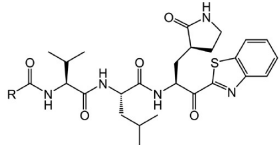
conformation allowing a new hydrophobic interaction with Ala191 at the  $P_4$  position.

In Figure 12, Hayashi et al.<sup>39</sup> selected 44 as a lead compound for further optimization. First, they substituted the 5-position of the indole unit in 44 with 5-methoxy, 5-chloro, and 5-hydroxy, which creates 45, 46, and 51, respectively. Among them, the 5-chloro substituent 46 yielded a better  $K_i$  than the lead 44. Next, a methoxy was introduced into the 6-position of the indole unit of 44, which forms 48. However, this regioisomer (48) displayed significantly lower activity. Third, the  $P_3$  indole unit of 44 was replaced by benzimidazole, benzothiazole, benzofuran, and indoline scaffolds. The benzimidazole 41 exhibits 3 times the potency of 44. However, the replacement of the indole with an indoline (52) or benzothiazole (49) provided less potent analogues. Fourth, Hayashi et al. also attempted placing a carbonyl substitution at the 3-position of the indole of 50, which leads to a 10-times potency decrease compared to the 2-substituted indole. Molecular docking suggested that this substitution may prevent critical hydrogen-bond interactions with  $M^{Pro}$ .<sup>39</sup>

Notably, the methoxy substitution at the 4-position of the indole unit (40) exhibits excellent inhibitory activity with 10- and 55-fold increase compared to the 5-methoxy (45) and 6-methoxy (48) derivatives, respectively. This finding reveals that the methoxy at the 4-position of the indole unit plays a vital role in the inhibitor- $M^{Pro}$  interaction. Konno et al.'s recent report<sup>41</sup> suggested that 40 (YH-53) has drug development potential



**Figure 10.** Cocrystal structures of the covalent adducts of 29 (a, b) and 32 (c, d) bound to SARS-CoV or SARS-CoV-2  $M^{Pro}$  (PDB ID 5N5O and 6Y2G).



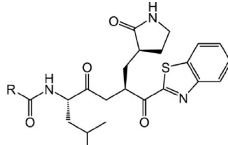
Compd	R	$K_i$		$IC_{50}$
		(SARS-CoV-2 Mpro)	(SARS-CoV Mpro)	
33			0.003 $\mu$ M	
34				0.65 $\mu$ M
35				0.75 $\mu$ M
36			0.014 $\mu$ M	0.92 $\mu$ M
37			0.011 $\mu$ M	1.2 $\mu$ M
38		0.0145 $\mu$ M	0.0041 $\mu$ M	1.7 $\mu$ M
39			0.022 $\mu$ M	2.3 $\mu$ M

**Figure 11.** Benzothiazole ketone-containing inhibitors 33–39.

against SARS-CoV-2, which will be discussed in section 2.1.1.7. The activity of the 4-methoxy group at the indole unit of **40** was further verified by substitutions with 4-isopropoxyl (**43**), 4-isobutyloxy (**47**), and 4-hydroxyl (**42**) moieties. The decrease in activities of these analogues compared to **40** strongly suggests that the methoxy group at the 4-position is superior to the isopropoxy, isobutyloxy, or hydroxyl groups at the 4-position.

Konno et al.<sup>41</sup> also determined the crystal structure of **40** bound to SARS-CoV-2 M<sup>Pro</sup>, which is shown in Figure 13. In this crystal structure, **40** exhibits an extended conformation. The Cys145 of M<sup>Pro</sup> forms a tetrahedral hemithioacetal bond with the carbonyl C atom at the P<sub>1</sub> position of **40**. The pyrrolidin-2-one group of **40** is completely buried in the S<sub>1</sub> pocket of M<sup>Pro</sup>. The carbonyl and amine groups of the pyrrolidine-2-one group accept hydrogen bonds from the side chains of His163 and Glu166, respectively. Additionally, the N and S atoms of the benzothiazole form a hydrogen bond network with water and His41 in the active site, respectively. More interestingly, the binding of **40** shifts a loop region (residues 188–194) of M<sup>Pro</sup> toward the inhibitor by approximately 2.5 Å. Thus, Thr190, Gln189, and Glu166 are close to the 4-methoxy-indole group at the P<sub>3</sub> position of **40**, which is important for the enhanced inhibitory activity. The side chain carbonyl of Gln189 also forms a hydrogen bond with the main chain amide group at the P<sub>2</sub> position.

**2.1.1.6. Thiazole-Containing Ketone Inhibitors.** Konno et al.<sup>38</sup> and Thanigaimalai et al.<sup>40</sup> also replaced the benzothiazole moiety at P<sub>1</sub>' by 5-substituted thiazoles (Figure 14). However, 5-substituted thiazole replacements generally compromise inhibitory potency. The crystal structure of benzothiazole-containing ketone inhibitor **40** with SARS-CoV-2 M<sup>Pro</sup> (PDB ID 7E18, see Figure 13) reveals that the substituent in the 5-position of the thiazole at P<sub>1</sub>' may sterically interact with the S<sub>1</sub> pocket of M<sup>Pro</sup> thereby reducing the binding affinity of the thiazole-containing ketone inhibitors with M<sup>Pro</sup>. This comparison suggests that the benzothiazole unit is a more suitable substituent on the ketone warhead group for the P<sub>1</sub>' moiety.



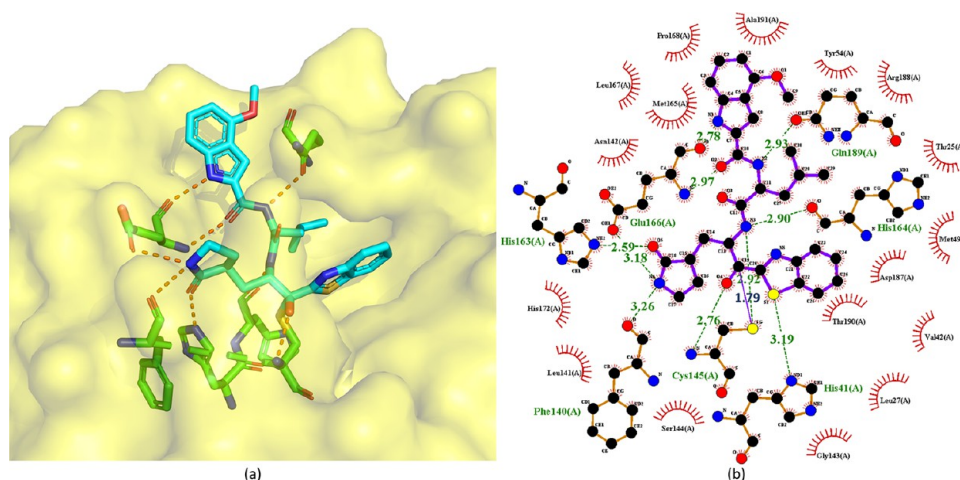
Compd	R	$K_i$		$IC_{50}$	CC <sub>50</sub>
		(SARS-CoV-2 Mpro)	(SARS-CoV Mpro)		
40		0.347 $\mu$ M	0.0063 $\mu$ M	0.74 $\mu$ M	> 100 $\mu$ M
41		0.032 $\mu$ M	0.022 $\mu$ M	1.3 $\mu$ M	
42			0.026 $\mu$ M	1.5 $\mu$ M	
43			0.048 $\mu$ M		
44			0.065 $\mu$ M	1.5 $\mu$ M	
45			0.067 $\mu$ M	4.6 $\mu$ M	
46			0.028 $\mu$ M	4.8 $\mu$ M	
47			0.03 $\mu$ M	5.2 $\mu$ M	
48			0.33 $\mu$ M		
49			0.8 $\mu$ M		
50			0.68 $\mu$ M		
51			0.16 $\mu$ M		
52			0.12 $\mu$ M		

**Figure 12.** Benzothiazole ketone-containing inhibitors 40–52.

**2.1.1.7. Perspectives on SARS-CoV-2 Ketone-Based Inhibitors.** One of the most promising ketone-based inhibitors is PF-00835231 (**2**). Currently its phase I clinical trial has been completed (<https://clinicaltrials.gov/ct2/show/NCT04627532?term=PF-00835231&draw=2&rank=1>). It is potent in blocking SARS-CoV-2 M<sup>Pro</sup>. Importantly, the *in vitro* and *in vivo* studies in rats indicate that both PF-00835231 and prodrug PF-07304814 exhibit no organ toxicity and minimal side effects. In addition, their work found that these compounds do not block the hERG channel.<sup>42</sup>

Another ketone-based inhibitor with drug development potential is **40** (YH-53), which has a different warhead from **2**. Positives include its stability in plasma and no obvious toxicity, mutagenicity, or other side effects with regards to hERG and CYP activity. However, even though *in vitro* assays suggested promising ADMET properties, some irregular absorption was detected by *in vivo* pharmacokinetic studies.<sup>41</sup> Nonetheless, **40** could provide a valuable lead compound for further optimization.



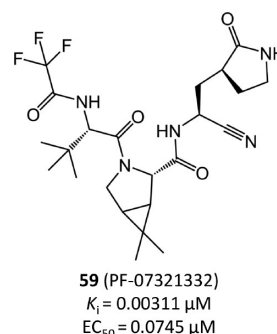


**Figure 13.** Cocystal structures of the covalent adducts of **40** bound to SARS-CoV-2 M<sup>Pro</sup> (PDB ID 7E18) (a) and its corresponding 2D interaction diagram (b).

Compd	R <sub>1</sub>	R <sub>2</sub>	K <sub>i</sub> (SARS-CoV Mpro)
53			0.06 μM
54			0.17 μM
55			0.27 μM
56			0.33 μM
57			0.47 μM
58			0.66 μM

**Figure 14.** Thiazole ketone-containing inhibitors from Konno et al.<sup>38</sup> and Thanigaimalai et al.<sup>40</sup>

**2.1.2. The Nitrile-Containing Drug Candidate from Pfizer.** One of the most advanced drug candidates targeting SARS-CoV-2 M<sup>Pro</sup> currently is nitrile-containing inhibitor PF-07321332 (**59** in Figure 15), which was developed by Pfizer during this pandemic and disclosed at the American Chemical Society Spring 2021 meeting. PF-07321332 is now in phase 3 clinical trials (<https://clinicaltrials.gov/ct2/show/NCT04960202?term=PF-07321332&draw=2&rank=3>). It is the first orally administered SARS-CoV-2 inhibitor. According to a recent report from Pfizer,<sup>43</sup> its enzymatic activity and cellular antiviral activity against SARS-CoV-2 are both high with  $K_i = 0.00311 \mu\text{M}$  and  $\text{EC}_{50} = 0.0745 \mu\text{M}$ . Especially, its  $\text{EC}_{50}$  is the lowest among all the current M<sup>Pro</sup> inhibitors, suggesting an optimal cell permeability. In mouse models, PF-07321332 can



**Figure 15.** Nitrile-containing drug candidate from Pfizer (PF-07321332).

protect lung tissue well from being damaged by virus replication.<sup>43</sup>

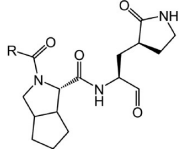
More importantly, PF-07321332 demonstrates low toxicity and side effects and does not block the hERG channel. Its ADMET properties are promising as well. For example, its plasma clearance is moderate with elimination half-lives of 5.1 and 0.79 h in rats and monkeys, respectively.

According to Pfizer's recent report,<sup>43</sup> the nitrile of PF-07321332 forms a covalent bond with SARS-CoV-2 M<sup>Pro</sup> in the crystal structure. However, this crystal structure has not been released to the public yet.

**2.1.2.1. Perspectives on PF-07321332.** PF-07321332 is on its way to becoming the first M<sup>Pro</sup> drug to treat SARS-CoV-2. It may reach the market by the end of 2021.<sup>44</sup> One of its major advantages is that it could be taken orally as a pill or capsule and, thus, be administered outside of hospitals.<sup>5</sup>

**2.1.3. Aldehyde-Based Inhibitors. 2.1.3.1. Bicycloproline-Containing Aldehyde Inhibitors.** Derived from approved protease inhibitor telaprevir or boceprevir, 32 bicycloproline-containing SARS-CoV-2 M<sup>Pro</sup> inhibitors were prepared by Qiao et al.<sup>45</sup> They incorporated an aldehyde in the P<sub>1</sub> position as the warhead to form a covalent bond with Cys145 of SARS-CoV-2 M<sup>Pro</sup>. Additionally, they adopted a bicycloproline moiety from either boceprevir or telaprevir for P<sub>2</sub> and used various hydrophobic aryl subgroups for P<sub>3</sub> to improve the potency and pharmacokinetic properties. As a result, all their compounds show potent SARS-CoV-2 M<sup>Pro</sup> inhibition in the FRET assay with IC<sub>50</sub> values below 1 μM.

Compounds **60**–**91** in Figures 16 and 17 are the bicycloproline-containing inhibitors derived from telaprevir and boceprevir, respectively. Among them, **60**, which is derived from



Compd	R	IC <sub>50</sub> (SARS-CoV-2 Mpro)	EC <sub>50</sub> (SARS-CoV-2)	Compd	R	IC <sub>50</sub> (SARS-CoV-2 Mpro)
<b>60</b>		0.0076 μM	5.63 μM	<b>69</b>		0.0691 μM
<b>61</b>		0.0076 μM	2.97 μM	<b>70</b>		0.0935 μM
<b>62</b>		0.0092 μM	0.67 μM	<b>71</b>		0.1531 μM
<b>63</b>		0.0172 μM	0.54 μM	<b>72</b>		0.1956 μM
<b>64</b>		0.0174 μM	30.49 μM	<b>73</b>		0.2988 μM
<b>65</b>		0.0197 μM	1.5 μM	<b>74</b>		0.375 μM
<b>66</b>		0.03 μM	0.83 μM	<b>75</b>		0.3782 μM
<b>67</b>		0.0347 μM	1.65 μM	<b>76</b>		0.5259 μM
<b>68</b>		0.0362 μM	24.72 μM	<b>77</b>		0.7485 μM

**Figure 16.** Bicycloproline-containing SARS-CoV-2 M<sup>Pro</sup> inhibitors derived from telaprevir.

telaprevir, has the highest M<sup>Pro</sup> binding affinity with IC<sub>50</sub> = 0.0076 μM. To illustrate the detailed binding mode of these compounds with SARS-CoV-2 M<sup>Pro</sup>, Qiao et al.<sup>45</sup> determined the structure of **60** in complex with SARS-CoV-2 M<sup>Pro</sup> (PDB ID 7D3I) as shown in Figure 18.

In this crystal structure, the carbonyl C atom of the aldehyde warhead of **60** reacts with the S atom of Cys145 to form a 1.77 Å covalent bond. Moreover, the O atom of the hemithioketal interacts with the main-chain amide of Cys145 by a hydrogen bond of 2.89 Å. The P<sub>1</sub> γ-lactam ring of **60** resides deep in the S<sub>1</sub> pocket. The O and N atoms of the lactam form hydrogen bonds with the side chain of His163 (2.77 Å) and the main chain of Phe140 (3.26 Å), respectively. The main-chain amide of P<sub>1</sub> also accepts a 2.88 Å hydrogen bond from the backbone O atom of His164. Due to the conformational constraints inherent from the structure of proline,<sup>46</sup> the rigid P<sub>2</sub> bicycloproline of **60** is restrained in a trans-exo conformation with limited NC<sub>α</sub> bond rotation. As a result, the bicycloproline group stays close to the hydrophobic S<sub>2</sub> pocket and forms hydrophobic interactions with His41, Met49, Met165, Asp187, Arg188, and Gln189 of M<sup>Pro</sup>. The backbone carbonyl O atom of P<sub>3</sub> of **60** forms a 2.91 Å hydrogen bond with the backbone amide of Glu166. The 1-ethyl-3,5-difluorobenzene moiety of P<sub>3</sub> occupies the S<sub>4</sub> site with an extended conformation and forms hydrophobic interactions with Leu167, Pro168, and Gln189.<sup>45</sup> Additionally, one F atom on the tail of **60** could form dipole–dipole interactions with the C<sub>α</sub> atom of Pro168.

The SAR between different bicycloproline-containing inhibitors suggests the two different bicycloproline moieties at P<sub>2</sub> do not largely impact their binding affinities to SARS-CoV-2 M<sup>Pro</sup>, such as **84** (IC<sub>50</sub> = 0.0165 μM) vs **61** (IC<sub>50</sub> = 0.0076 μM), **86** (IC<sub>50</sub> = 0.019 μM) vs **62** (IC<sub>50</sub> = 0.0092 μM), and **79** (IC<sub>50</sub> = 0.013 μM) vs **63** (IC<sub>50</sub> = 0.0172 μM). Moreover, the compounds with F or Cl atoms on the tail can be more active than others because these halogen atoms could form dipole–dipole interactions with M<sup>Pro</sup> such as with the C<sub>α</sub> atom of Pro168.

In addition to the enzymatic activity, the cellular antiviral activity of **60**–**68** and **78**–**88** was also tested in cell protection assays,<sup>45</sup> which are shown in Figures 16 and 17 in terms of the EC<sub>50</sub>. Among them, six compounds, namely, **86** (EC<sub>50</sub> = 0.53 μM), **63** (EC<sub>50</sub> = 0.54 μM), **79** (EC<sub>50</sub> = 0.66 μM), **62** (EC<sub>50</sub> = 0.67 μM), **66** (EC<sub>50</sub> = 0.83 μM), and **83** (EC<sub>50</sub> = 0.86 μM), exhibit sub-micromolar or low micromolar EC<sub>50</sub> values. Notably, probably due to the poor cell membrane permeability caused by the relatively low lipophilic nature of the groups in the P<sub>3</sub> position,<sup>47</sup> some compounds such as **64** and **68** lack activity in the cell protection assays despite potent enzymatic inhibition.

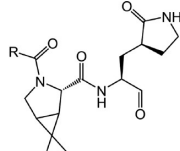
Compounds **63** and **83** exhibit promising pharmacokinetics properties with oral bioavailability of 11.2% and 14.6% in the experiments in Sprague–Dawley rats. In light of that, Qiao et al.<sup>45</sup> further evaluated their toxicity and antiviral activity *in vivo*.

Determination of tolerance in rats was evaluated at 100 and 200 mg/kg twice daily for 7 consecutive days. No noticeable toxicity was found for **63** and **83**. Moreover, the *in vivo* antiviral activity of the compounds was assayed in a human angiotensin-converting enzyme 2 transgenic mouse model. Compounds **63** (50 mg/kg once daily) and **83** (50 mg/kg twice daily or 50 mg/kg once daily) were administered starting at 1 h prior to virus inoculation and lasting until 5 days postinfection (5 dpi). During this period, no abnormal behavior or body-weight loss was observed in the mice. More importantly, at 5 dpi, the viral RNA loads in the lung tissues of treatment groups were almost undetectable. This result suggests that **63** and **83** could efficiently inhibit SARS-CoV-2 replication and ameliorate SARS-CoV-2 induced lung lesions *in vivo*.

**2.1.3.2. Other Aldehyde-Based Inhibitors.** In some designs,<sup>48–53</sup> an aldehyde is selected as the warhead in the P<sub>1</sub> moiety to form a covalent bond with Cys145 of SARS-CoV-2 and SARS-CoV M<sup>Pro</sup> (see Figure 19). In addition, most of these inhibitors are functionalized with an (S)-γ-lactam ring that occupies the S<sub>1</sub> site of M<sup>Pro</sup>, which was already suggested by Zhang et al.<sup>34</sup> As expected, many of them show potent IC<sub>50</sub> or K<sub>i</sub> values against M<sup>Pro</sup>, especially **92** and **93** with IC<sub>50</sub> values of 0.04 μM and 0.053 μM, respectively.

Some of these aldehyde-based inhibitors have available crystal structures with SARS-CoV-2 or SARS-CoV M<sup>Pro</sup> in PDB, such as **92** (PDB ID 6MOK), **93** (PDB ID 6LZE),<sup>48</sup> **96** (GC373, PDB ID 6WTK),<sup>50</sup> **104** (PDB ID 6LOO),<sup>52</sup> and **105** (PDB ID 2GX4).<sup>53</sup>

As an example, the crystal structure of **92** bound to SARS-CoV-2 M<sup>Pro</sup> is chosen to depict the binding mode (Figure 20a,b). In this crystal structure, the C atom of the aldehyde group of **92** forms a standard 1.81 Å C–S covalent bond with Cys145 of SARS-CoV-2 M<sup>Pro</sup>, and the conformation is stabilized by the 2.83 Å hydrogen bond between the O atom of the hemithioketal group and the backbone of Cys145 in the S<sub>1</sub>' site. The (S)-β-lactam ring of **92** at P<sub>1</sub> fits well into the S<sub>1</sub> site. The O atom of the (S)-β-lactam ring accepts a 2.71 Å hydrogen bond from the side chain of His163. The main chain of Phe140 and



Compd	R	IC <sub>50</sub> (SARS-CoV-2 Mpro)	EC <sub>50</sub> (SARS-CoV-2)	Compd	R	IC <sub>50</sub> (SARS-CoV-2 Mpro)	EC <sub>50</sub> (SARS-CoV-2)
78		0.0124 μM	2.08 μM	85		0.0185 μM	1.64 μM
79		0.013 μM	0.66 μM	86		0.019 μM	0.53 μM
80		0.0132 μM	5.57 μM	87		0.0372 μM	4.68 μM
81		0.0133 μM	1.18 μM	88		0.0433 μM	16.95 μM
82		0.0145 μM	1.73 μM	89		0.0508 μM	
83		0.0152 μM	0.86 μM	90		0.0521 μM	
84		0.0165 μM	2.23 μM	91		0.453 μM	

Figure 17. Bicycloproline-containing SARS-CoV-2 M<sup>pro</sup> inhibitors derived from boceprevir.

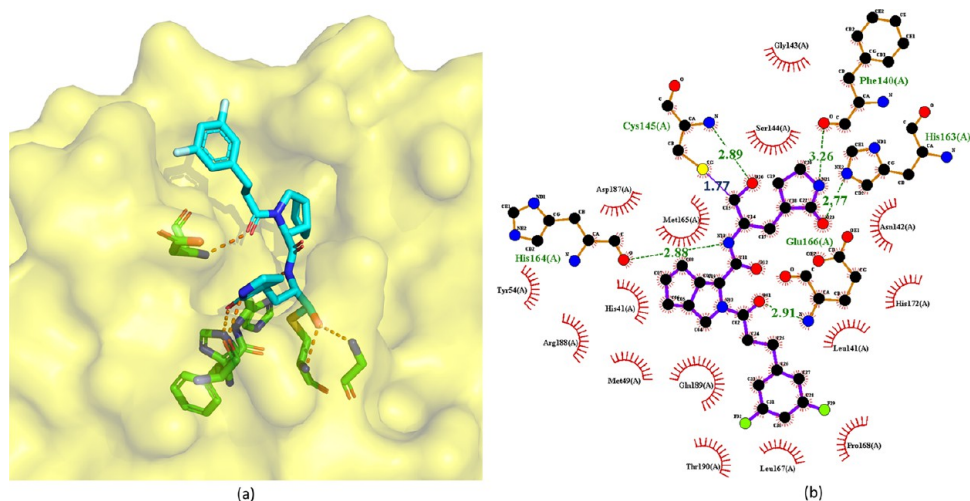
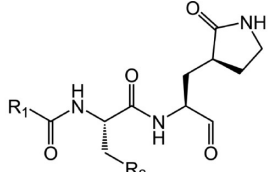


Figure 18. Crystal structure of **60** covalently bound to SARS-CoV-2 M<sup>pro</sup> (PDB ID 7D3I) (a) and its corresponding 2D interaction diagram (b).

the side chain of Glu166 also stabilize the (*S*)- $\beta$ -lactam ring via a 3.26 Å hydrogen bond and a 2.96 Å hydrogen bond with its NH group, respectively. Additionally, the amide bonds in the main chain of **92** form two hydrogen bonds with the main chains of His164 (3.29 Å) and Glu166 (2.81 Å). The 3-fluorophenyl moiety at P<sub>2</sub> of **92** inserts deeply into the S<sub>2</sub> site of M<sup>pro</sup>, stacking with the imidazole ring of His41. The side chains of Met49, Met165, Val186, Asp187, and Arg188 are near the 3-fluorophenyl group, leading to extensive hydrophobic interactions. Just like **4** and **9**, the indole group at the P<sub>3</sub> position of **92**, which is exposed to solvent, is stabilized by a 2.57 Å hydrogen bond with Glu66. Moreover, the side chains of Pro168

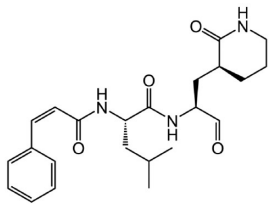
and Gln189 have hydrophobic interactions with the indole group of **92**. Compound **95** shares with **92** a similar inhibitor binding mode (Figure 20c,d). The binding mode of GC373 (**96**) is as the same as that of GC376 (**110**) and will be illustrated in section 2.1.3.3.

Comparing the enzymatic activities of these aldehyde-based inhibitors reveals that **92** and **93** are the most potent. This is because the NH group of their indole can form a hydrogen bond with the backbone carbonyl of Glu166, just like **4** and **9**. This confirms that indole is an optimal design for the P<sub>3</sub> position of M<sup>pro</sup> inhibitors. Another finding from the comparison is the reason why **94** and **95** are the second most potent compounds.

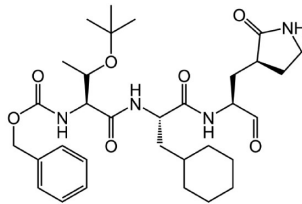


Compd	R <sub>1</sub>	R <sub>2</sub>	IC <sub>50</sub> (SARS-CoV-2 Mpro)	IC <sub>50</sub> (SARS-CoV Mpro)	EC <sub>50</sub> (SARS-CoV-2)	CC <sub>50</sub>
92			0.04 μM		0.72 μM	>100 μM
93			0.053 μM		0.53 μM	>100 μM
94			0.17 μM	0.9 μM	0.15 μM	63.3 μM
95			0.28 μM	1.7 μM	0.25 μM	>100 μM
96 (GC373)			0.4 μM	0.07 μM	1.5 μM	>100 μM
97			0.43 μM	2.3 μM	0.9 μM	>100 μM
98			0.48 μM	1.2 μM	0.8 μM	>100 μM
99			0.82 μM	3.9 μM		>100 μM
100				0.2 μM		
101				0.5 μM		
102				0.7 μM		
103				0.83 μM		



**104**  
IC<sub>50</sub> (SARS-CoV) = 0.508 μM



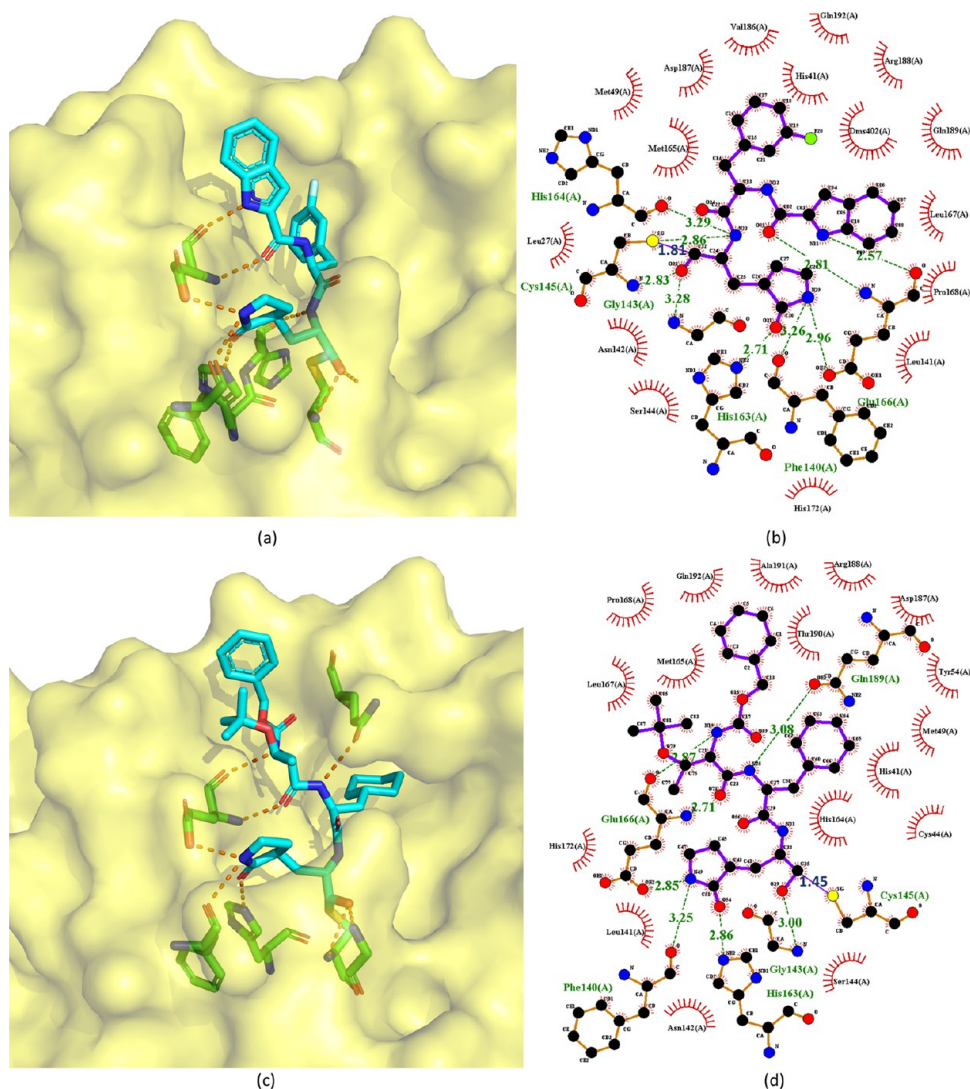
**105**  
K<sub>i</sub> (SARS-CoV Mpro) = 0.053 μM  
EC<sub>50</sub> (SARS-CoV) = 0.6 μM  
CC<sub>50</sub> > 200 μM

**Figure 19.** Other aldehyde-based inhibitors.

The hydrophobic tails in their P<sub>3</sub> sites could form hydrophobic interactions with the hydrophobic amino acids in the M<sup>PRO</sup> S<sub>3</sub> pocket, such as Met165 and Leu167.

In addition to enzymatic activity, the cellular antiviral activity of 92–98 and 105 against SARS-CoV-2 or SARS-CoV was also assayed in terms of the EC<sub>50</sub>. All of them have strong antiviral

activity with EC<sub>50</sub> values ≤1.5 μM (see Figure 19). To further examine the antiviral activity within a large dynamic range, quantitative reverse transcription polymerase chain reaction (RT-PCR) was performed on cultures treated with 92, 93, GC373 (96), and its prodrug GC376 (110), which revealed good antiviral effect against SARS-CoV-2.<sup>48,50</sup> Particularly,



**Figure 20.** Cocystal structures of the covalent adducts of **92** (a, b) and **105** (c, d) bound to SARS-CoV or SARS-CoV-2 M<sup>pro</sup> (PDB ID 6M0K and 6L0O).

GC373 and GC376 were reported to decrease viral titers by 3-log values.<sup>50</sup>

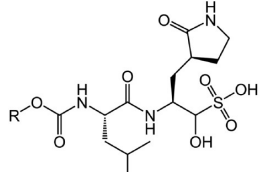
The toxicity of **92–99** and prodrug GC376 (**110**) was assayed in Huh-7, CRFK, or L929 cells. Except for **94**, which has a CC<sub>50</sub> = 63.3 μM,<sup>49</sup> none of these compounds cause obvious cytotoxicity. The CC<sub>50</sub> values of **92**, **93**, and **95–99** are higher than 100 μM,<sup>48,49</sup> and the CC<sub>50</sub> values of **105**, GC373, and GC376 are over 200 μM.<sup>50,53</sup> More importantly, no obvious *in vivo* toxicity of **92** and **93** was observed during the animal tests on Sprague–Dawley rats and beagle dogs.<sup>48</sup>

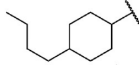
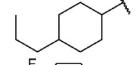

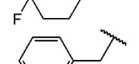
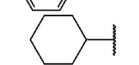
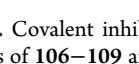
Since no obvious *in vivo* toxicity was observed, the pharmacokinetics properties of **92** and **93** were further assessed by Dai et al.<sup>48</sup> Compound **92** exhibits long *T*<sub>1/2</sub> values (Sprague–Dawley rat, 7.6 h; beagle dog, 5.5 h), low clearance rates (rat, 4.01 (mL/min)/kg; dog, 5.8 (mL/min)/kg), and high AUC values (rat, 41 500 h·ng/mL; dog, 14 900 h·ng/mL). Its potent enzymatic and antiviral activities as well as satisfying pharmacokinetic properties indicate that **92** warrants further optimization toward potential drug candidates.

**2.1.3.3. Water-Soluble Aldehyde Bisulfite Adducts.** The aldehyde bisulfite adducts are prodrugs of the aldehyde-based inhibitors introduced in the last sections created to improve

water solubility.<sup>50</sup> Aldehyde bisulfites can have improved pharmacokinetic properties compared to their aldehyde counterparts, but they are typically rapidly hydrolyzed and converted to the corresponding aldehydes.<sup>54</sup>

Rathnayake et al.,<sup>49</sup> Vuong et al.,<sup>50</sup> and Ma et al.<sup>55</sup> reported a series of aldehyde bisulfite adducts (see Figure 21). Notably, the crystal structure of GC376 (**110**) with SARS-CoV-2 M<sup>pro</sup> is available with PDB ID 6WTJ (see Figure 22). GC376 is the prodrug of GC373 (**96** in Figure 19). GC376 eliminates its bisulfite group and turns into GC373 before binding to M<sup>pro</sup>, then the aldehyde warhead of GC373 forms a covalent bond with Cys145 of M<sup>pro</sup>.<sup>50,55</sup> For other interactions, GC373 mimics the peptide substrate cleaved by the protease.<sup>35</sup> The glutamine surrogate  $\gamma$ -lactam ring of GC373 derived from the P<sub>1</sub> glutamine side chain always occupies the S<sub>1</sub> site. This ring forms hydrogen bonds with the His163 and Glu166 side chains and the Phe140 main chain. An amide bond attaches the  $\gamma$ -lactam side chain to the isobutyl moiety of the hydrophobic S<sub>2</sub> site formed by His41, Met49, and Met169. A carbonate bond in GC373, which accepts hydrogen bonds from the main chain of Glu166 and the side chain of Gln189, attaches the P<sub>2</sub> isobutyl group to a phenylmethyl ester that interacts with the aliphatic S<sub>4</sub> site.<sup>55</sup>



Compd	R	IC <sub>50</sub> (SARS-CoV-2 Mpro)	IC <sub>50</sub> (SARS-CoV Mpro)	EC <sub>50</sub> (SARS-CoV-2)	CC <sub>50</sub>
106		0.2 μM	1.0 μM		59.1 μM
107		0.23 μM	1.7 μM		>100 μM
108		0.41 μM	2.2 μM		>100 μM
109		0.45 μM	1.1 μM		>100 μM
110 (GC376)		0.62 μM 0.19 μM 0.03 μM	2.2 μM 0.05 μM	0.92 μM	>200 μM
111		0.65 μM	3.8 μM		>100 μM

**Figure 21.** Covalent inhibitors with aldehyde bisulfite warhead. The IC<sub>50</sub> values of **106**–**109** and **111** were reported by Rathnayake et al.<sup>49</sup> For **110** (GC376), the IC<sub>50</sub> values of 0.62 μM and 2.2 μM for SARS-CoV-2 and SARS-CoV M<sup>Pro</sup> were given by Rathnayake et al.<sup>49</sup> The IC<sub>50</sub> values 0.19 μM and 0.05 μM to SARS-CoV-2 and SARS-CoV M<sup>Pro</sup> were reported by Vuong et al.<sup>50</sup> The IC<sub>50</sub> value 0.03 μM against SARS-CoV-2 M<sup>Pro</sup> was given by Ma et al.<sup>55</sup>

GC376 (**110**) is an investigational veterinary drug to cure feline infectious peritonitis (FIP).<sup>56–58</sup> Its target is the viral M<sup>Pro</sup>. Researchers also found that GC376 is a broad-spectrum coronavirus protease inhibitor, which is active toward the M<sup>Pro</sup> enzymes of multiple coronaviruses, including FIPV, MERS-CoV, and norovirus.<sup>56,57</sup> In light of its broad-spectrum activity, preclinical studies have been started to examine its potential in treating COVID-19.<sup>59</sup> Different groups have reported inconsistent but promising potency.

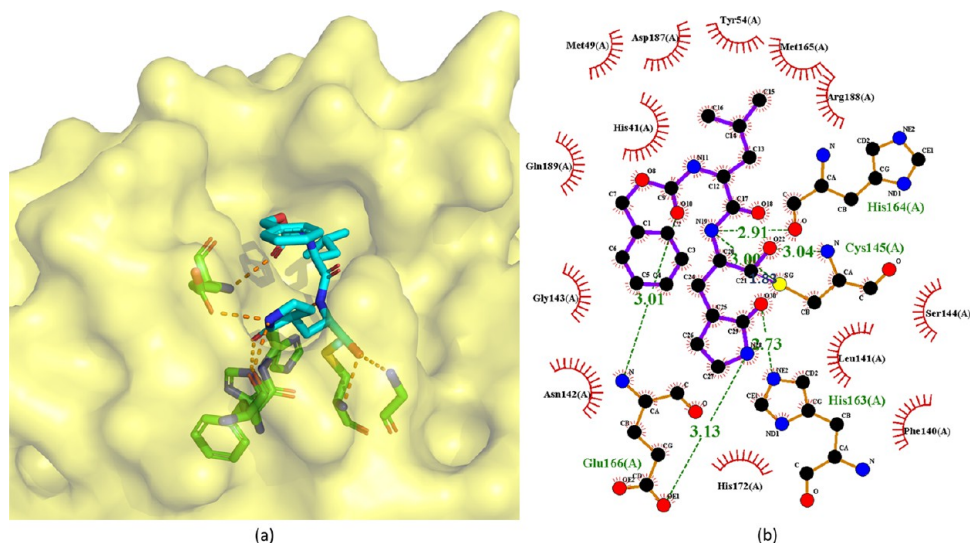
In the FRET enzyme assays conducted by Rathnayake et al.,<sup>49</sup> the IC<sub>50</sub> values of GC376 are 0.62 μM and 2.2 μM against SARS-

CoV-2 M<sup>Pro</sup> and SARS-CoV M<sup>Pro</sup>, respectively. By the same technique, Vuong et al.<sup>50</sup> achieved IC<sub>50</sub> values of 0.19 μM and 0.05 μM against SARS-CoV-2 M<sup>Pro</sup> and SARS-CoV M<sup>Pro</sup>, respectively. While Ma et al.<sup>55</sup> reported an IC<sub>50</sub> value of 0.03 μM against SARS-CoV-2 M<sup>Pro</sup>. It was also reported that GC376 and its variants could increase survival of mice infected with SARS-CoV-2.<sup>60</sup>

For aldehyde bisulfite adducts such as GC376, it is their corresponding aldehydes that interact with M<sup>Pro</sup> and their binding affinities are almost identical to those of their corresponding aldehydes. For example, as shown in Figure 21, the SARS-CoV-2 M<sup>Pro</sup> IC<sub>50</sub> values of **106**, **107**, **108**, **109**, and **111** are 0.2 μM, 0.23 μM, 0.41 μM, 0.45 μM, and 0.65 μM, respectively, while the IC<sub>50</sub> values of their corresponding aldehydes **94**, **95**, **97**, **98**, and **99** are 0.17 μM, 0.28 μM, 0.43 μM, 0.48 μM, and 0.82 μM, respectively. Just like their corresponding aldehydes, the high enzymatic activity of **106** and **107** is also probably due to the hydrophobic tails in their P<sub>3</sub> positions forming hydrophobic interactions with the hydrophobic amino acids in the M<sup>Pro</sup> S<sub>3</sub> pocket.

Similar to their corresponding aldehydes, the cytotoxicity of these bisulfite adducts is also weak,<sup>49,50</sup> except for **106**, which exhibits a CC<sub>50</sub> of 59.1 μM. All the other bisulfite adducts have CC<sub>50</sub> values over 100 μM and GC376 (**110**) even has a CC<sub>50</sub> larger than 200 μM.

**2.1.3.4. Drawbacks of the Aldehyde and Aldehyde Bisulfite Inhibitors.** Aldehyde bisulfite GC373 has shown promising antiviral activity *in vivo*. The bisulfite prodrugs may have improved chemical stability and pharmacokinetic properties, which make them often superior drug candidates over the free aldehydes. However, considering the highly reactive nature of the electrophilic warhead, both the aldehydes and the aldehyde bisulfite prodrugs may suffer from substrate promiscuity. Reactive aldehyde species are often considered toxic, due to their formation of various Schiff bases and DNA adducts, and are known to also induce oxidative stress and inflammation.<sup>61,62</sup> For example, GC373 and its prodrug GC376 are active against proteins cathepsin B and L with IC<sub>50</sub> values in the micromolar range.<sup>63</sup> Therefore, whether these types of warheads offer an



**Figure 22.** Cocystal structures of the covalent adduct of **110** (GC376) bound to SARS-CoV-2 M<sup>Pro</sup> (PDB ID 6WTJ) (a) and its corresponding 2D interaction diagram (b).

advantage over ketone-based covalent inhibitors, including HMK inhibitors, still needs to be investigated carefully.

**2.1.4. Michael Acceptor-Based Inhibitors.** Several Michael acceptor-based inhibitors active against SARS-CoV-2 M<sup>Pro</sup> or SARS-CoV M<sup>Pro</sup> were reported<sup>53,64–67</sup> and are depicted in Figure 23.

As a Michael acceptor, each of **112–116** contains an  $\alpha,\beta$ -unsaturated ester with the double bond at the P<sub>1</sub>' position to form a covalent bond with Cys145 of M<sup>Pro</sup><sup>28</sup> (see Figure 24b,d).

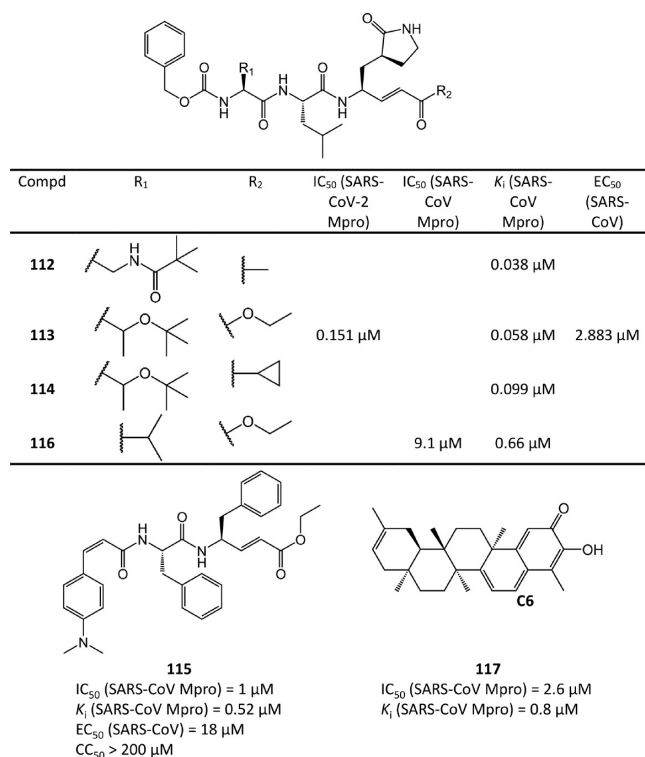


Figure 23. Michael acceptor-based inhibitors.

However, not all Michael acceptor-based inhibitors are peptides. Ryu et al.<sup>67</sup> extracted four quinone-methide triterpenoid derivatives from *Tripterygium regelii* (a woody vine). Among them, **117** has sub-micromolar potency. According to Sreeramulu et al.'s study,<sup>68</sup> the nucleophilic group of M<sup>Pro</sup> reacts with the quinone-methide of **117** or other derivatives through a Michael addition, resulting in the formation of an adduct at C6 (see **117** in Figure 23).

The crystal structures of **113** bound to SARS-CoV-2 M<sup>Pro</sup> and **112**, **113**, and **114** bound to SARS-CoV M<sup>Pro</sup> are available with PDB ID 7JT7, 2ZU4, and 2ZU5, respectively,<sup>64,65</sup> which are depicted in Figure 24. Their binding modes are almost identical. M<sup>Pro</sup> Cys145 attacks the C<sub>β</sub> atom of the  $\alpha,\beta$ -unsaturated ketone at the P<sub>1</sub>' position to form a covalent C–S bond (1.87 Å, 1.78 Å, and 1.94 Å, respectively), and hydrogen bonds are formed between the ketone O atom and the NH groups of Gly143 and Cys145 in the S<sub>1</sub>' pocket. In the S<sub>1</sub> site, the carbonyl O atom and the five-membered lactam ring's N atom at the P<sub>1</sub> position accept hydrogen bonds from His163 and Glu166. The P<sub>2</sub> side chain of each compound is inside a hydrophobic S<sub>2</sub> pocket, while the P<sub>3</sub> group is toward the bulk solvent. The benzoxy group at the P<sub>4</sub> position is in the S<sub>4</sub> pocket with its phenyl ring parallel to a flat surface near Ala191. The peptide NH groups of residues P<sub>1</sub>, P<sub>2</sub>, and P<sub>3</sub> also have four hydrogen bonds with the backbone

carbonyl groups of His164 and Glu166 and the side chain of Gln189. Moreover, the carbonyl group of P<sub>3</sub> interacts with the NH group of Glu166.

The SAR analysis of these analogues (**113–116**) indicates that the introduction of a lipophilic *tert*-butyl group at the P<sub>2</sub> site increases binding affinity by over 10-fold. The possible explanation could be found in the crystal structure of **113** binding to M<sup>Pro</sup> (see Figure 24d). The *tert*-butyl group of the compound turns to the P<sub>4</sub> site and forms hydrophobic interactions with the phenyl ring in the benzoxy group of the compound itself. Moreover, the phenyl ring of the compound interacts with M<sup>Pro</sup> and faces the P<sub>3</sub> site directing the methylene group in a small corner pocket near Ala191.

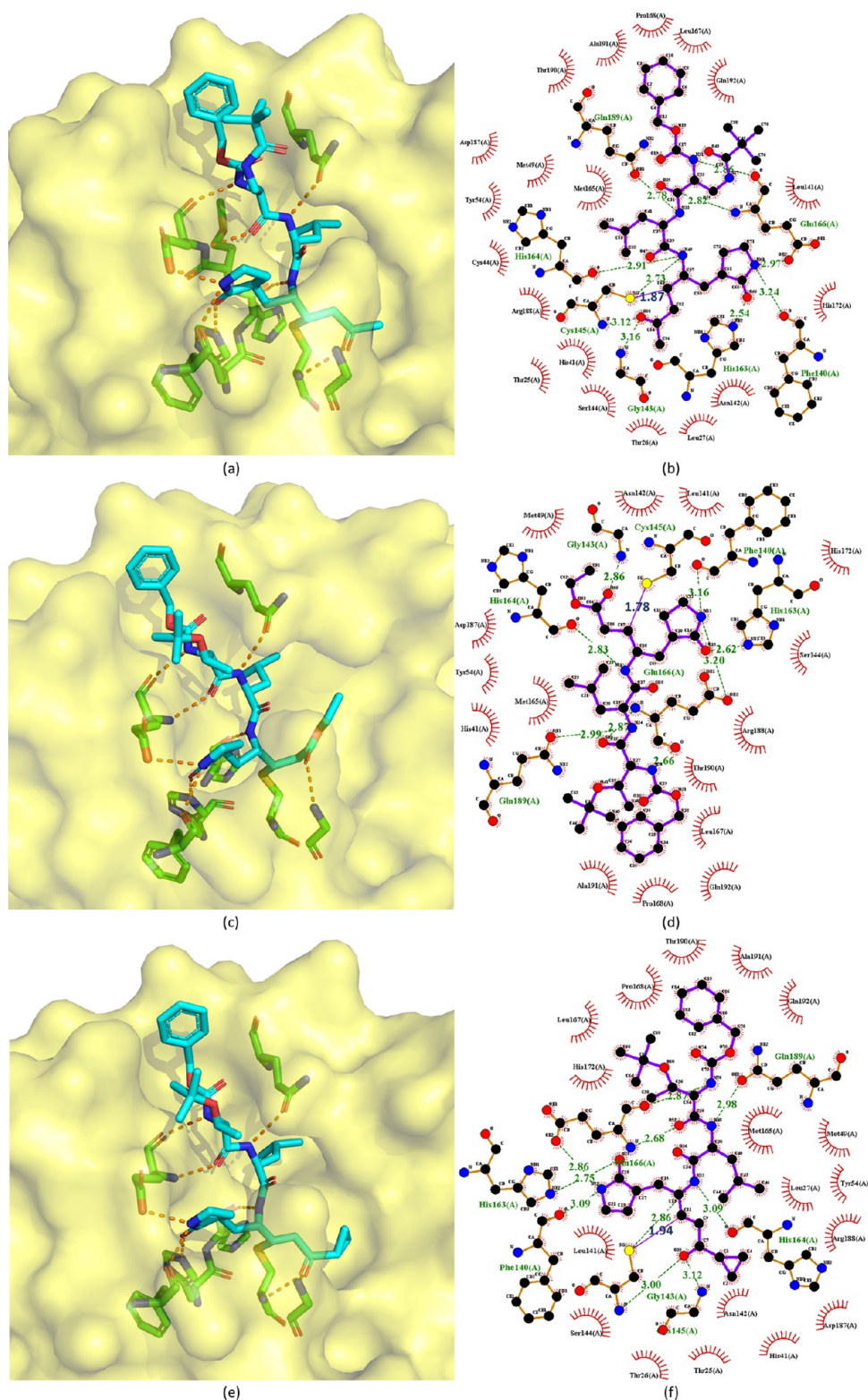
The antiviral activity and cytotoxicity of **113** and **115** were assayed. The EC<sub>50</sub> of **113** against SARS-CoV-2 is 2.883 μM, and the EC<sub>50</sub> of **115** against SARS-CoV is 0.18 μM. Compound **115** also has a CC<sub>50</sub> value over 200 μM, making **115** a promising M<sup>Pro</sup> inhibitor for further studies.

**2.1.4.1. Perspectives on Michael Acceptor-Based M<sup>Pro</sup> Inhibitors.** Although with a risk of presumed indiscriminate reactivity, the covalent modification of targets using an irreversible hetero-Michael addition with a cysteine residue has gained some recent validation with the FDA approval of multiple Michael-acceptor-based drugs.<sup>69</sup> Developing Michael acceptors could be a possible promising direction for discovering SARS-CoV-2 drug candidates. However, careful evaluations of safety and side effects are required.

**2.1.5. Calpain Inhibitors.** Ma et al.<sup>55</sup> found that calpain inhibitor XII (**118**) and calpain inhibitor II (**119**) are also potent against SARS-CoV-2 M<sup>Pro</sup> (Figure 25). A biphasic enzymatic progression curve of the inhibitors suggests a slow covalent binding. Notably, calpain inhibitors II and XII are dual inhibitors targeting both SARS-CoV-2 M<sup>Pro</sup> and human cathepsin L. Cathepsin L plays an important role in SARS-CoV-2 viral entry by activating the viral spike protein in the endosome or lysosome.<sup>70,71</sup> Studies have proven that cathepsin L inhibitors can substantially weaken virus entry.<sup>72</sup>

The crystal structures of calpain inhibitors XII (**118**) and II (**119**) with SARS-CoV-2 M<sup>Pro</sup> are available (PDB ID 6XFN and 6XA4),<sup>73</sup> as shown in Figure 26. These two compounds adopt an unusual binding mode compared with traditional M<sup>Pro</sup> inhibitors. Specifically, calpain inhibitors XII and II possess norvaline and hydrophobic methionine side chains at the P<sub>1</sub> position, respectively, which challenges the previous experience that a hydrophilic glutamine mimetic is necessary at the P<sub>1</sub> position and suggests that S<sub>1</sub> pocket of M<sup>Pro</sup> can accommodate both hydrophilic and hydrophobic substitutions. This new finding paves the way to design dual inhibitors targeting both SARS M<sup>Pro</sup> and human cathepsin L.

In the crystal structure of calpain inhibitor XII with M<sup>Pro</sup>, the length of the covalent bond between one ketone group of the inhibitor and Cys145 is 1.71 Å. The P<sub>1</sub>' pyridine is positioned in the S<sub>1</sub> site, while the P<sub>1</sub> norvaline takes the S<sub>1</sub>' site. The P<sub>2</sub> leucine is toward the solvent near residues 45–51, and the terminal carboxybenzyl group facing the S<sub>1</sub> site forces Asn142 upward and forms a water-mediated hydrogen bond with Glu166. The hydroxyl group establishes a strong hydrogen bond (2.41 Å) with the catalytic His41. The ketoamide O atom of the inhibitor forms a hydrogen bond with one residue in the oxyanion hole (2.94, 3.14, and 3.16 Å to the backbone amino of Gly143, Ser144, and Cys145, respectively), while the N atom accepts a hydrogen bond (3.04 Å) from the main chain carbonyl of His164 (Figure 26a). In the crystal structure of calpain



**Figure 24.** Cocystal structures of the covalent adducts of 112 (a, b), 113 (c, d), and 114 (e, f) bound to SARS-CoV M<sup>Pro</sup> or SARS-CoV-2 M<sup>Pro</sup> (PDB ID 2ZU4, 7JT7, and 2ZUS).

inhibitor II with M<sup>Pro</sup>, the length of the covalent bond between the aldehyde group and Cys145 is 1.70 Å. Like other peptidomimetic aldehyde inhibitors, the thiohemiacetal of calpain inhibitor II occupies the oxyanion hole consisting of the backbone amide groups of Gly143, Ser144, and Cys145. The inhibitor extends the length of the substrate-binding channel

with its side chains placed in their respective recognition pockets. The P<sub>2</sub> leucine side chain of the inhibitor forms hydrophobic interactions in the S<sub>2</sub> pocket, while the P<sub>3</sub> leucine occupies the solvent-accessible S<sub>3</sub> position. Multiple hydrogen bonds form between the amide backbone of the inhibitor and the main chain of His164 and Glu166.



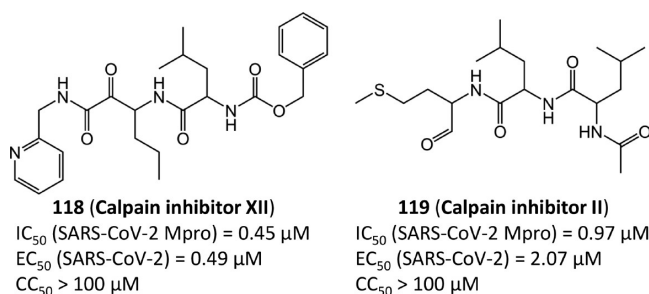


Figure 25. Calpain inhibitors.

The antiviral activity and cytotoxicity of the two calpain inhibitors are also available. The  $EC_{50}$  values of calpain inhibitors XII and II against SARS-CoV-2 are 0.49  $\mu$ M and 2.07  $\mu$ M, respectively. Additionally, their  $CC_{50}$  values are both over 100  $\mu$ M, representing low cytotoxicity.<sup>55</sup>

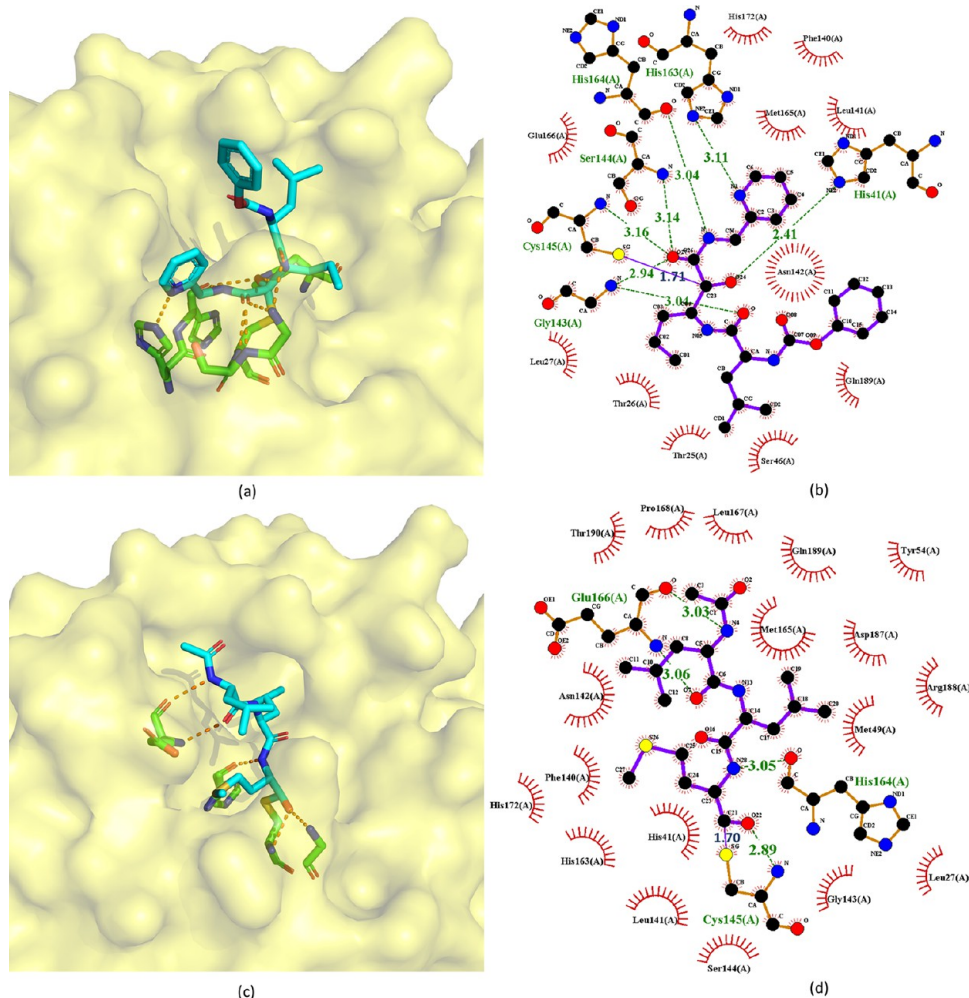
**2.1.5.1. Perspectives on Calpain Inhibitors.** The calpain inhibitors represent an interesting class of inhibitors considering their potential dual role as  $M^{pro}$  and cathepsin L inhibitors. Whereas many peptidic  $M^{pro}$  inhibitors place a pyrrolidinone moiety in the  $P_1$  position to form a hydrogen bond interaction with His163, the pyridine moiety of calpain inhibitor XII was shown to be a suitable replacement. A decrease in activity is seen with calpain inhibitor II, in which this side chain is replaced with

a methionine, which does not appear to be involved with a specific binding interaction according to the crystal structure. As seen with many peptide-aldehydes, the possible promiscuity of a reactive aldehyde functionality in inhibitor II may render the ketoamide XII the better lead agent in this series for further evaluation.

**2.2. Non-peptidomimetic Covalent Inhibitors.** Current existing non-peptidomimetic covalent inhibitors were developed by Ghosh et al.,<sup>74</sup> Wu et al.,<sup>75</sup> Zhang et al.,<sup>76</sup> and Niu et al.<sup>77</sup> Interestingly, all these inhibitors belong to the class of esters: 3-chloropyridine, 3-chloropyridyl, or benzotriazole esters (see Figures 27 and 28).

Based on their mass spectrometry experiments, Wu et al.<sup>75</sup> proposed an inhibition mechanism of these ester-derived inhibitors, which is depicted in Figure 29. Upon binding to  $M^{pro}$ , the ester is attacked by the nucleophilic cysteine (Cys145). The acyl group of the ester-derived inhibitor subsequently acylates the thiol of Cys145 and generates an inactive acylated  $M^{pro}$ . This mechanism is further confirmed by a recent crystal structure of MAC-5576 (152) bound to SARS-CoV-2  $M^{pro}$  (see Figure 30).<sup>65</sup> In this crystal structure, the activated group of MAC-5576 acylates Cys145.

Compounds 124 and 129–135 in Figure 27 are a series of benzotriazole esters synthesized by Wu et al. Their  $K_i$  values against SARS-CoV  $M^{pro}$  surveyed by the authors are also

Figure 26. Crystal structures of the covalent adducts of 118 (a, b) and 119 (c, d) bound to SARS-CoV-2  $M^{pro}$  (PDB ID 6XFN and 6XA4).

Compd	R <sub>1</sub>	R <sub>2</sub>	IC <sub>50</sub> (SARS-CoV Mpro)	K <sub>i</sub> (SARS-CoV Mpro)	EC <sub>50</sub> (SARS-CoV Mpro)
120			0.03 μM		6.9 μM
121			0.08 μM		12.1 μM
122			0.089 μM		
123			0.14 μM		
124			0.2 μM	0.0075 μM	NI
125			0.23 μM		25 μM
126			0.31 μM		24 μM
127			0.37 μM		
128			0.4 μM		NI
129				0.0111 μM	
130				0.0121 μM	
131				0.0123 μM	
132				0.0138 μM	
133				0.0174 μM	
134				0.0195 μM	
135				0.0229 μM	

**Figure 27.** 5-Chloropyridine ester and benzotriazole ester derived non-peptidomimetic covalent inhibitors from Ghosh et al.<sup>74</sup> and Wu et al.<sup>75</sup> NI represents no inhibition.

included in Figure 27. Especially **124** exhibits a  $K_i$  value as low as 0.0075 μM.<sup>75</sup> Additionally, Wu et al.'s cell-based assays at 100 μM suggested that these esters are not toxic to Vero E6 cells.<sup>78</sup> Notably, benzotriazole esters are well-known for their lability toward various nucleophiles, but the authors found that the compounds are relatively stable over 24 h in pH 5.0–8.0 at room temperature.<sup>75</sup>

Ghosh et al.<sup>74</sup> also focused on **124** and its derivatives. Consistent with the reported low  $K_i$  value,<sup>78</sup> **124** has a potent IC<sub>50</sub> value of 0.2 μM against SARS-CoV M<sup>Pro</sup>. However, as a drawback, the cell-based experiments suggested that **124** does not exhibit any SARS-CoV antiviral activity (see Figure 27, NI = no inhibition). Thus, Ghosh et al. developed more 3-chloropyridine esters derived from **124**, namely, **120–123** and **125–128** in Figure 27. Replacing the benzotriazole unit with a 3-chloropyridine unit, **126** shows comparable enzymatic inhibitory potency (IC<sub>50</sub> = 0.31 μM) with that of **124**. More

importantly, **126** has antiviral activity with an EC<sub>50</sub> of 24 μM. With the indole N atom acetylated, the resulting **128** remains potent against SARS-CoV M<sup>Pro</sup> (IC<sub>50</sub> = 0.4 μM) but without antiviral activity. Compound **127** contains a tosylated indole and has a IC<sub>50</sub> = 0.37 μM against SARS-CoV M<sup>Pro</sup>. Interestingly, its nitrobenzenesulfonamide analog **122** indicates a quite improved IC<sub>50</sub> value of 0.089 μM. The tetrahydroisoquinoline derivative **123** shows an IC<sub>50</sub> value of 0.14 μM.

Additional studies suggested that the carboxylic positions on the benzene ring of indole are critical for inhibitory potency against M<sup>Pro</sup>. Accordingly, carboxylate substitutions on indole rings at the 5-, 6-, 4-, and 7-positions result in chloropyridine esters **126**, **125**, **120**, and **121**, respectively. Of this series, inhibitor **120**, which contains a carboxylate at the 4-position, is the most potent inhibitor so far among all the existing non-peptidomimetic M<sup>Pro</sup> inhibitors with an IC<sub>50</sub> value of 0.03 μM, a 10-fold potency enhancement over **126**, which contains a carboxylate at the fifth position. Compound **121** is substituted with a carboxylate at the 7-position and exhibits an IC<sub>50</sub> value of 0.08 μM as well. Encouragingly, **120** and **121** show high antiviral activity with EC<sub>50</sub> values of 6.9 μM and 12.1 μM, respectively.

MAC-5576 (**152** in Figure 28) is another non-peptidomimetic inhibitor widely investigated. Its IC<sub>50</sub> against SARS-CoV M<sup>Pro</sup> is 0.5 μM.<sup>79</sup> A recent study found that it is even more potent against SARS-CoV-2 M<sup>Pro</sup> with an IC<sub>50</sub> of 0.081 μM. However, it does not block SARS-CoV-2 viral replication in cellular assays.<sup>65</sup> With MAC-5576 as the lead compound, Zhang et al.<sup>76</sup> and Niu et al.<sup>77</sup> developed tens of 5-chloropyridyl ester based inhibitors. Compounds **136**, **137**, **139–141**, **146**, **148**, and **150** were synthesized by Zhang et al.<sup>76</sup> Among them, compound **136** has an IC<sub>50</sub> of 0.05 μM against SARS-CoV M<sup>Pro</sup>. Through electrospray mass spectrometry experiments, they also suggested an inhibition mechanism identical to that from Wu et al.<sup>75</sup> as shown in Figure 29. Compounds **138**, **139**, **142–145**, **147**, **149**, **151**, and **153–155** are 5-chloropyridyl ester-based inhibitors developed by Niu et al.<sup>77</sup> Interestingly, these two research groups both reported that **138** has an IC<sub>50</sub> value of 0.63 μM. However, the antiviral activity of these compounds was not reported.

The SAR studies by Zhang et al.<sup>76</sup> and Niu et al.<sup>77</sup> of the compounds in Figure 28 indicate, besides a pyridinyl ring, a second aromatic ring (furan or thiophene) is also a key component for inhibiting SARS-CoV-2 and SARS-CoV M<sup>Pro</sup> potently.<sup>76</sup> More importantly, the positions of the electron-withdrawing substituents on the terminal aromatic rings dramatically impact inhibitory potency. Consistent with the mechanism shown in Figure 29, stronger electron-withdrawing R-groups, through either resonance or inductive effects, render a more electrophilic carbonyl of the ester warhead, resulting in stronger reactivity toward Cys145. For example, the difference in the positions of the N atom of the pyridine moiety relative to the carbonyl group in **145** and **155** causes a 4-fold disparity in their IC<sub>50</sub> values. Compound **138** has a nitro group at the para position relative to the furan group. Changing the nitro group of **138** to either the ortho (**147**) or the meta (**153**) position leads to a 3-fold or 8-fold increase in the IC<sub>50</sub> values, respectively. By contrast, **149**, **151**, and **154** bear a chloro- or a nitro-substituent on the benzene ring directly connected to the central ester group at the para, ortho, and meta positions relative to the ester bond, respectively. The position of the substituents in these three compounds has less impact on inhibiting SARS-CoV M<sup>Pro</sup>, although the meta-substituted **154** is a markedly weaker inhibitor than either **149** or **151**. Unlike the ketone and

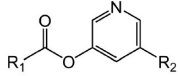
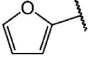
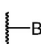
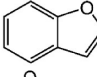
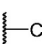
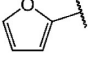
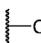
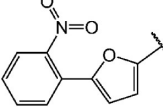
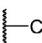
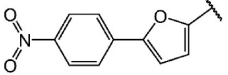
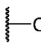
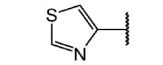
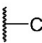
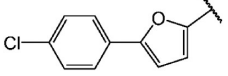
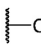
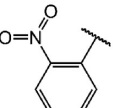
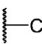
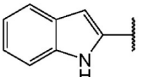
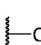
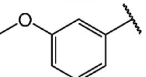
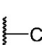
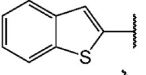
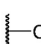
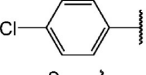
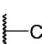
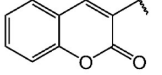
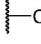
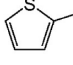
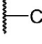
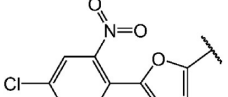
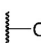
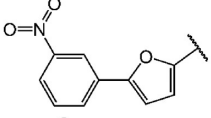
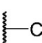
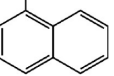
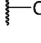
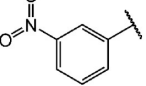
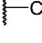
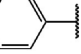
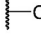
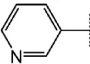
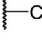
							
Compd	R <sub>1</sub>	R <sub>2</sub>	IC <sub>50</sub> (SARS-CoV Mpro)	Compd	R <sub>1</sub>	R <sub>2</sub>	IC <sub>50</sub> (SARS-CoV Mpro)
136			0.05 μM	146			0.17 μM
137			0.06 μM	147			0.208 μM
138			0.06 μM	148			0.27 μM
139			0.063 μM	149			0.333 μM
140			0.065 μM	150			0.34 μM
141			0.095 μM	151			0.434 μM
142			0.108 μM	152 (MAC 5576)			0.5 μM
143			0.122 μM	153			0.5 μM
144			0.124 μM	154			0.684 μM
145			0.164 μM	155			0.697 μM

Figure 28. 5-Chloropyridyl or 5-chloropyridine ester derived non-peptidomimetic covalent inhibitors from Zhang et al.<sup>76</sup> and Niu et al.<sup>77</sup>

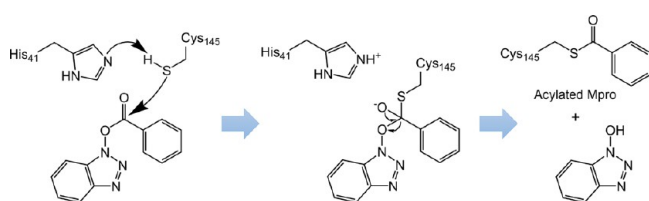


Figure 29. Proposed mechanism of the SARS-CoV M<sup>pro</sup> inhibition by acylation with ester-based inhibitors.

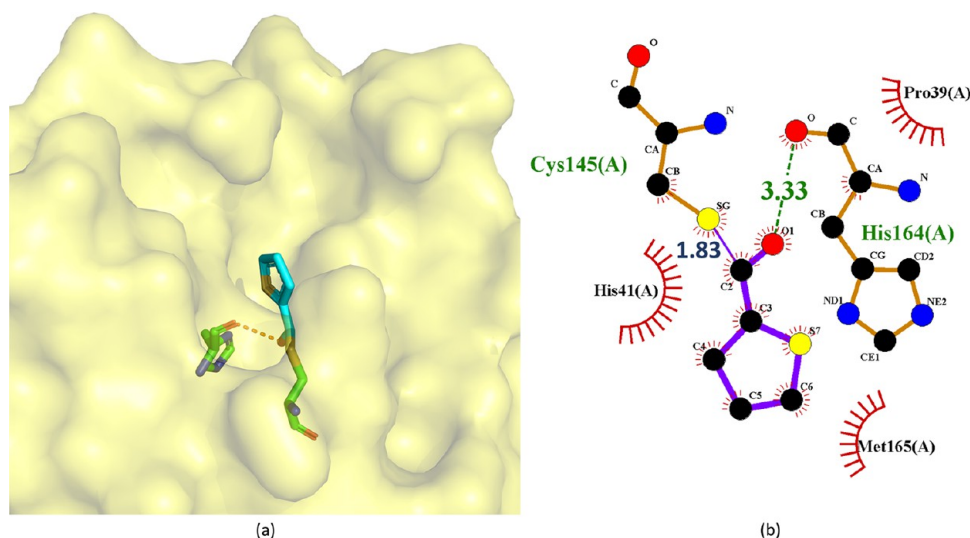
aldehyde-based inhibitors, these activated esters suffer from the elimination of a relatively large leaving group that may exhibit undesirable activities itself.

Very recently, Sun et al.<sup>80</sup> developed a series of ebselen and ebsulfur derivatives inhibiting SARS-CoV-2 M<sup>pro</sup> as shown in Figures 31 and 32. The kinetic progression curves of these isothiazolone-type covalent modifiers showed a biphasic character, indicating that the inhibition follows pseudo-first-order rate kinetics and implying ebselen, ebsulfur, and their derivatives covalently bind to M<sup>pro</sup>. Moreover, their assays also showed that these compounds irreversibly inhibit M<sup>pro</sup> and do not have significant activity recovery. Ebselen and ebsulfur are the most potent among these compounds with IC<sub>50</sub> values of 0.074 μM and 0.11 μM, respectively. Their K<sub>i</sub> values are 0.031

μM and 0.078 μM, respectively. Other experiments confirmed that ebselen potently inhibit SARS-CoV-2 with an IC<sub>50</sub> of 0.67 μM.<sup>81,82</sup> Additionally, Jin et al.<sup>81</sup> reported that ebselen has antiviral activity against SARS-CoV-2 with an EC<sub>50</sub> of 4.67 μM. The cytotoxicity of ebselen is also extremely low (the oral median lethal dose in rats is >4600 mg/kg).<sup>83</sup> Remarkably, the clinical evaluation of ebselen was recently initiated.<sup>84</sup>

**2.2.1. Drawbacks of the Current Non-peptidomimetic Covalent Inhibitors.** It should be noted that the current non-peptidomimetic covalent inhibitors lack specificity. The current non-peptidomimetic covalent inhibitors all contain isothiazolones. Isothiazolones have been labeled as some of the worst offenders as pan-assay interference compounds (PAINS) due to their high promiscuity.<sup>85</sup> Recent assays found that ebselen and some other non-peptidomimetic inhibitors interact with a panel of cysteine proteases.<sup>82</sup> Therefore, these leads should be carefully scrutinized to ensure that off-target effects do not cause serious consequences and that the proposed mechanism is responsible for the efficacy observed.

**2.3. Noncovalent M<sup>pro</sup> Inhibitors.** Since drugs acting through covalent modifications to the target may be associated with off-target liability and consequent potentially toxic effects,<sup>12</sup> research efforts have also been devoted to discovering noncovalent M<sup>pro</sup> inhibitors.



**Figure 30.** Crystal structure of the covalent complex of **152** (MAC-5576) with SARS-CoV-2 M<sup>pro</sup> (PDB ID 7JT0) through the acylation of Cys145 (a) and its corresponding 2D interaction diagram (b).

Compd	R	IC <sub>50</sub> (SARS-CoV-2 M <sup>pro</sup> )	K <sub>i</sub> (SARS-CoV-2 M <sup>pro</sup> )	EC <sub>50</sub> (SARS-CoV-2 M <sup>pro</sup> )
<b>156</b> (Ebselen)		0.074 μM 0.67 μM	0.031 μM	4.67 μM
<b>157</b>		0.13 μM		
<b>158</b>		0.15 μM		
<b>159</b>		0.24 μM		
<b>160</b>		0.26 μM		
<b>161</b>		0.33 μM		
<b>162</b>		0.35 μM		
<b>163</b>		0.41 μM		
<b>164</b>		0.52 μM		
<b>165</b>		0.65 μM		

**Figure 31.** Ebselen derived non-peptidomimetic covalent inhibitors.

**2.3.1. Aryl Boronic Acid Derivatives.** Some aryl boronic acid derivatives were found to be potent against SARS-CoV M<sup>pro</sup>. Compound **183** (Figure 33), bearing anilide linkages, is the best performing compound among aryl boronic acid derivatives ( $K_i = 0.04 \mu\text{M}$ ).<sup>86</sup>

**2.3.2. Isatin Derivatives.** Lai et al.<sup>87,88</sup> and Juang et al.<sup>89</sup> focused on developing N-substituted isatin derivatives as noncovalent SARS-CoV-2 and SARS-CoV M<sup>pro</sup> inhibitors (see Figure 34).

Compounds **184–186** are highly potent isatin inhibitors against SARS-CoV-2 M<sup>pro</sup> synthesized by Liu et al.<sup>87</sup> For instance, **184** has IC<sub>50</sub> of 0.045 μM against SARS-CoV-2 M<sup>pro</sup>. Lai et al.<sup>88</sup> revealed that **184** inhibits SARS-CoV M<sup>pro</sup> with IC<sub>50</sub> = 0.37 μM as well. Juang et al.<sup>89</sup> also synthesized a series of N-

substituted isatin derivatives. Compounds **187** and **188** were found to have promising IC<sub>50</sub> values against SARS-CoV.

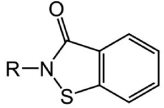
The extensive SAR investigation by Liu et al.<sup>87</sup> provided some suggestion concerning their binding requirements. First, due to space limitation in the M<sup>pro</sup> active site, substituents at R<sub>1</sub> and R<sub>2</sub> must be small. Second, hydrophobic groups at the R<sub>1</sub> position are necessary to ensure inhibitory effect. Finally, the carboxamide group at the R<sub>2</sub> position is essential for high potency (see Figure 34).

**2.3.3. Noncovalent Inhibitors Containing Benzotriazole.** Turlington et al.<sup>90</sup> developed a series of noncovalent M<sup>pro</sup> inhibitors containing benzotriazole based on their screening against the NIH molecular libraries sample collection. The potent ones are shown in Figure 35.

Notably, based on the crystal structure of SID24808289 with SARS-CoV M<sup>pro</sup> (PDB ID 4MDS), Turlington et al.'s SAR study<sup>90</sup> suggested that a 3-pyridyl heterocycle (see **190** and **191**) has potential to engage a side-chain interaction with the hydroxyl group of Thr24 or Thr25 of M<sup>pro</sup>. As a result, **190** and **191** inhibit SARS-CoV M<sup>pro</sup> with IC<sub>50</sub> values of 0.70 μM and 0.97 μM, respectively. Moreover, Turlington et al.<sup>90</sup> unexpectedly found that the parent simple phenyl biaryl (see **189**) increases activity by over 700-fold relative to **190** and **191** and represents the first sub-100 nM inhibitor in the series (IC<sub>50</sub> = 0.051 μM). This is probably because some unexpected hydrophobic interactions are formed. For example, our docking study suggested that the ring of the diaryl could form hydrophobic interactions with Ala46, Ile43, and Val42 of M<sup>pro</sup>.

**2.3.4. Anilide Based Inhibitors.** Among anilide based inhibitors, **192** (JMF1507) in Figure 36 displays the best potency with an IC<sub>50</sub> of 0.06 μM against SARS-CoV M<sup>pro</sup>. It is a competitive noncovalent inhibitor.<sup>91</sup>

**2.3.5. Noncovalent Aldehyde Peptide Inhibitors.** In addition to covalent aldehyde inhibitors described in section 2.1.3, there are also some noncovalent aldehyde peptide inhibitors reported by Akaji et al.<sup>92</sup> Covalent bonds are not formed with these inhibitors because the aldehyde groups are too far from the catalytic site Cys145 of SARS-CoV M<sup>pro</sup> in the crystal structures. For example, in the crystal structure of **193** with SARS-CoV M<sup>pro</sup> (PDB ID 3AVZ, Figure 38a,b), the C atom of the aldehyde group is 2.23 Å from the S atom of Cys145, while for **194** (PDB



Compd	R	IC <sub>50</sub> (SARS-CoV-2 Mpro)	K <sub>i</sub> (SARS-CoV-2 Mpro)	Compd	R	IC <sub>50</sub> (SARS-CoV-2 Mpro)
<b>166</b> (Ebsulfur)		0.11 μM	0.078 μM	<b>175</b>		0.41 μM
<b>167</b>		0.13 μM		<b>176</b>		0.48 μM
<b>168</b>		0.17 μM		<b>177</b>		0.49 μM
<b>169</b>		0.23 μM		<b>178</b>		0.63 μM
<b>170</b>		0.33 μM		<b>179</b>		0.66 μM
<b>171</b>		0.36 μM		<b>180</b>		0.73 μM
<b>172</b>		0.38 μM		<b>181</b>		0.78 μM
<b>173</b>		0.39 μM		<b>182</b>		0.91 μM
<b>174</b>		0.41 μM				

Figure 32. Ebsulfur derived non-peptidomimetic covalent inhibitors.

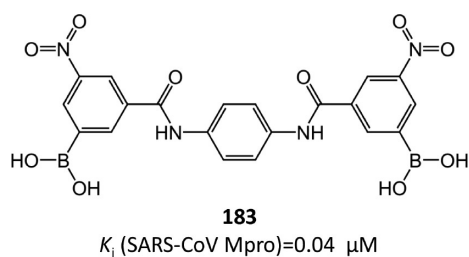
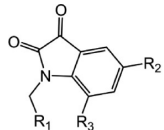


Figure 33. Most potent noncovalent M<sup>Pro</sup> inhibitor among aryl boronic acid derivatives.

ID 3ATW, Figure 38c,d), this distance is 2.48 Å (see Figure 38). Considering that the length of a regular C–S bond is around 1.8 Å, their distances are not close enough to form strong covalent interactions.

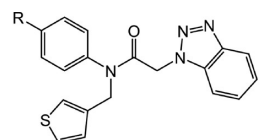
Some of these noncovalent aldehyde inhibitors are still potent against SARS-CoV M<sup>Pro</sup> (Figure 37). Akaji et al.<sup>92</sup> designed these noncovalent aldehyde inhibitors via SAR analysis. First, they found that a bulky group at the side chain of the P<sub>2</sub> site could fit into the S<sub>2</sub> pocket more tightly than other groups, which leads to **193** and **197** with IC<sub>50</sub> values of 0.065 μM and 0.39 μM, respectively. Notably, the comparison between **193** and **197** suggests that the substitution with a cyclohexyl group is more effective than that with a planar aromatic group. This is probably because a cyclohexyl group is more adjustable to more strongly interact with the S<sub>2</sub> pocket. Second, the outwardly directed P<sub>5</sub> site could be removed to lower the molecular weight of the



Compd	R <sub>1</sub>	R <sub>2</sub>	R <sub>3</sub>	IC <sub>50</sub> (SARS-CoV-2 Mpro)	IC <sub>50</sub> (SARS-CoV Mpro)
<b>184</b>				0.045 μM	0.37 μM
<b>185</b>				0.047 μM	
<b>186</b>				0.053 μM	
<b>187</b>					0.95 μM
<b>188</b>					0.98 μM

Figure 34. N-Substituted isatin derivatives as noncovalent SARS-CoV-2 and SARS-CoV M<sup>Pro</sup> inhibitors.

inhibitors since no interactions of the corresponding side chains to the protease are detected. This strategy resulted in **195**, whose activity is a bit better than that of **197**. Third, to attach the P<sub>5</sub> site-deleted inhibitors to the active-site cleft more tightly, a secondary alcohol moiety was introduced into the side chain of the P<sub>4</sub> site to form more hydrogen bonds with M<sup>Pro</sup>, which results in **194**. Compound **194** has almost the same activity



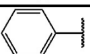
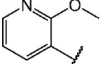
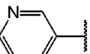
Compd	R	IC <sub>50</sub> (SARS-CoV Mpro)
189		0.051 μM
190		0.70 μM
191		0.97 μM

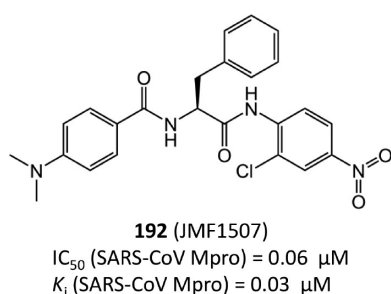
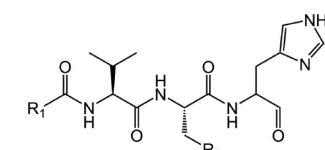
Figure 35. Noncovalent M<sup>pro</sup> inhibitors containing benzotriazole.

Figure 36. Most potent anilide based inhibitor.



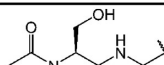
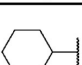
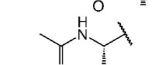
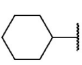
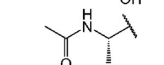
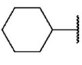
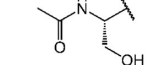
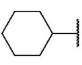
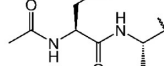
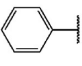
Compd	R <sub>1</sub>	R <sub>2</sub>	IC <sub>50</sub> (SARS-CoV Mpro)
193			0.065 μM
194			0.098 μM
195			0.27 μM
196			0.34 μM
197			0.39 μM

Figure 37. Noncovalent aldehyde inhibitors.

(IC<sub>50</sub> = 0.098 μM) as **193** (IC<sub>50</sub> = 0.065 μM), while the molecular weight is reduced (534 vs 591).

The potent inhibition of these compounds against M<sup>pro</sup> is due to their tight hydrogen-bond interactions with M<sup>pro</sup>.<sup>92</sup> As shown in the crystal structures of **193** and **194** with SARS-CoV M<sup>pro</sup> (see Figure 38), the imidazole N atom at the P<sub>1</sub> site accepts a hydrogen bond from M<sup>pro</sup> His163. As a result, the other side of the imidazole inserts into the S<sub>1</sub> pocket formed by the side chains of Phe140, Leu141, and Glu166. The cyclohexyl group at the P<sub>2</sub> site occupies most of the sizable S<sub>2</sub> pocket consisting of His41, Met49, Met165, and Asp187. The amide-bound N and carbonyl O atoms of the P<sub>3</sub> site have hydrogen bonds with the

main chain of Glu166. The amide-bound N atom of the P<sub>4</sub> site also accepts another hydrogen bond from Thr190 of M<sup>pro</sup>. In the structure of **193** with M<sup>pro</sup>, an additional hydrogen bond (3.19 Å) can also be found between the side-chain O atom at the P<sub>4</sub> site and Thr190. Notably, along with a secondary alcohol moiety introduced at the P<sub>4</sub> site, a strong hydrogen bond (2.69 Å) is formed between this alcohol moiety and Thr190 of M<sup>pro</sup>, which agrees with the SAR analysis by Akaji et al.<sup>92</sup>

**2.3.5.1. Drawbacks of Noncovalent Aldehyde Peptide Inhibitors.** Ample evidence suggests that the aldehyde in these agents does not form a stable covalent bond with the protease. Considering the reactive and promiscuous nature of aldehydes in general, it may be advantageous to replace this liability. Compared to the nonpeptidic and noncovalent inhibitors, these peptide-based inhibitors may also be limited by their *in vivo* instability and poor membrane permeability.

**2.3.6. Symmetric Peptides and Molecules.** TL-3 (**200** in Figure 39) is a C-2 symmetric peptide-based dimer that was identified as a human immunodeficiency virus (HIV) protease inhibitor. Wu et al.<sup>78</sup> found that it is also active against SARS-CoV M<sup>pro</sup> with a K<sub>i</sub> value of 0.6 μM.

With TL-3 as the lead structure, Shao et al.<sup>93</sup> developed several symmetric peptide-based SARS-CoV M<sup>pro</sup> inhibitors. Among them, **198** and **199** in Figure 39 have stronger efficacy than TL-3 with K<sub>i</sub> values of 0.073 and 0.34 μM, respectively.

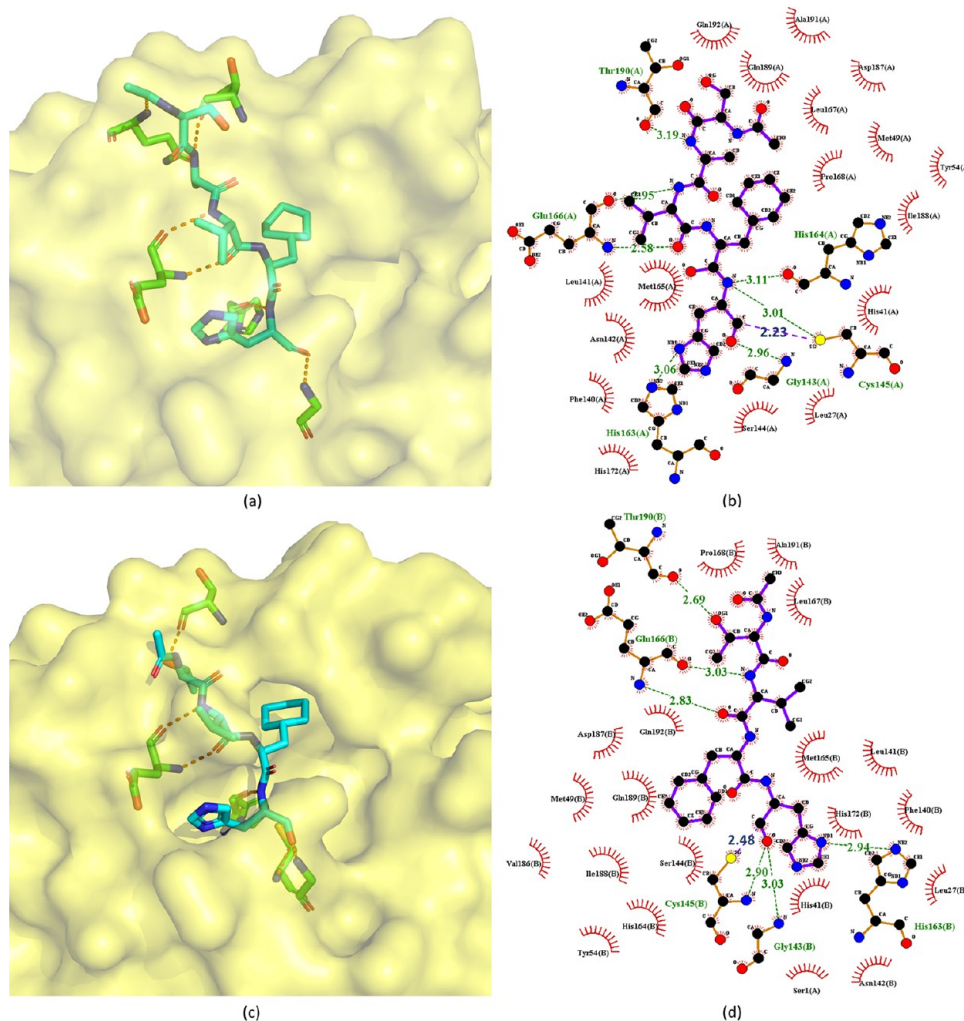
Besides symmetric peptides, other symmetric molecules were also identified as SARS-CoV-2 and SARS-CoV M<sup>pro</sup> inhibitors. For instance, recently Coelho et al.<sup>94</sup> have found that Evans blue, a sulfonic acid-containing dye, is highly active against SARS-CoV-2 M<sup>pro</sup> with IC<sub>50</sub> = 0.2 μM and K<sub>i</sub> = 0.21 μM (**201** in Figure 39). Interestingly, Evans blue has been previously reported to inhibit HIV<sup>95</sup> and hepatitis B virus (HBV).<sup>96</sup> In addition, symmetric inhibitor **202**, as one of a series of diarylsulfonyl compounds in Figure 39, has a reported IC<sub>50</sub> = 0.9 μM against SARS-CoV M<sup>pro</sup>.<sup>97</sup> However, the acylated phenol **201** is likely susceptible to hydrolysis or other nucleophiles, which may compromise its cellular and *in vivo* efficacy.

**2.3.7. Aromatic-Disulfide Based Inhibitors.** Wang et al.<sup>98</sup> synthesized a series of novel aromatic disulfides and evaluated their enzymatic activities against SARS-CoV M<sup>pro</sup>. Notably, disulfide compounds have the potential to react with other thiols, including Cys145, and form new -S-S- covalent bonds. However, according to their experiments,<sup>98</sup> different aryl thiols derived from the disulfides exhibit no efficacy against SARS-CoV M<sup>pro</sup> even at very high concentration. Also, no molecular weight change of M<sup>pro</sup> was detected before and after the reactions. These two results suggest that the interaction of M<sup>pro</sup> to their aromatic-disulfide based inhibitors is of a noncovalent nature.

Aromatic disulfide-based inhibitors with potency in the micromolar range are illustrated in Figure 40. The best IC<sub>50</sub> value among them is 0.516 μM (**203**).

**2.3.7.1. Drawbacks of Aromatic-Disulfide Based Inhibitors.** No cellular activity was reported for the aromatic-disulfide based inhibitors. It would be interesting to see the translational efficacy of these agents as multiple reductases and high levels of endogenous glutathione are known to readily clean disulfides *in vivo*, which may significantly affect the overall efficacy of aromatic-disulfide based inhibitors.<sup>99</sup> These electrophilic aryl disulfide-based species are also prone to nucleophilic attack by other species, and therefore, undesirable sulfenylation events are likely to occur.

**2.3.8. Other Noncovalent M<sup>pro</sup> Inhibitors.** Walrycin B (**208** in Figure 41) is an analog of toxoflavin. Recent repurposing



**Figure 38.** Crystal structures of **193** (a, b) and **194** (c, d) bound to SARS-CoV M<sup>Pro</sup> (PDB ID 3AVZ and 3ATW).

work<sup>100</sup> found that walrycin B also strongly inhibits SARS-CoV-2 M<sup>Pro</sup> with  $IC_{50} = 0.26 \mu\text{M}$  and more importantly shows potent antiviral activity against SARS-CoV-2 with  $EC_{50} = 3.55 \mu\text{M}$ . However, its  $CC_{50}$  of  $4.25 \mu\text{M}$  suggests it may be highly cytotoxic.

Compound **209** was identified from high-throughput screening performed by Lu et al.<sup>97</sup> and has  $IC_{50} = 0.3 \mu\text{M}$  against SARS-CoV M<sup>Pro</sup>. Compound **210** belongs to a series of keto-glutamine analogs synthesized by Jain et al.<sup>101</sup> and displays reversible inhibition against SARS-CoV M<sup>Pro</sup> with  $IC_{50} = 0.6 \mu\text{M}$ . The flavonoid baicalein (**211**) is one ingredient of traditional Chinese medicine shuanghuanglian. Su et al.<sup>102</sup> reported that it also exhibits activity against SARS-CoV-2 M<sup>Pro</sup> with an  $IC_{50}$  of  $0.94 \mu\text{M}$  and antiviral activity with an  $EC_{50}$  of  $2.94 \mu\text{M}$ . However, its cytotoxicity was reported with  $CC_{50} = 86 \mu\text{M}$  in Vero cells.<sup>103</sup>

The crystal structures of **209** and **211** (baicalein) bound to SARS-CoV or SARS-CoV-2 M<sup>Pro</sup> are available with PDB ID 2GZ7 and 6M2N, respectively. In crystal structure 2GZ7 (Figure 42a,b), **209** occupies the  $S_3$ – $S_5$  pockets of SARS-CoV M<sup>Pro</sup>. The 2,4-dichloro-5-methylbenzene group sits deeply inside the hydrophobic pocket consisting of Pro39, His41, Cys145, His163, His164, Phe181, Tyr182, and Phe185. The phenyl ring of **208** has strong  $\pi$ – $\pi$  interactions with the side chain of His41, while the dichloro and methyl groups are close to Cys145, His164, Pro39, and Leu27. Moreover, the 1,3-

dinitro-5-(trifluoromethyl) benzene group forms strong hydrogen-bond interactions with M<sup>Pro</sup>. In particular, one nitro group has a hydrogen bond with the N atom in the side chain of His41 and two hydrogen bonds with Met49 and His41 through a water molecule. The trifluoromethyl substituent generates a weak hydrogen bond with Gln192 and is adjacent to Gln192, Gln189, Leu167, and Met165. Moreover, the benzene group forms hydrophobic interactions with Met165, while the sulfone group has hydrogen-bond interactions with a water molecule.<sup>97</sup>

In the crystal structure of baicalein (**211**) in complex with SARS-CoV-2 M<sup>Pro</sup>, the baicalein binds to the surface of the protease between domains I and II, which is the core region of the binding site (Figure 42c,d). Three phenolic hydroxyl groups of baicalein form multiple hydrogen bonds with the main chains of Leu141 and Gly143 and the side chains of Ser144 and His163. The carbonyl group of baicalein leads to a hydrogen bond with the main chain of Glu166, while the free phenyl ring is inside the  $S_2$  subsite and forms hydrophobic interactions with Gln189, Arg188, Met49, Cys44, and His41. Notably, in addition to the hydrophobic interactions, the catalytic His41 and Cys145 also establish  $S$ – $\pi$  and  $\pi$ – $\pi$  interactions with the aromatic rings of baicalein. The side chain of Asn142 also forms  $NH_2$ – $\pi$  interactions with baicalein. These interactions, together with the interactions with Cys145, sandwich the phenyl ring of baicalein with three OH groups between Asn142 and Cys145. Moreover, Met165 has hydrophobic interactions with the

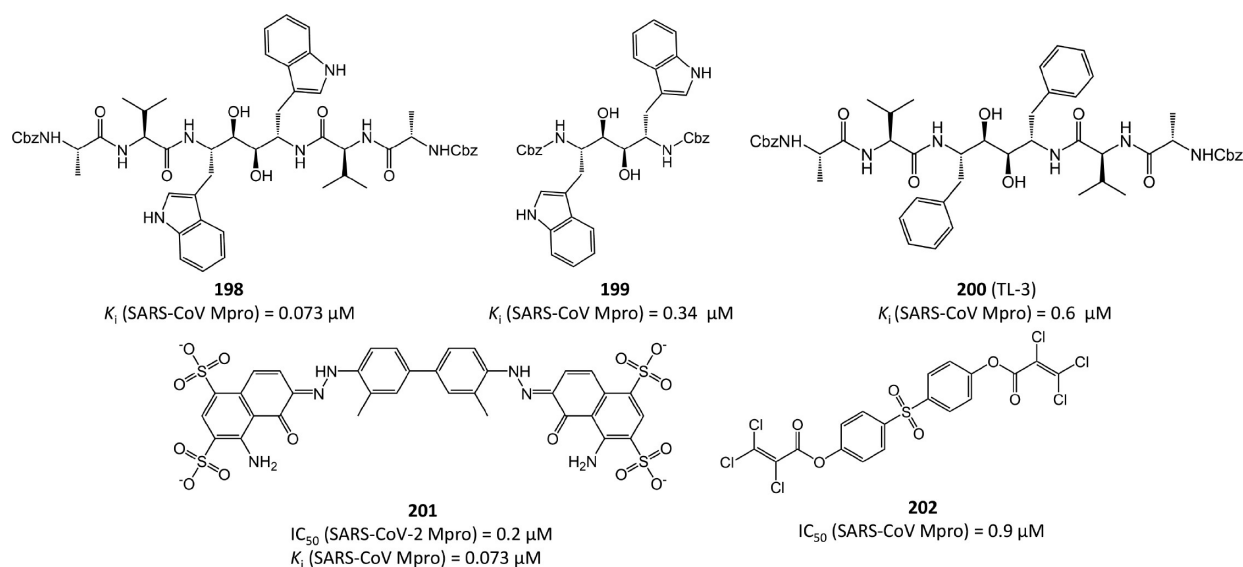


Figure 39. Symmetric peptides and molecules.

middle ring of baicalein. As a result, baicalein blocks two catalytic residues, as well as the oxyanion loop (residues 138–145), Glu166, and the  $S_1$  and  $S_2$  subsites, thereby preventing  $M^{pro}$  from recognizing substrates.

**2.3.8.1. Drawbacks of Walrycin B and Baicalein.** Walrycin B (**208**) is not only highly cytotoxic but also an analog of toxoflavin, which is a well-known offender in the arena of PAINS.<sup>85</sup> Considering its promiscuous reactivity, the observed efficacy and how it correlates to a proposed mechanism should therefore be treated with severe caution. Baicalein (**211**) is also reported to have some cytotoxicity. More importantly, baicalein has promiscuity risks and is known to inhibit numerous substrates.<sup>102</sup>

**2.4. Metal Conjugated SARS-CoV-2 or SARS-CoV  $M^{pro}$  Inhibitors.** As shown in Figure 43, **212**–**218** with conjugated  $Zn^{2+}$  or  $Hg^{2+}$  ions also show inhibitory potency in the sub-micromolar range against SARS-CoV-2  $M^{pro}$  or SARS-CoV  $M^{pro}$ .<sup>94,104,105</sup> Notably, the crystal structures of metal conjugated inhibitors bound to  $M^{pro}$  reveals that, after binding, the inhibitors are always dissociated and the metals covalently attach to  $M^{pro}$  residues such as Cys145 (see Figure 44).

Compounds **212**–**214** are good examples to depict their binding modes to  $M^{pro}$ . In the  $M^{pro}$ –JMF1586 (**212**) complex (Figure 44a,b), His41, Cys145, and two N atoms of the compound make up the Zn-centered tetrahedral coordination, in which two N and two O atoms chelate the Zn atom. In the  $M^{pro}$ –JMF1600 (**213**) complex (Figure 44c,d), His41, Cys145, one N atom, and a water molecule participate in the Zn coordination. The Zn atom is chelated by one N and three O atoms of JMF1600. A Zn–N bond is stronger than a Zn–O bond, which is consistent with the lower  $K_i$  value of JMF1586 than JMF1600. Both these 3D structures indicate that the metal–O bonds of JMF1586 and JMF1600 must be broken before being replaced by His41 and Cys145 to form the Zn-centered complex. In the  $M^{pro}$ –phenylmercuric acetate (**214**) complex structure (Figure 44e,f), the phenyl-bound mercury is bound to the S atom of Cys44 with a bond distance of 2.47 Å. The phenolic O atom of Tyr54 is another site to accept a 2.56 Å Hg–O bond from **214**, while its acetate group is dissociated and substituted by protein residues.

Compd	$R_1-S-S-R_2$		$IC_{50}$ (SARS-CoV Mpro)	$K_i$ (SARS-CoV Mpro)
	$R_1$	$R_2$		
203			0.516 $\mu$ M	0.24 $\mu$ M
204			0.684 $\mu$ M	
205			0.697 $\mu$ M	
206			0.883 $\mu$ M	
207			0.921 $\mu$ M	

Figure 40. Aromatic-disulfide based inhibitors.

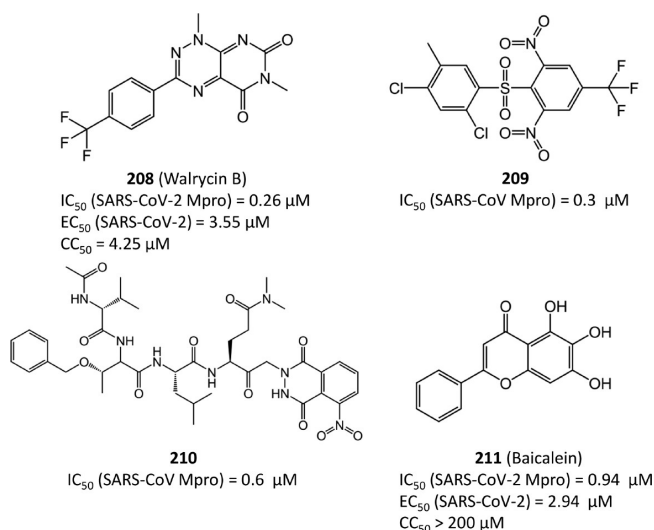


Figure 41. Other noncovalent  $M^{pro}$  inhibitors.



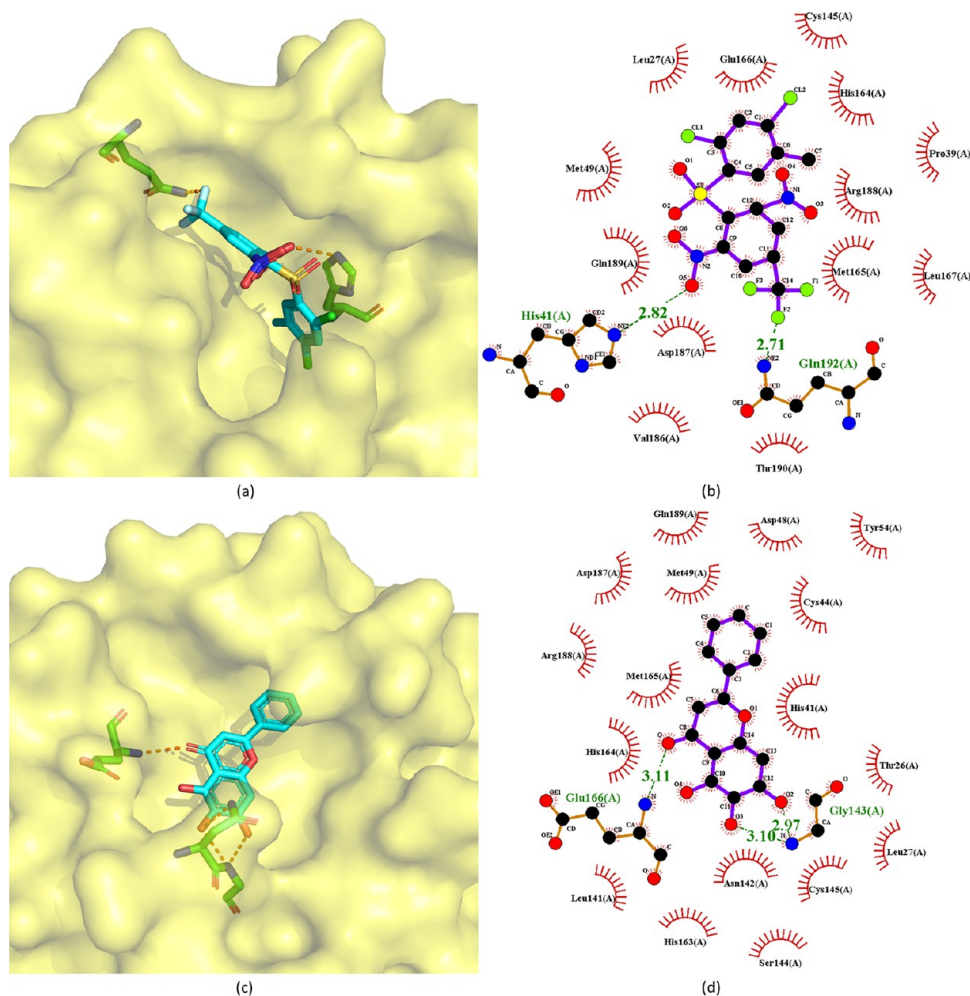


Figure 42. Crystal structures of **209** (a, b) and **211** (c, d) bound to SARS-CoV-2 M<sup>Pro</sup> (PDB ID 2GZ7 and 6M2N).

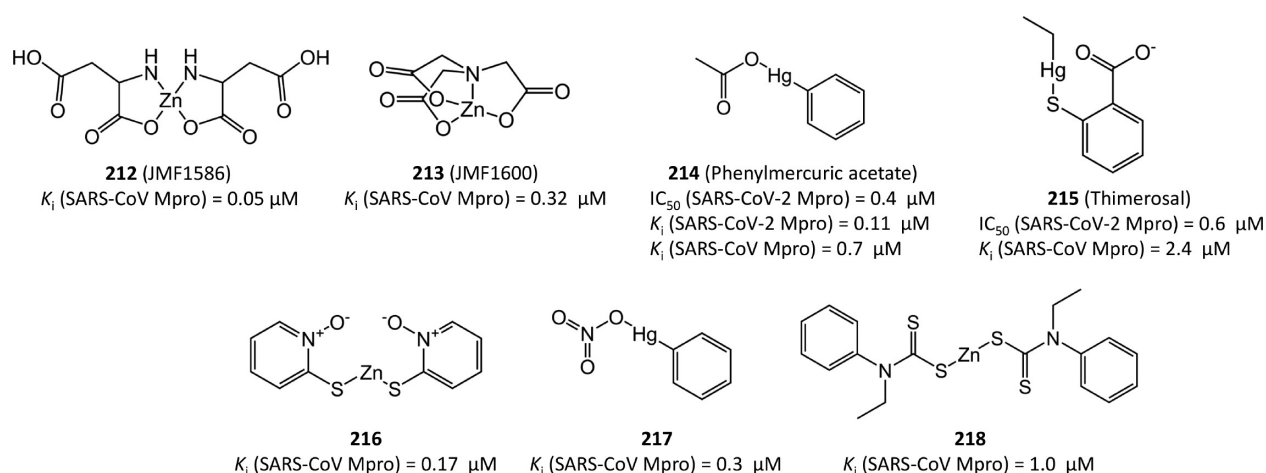
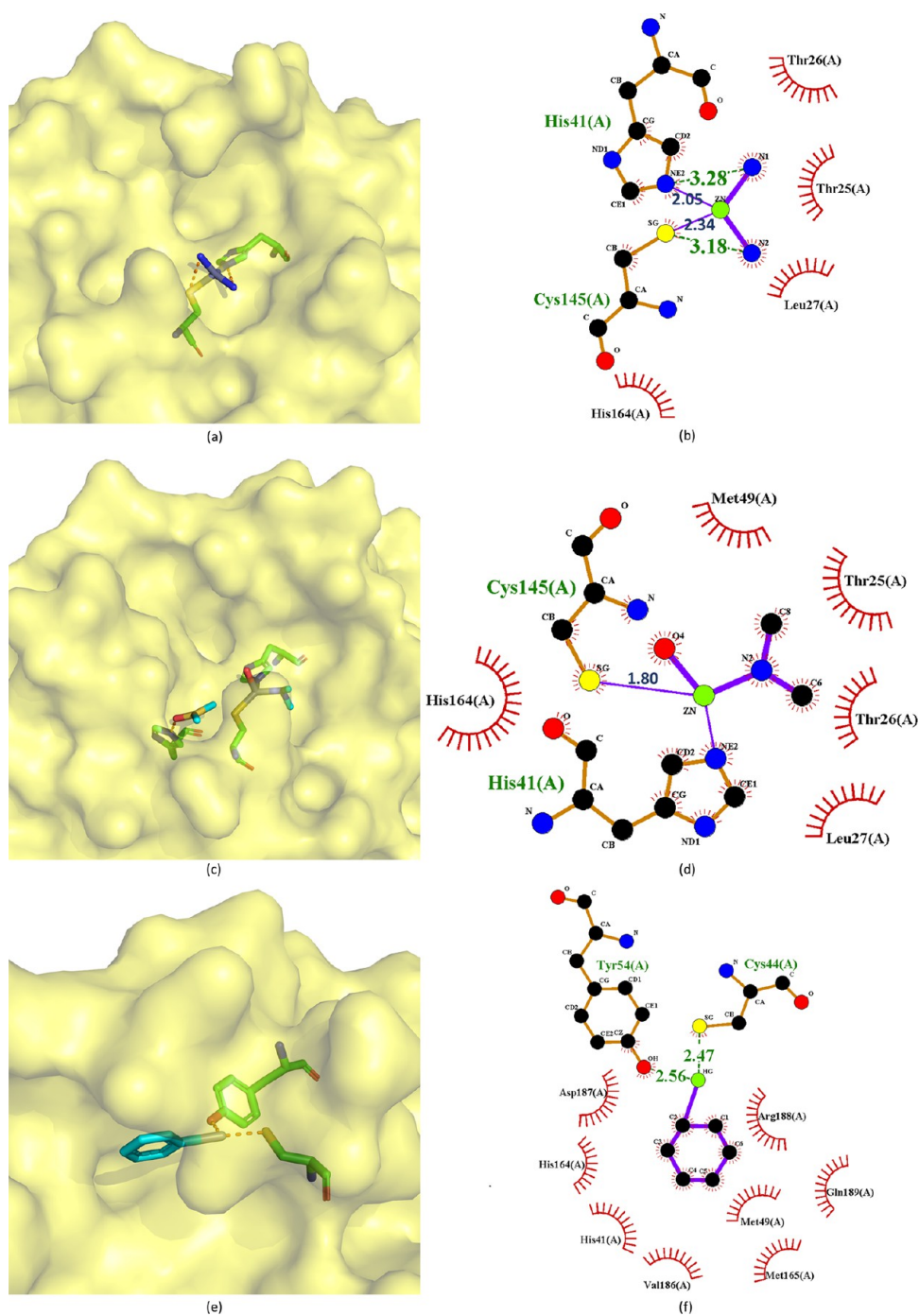


Figure 43. Metal conjugated SARS-CoV-2 or SARS-CoV M<sup>Pro</sup> inhibitors.

**2.4.1. Perspectives on Metal Conjugated Inhibitors.** Metal conjugated inhibitors provide an interesting class of lead agents and are often improperly labeled as toxic agents. However, phenylmercuric acetate and thimerosal are used as pharmaceutical excipients, and several other metal conjugates have been used as topical antimicrobial preservatives. The anticipated toxicity of metals depends on many factors, including their oxidation states.

### 3. DISCUSSION AND PERSPECTIVES

COVID-19 caused by SARS-CoV-2 is one of the most deadly pandemics since the new millennium. It has overwhelmed the worldwide healthcare system and devastated the global economy. Currently, there is no approved medication against the virus; thus it is imperative to discover potential therapeutic agents against SARS-CoV-2.



**Figure 44.** Crystal structures of **212** (a, b), **213** (c, d), and **214** (e, f) bound to SARS-CoV-2 M<sup>Pro</sup> (PDB ID 2Z9L, 2Z9K and 2Z9G).

The main protease (M<sup>Pro</sup>) is not only critical for viral replication but also highly conserved in viral evolution. Therefore, M<sup>Pro</sup> is one of the most attractive targets for developing antiviral therapies. A large number of M<sup>Pro</sup> inhibitors have been reported since the outbreak of SARS-CoV in 2003. To provide a whole landscape of the current status of SARS-CoV-2 and SARS-CoV inhibitors, here we collect all available SARS-CoV-2 and SARS-CoV M<sup>Pro</sup> inhibitors so far from literature or databases. We highlight highly potent inhibitors, analyze their structures and functions, and illustrate their covalent or noncovalent binding interactions with M<sup>Pro</sup>. The optimization of inhibitors to improve potency is also discussed. To serve as a good starting point to design new drugs against SARS-CoV-2,

we classify M<sup>Pro</sup> inhibitors into different categories based on their molecular mechanisms of action, such as small-molecule covalent inhibitors, peptidomimetic covalent inhibitors, non-covalent inhibitors, and metal conjugated inhibitors.

**3.1. Drug Development Potential of Existing SARS-CoV-2 and SARS-CoV M<sup>Pro</sup> Inhibitors.** So far, more than 800 SARS-CoV-2 and SARS-CoV M<sup>Pro</sup> inhibitors are available, and this data set is provided in the [Supporting Information](#). The classification of these inhibitors is summarized in [Table 1](#). Considering that the binding sites of SARS-CoV-2 and SARS-CoV M<sup>Pro</sup> are almost identical, SARS-CoV M<sup>Pro</sup> inhibitors are also effective to SARS-CoV-2.

**Table 1. Classification of Current SARS-CoV-2 and SARS-CoV M<sup>Pro</sup> Inhibitors**

class	subclass	ref	
covalent	peptidomimetic ketone	26,34,35,38–40,106–112	
	peptidomimetic nitrile-containing	43	
	peptidomimetic aldehyde	45,48,49,51–53	
	peptides with aldehyde bisulfite	50,65,113	
	peptidomimetic michael acceptors	29,64,66,67,114–116	
	nonpeptidomimetic covalent inhibitors	74–77,79,80,117	
	noncovalent	aryl boronic acid derivative	86
		istin based	87–89,118
		benzotriazole based	90
		anilide	91
aldehyde		92	
symmetric peptide or molecule		78,93	
aromatic disulfide		98	
ketone		119	
others		4,81,82,94,97,100–102,120–155	
metal conjugated		94,104,105	

However, many M<sup>Pro</sup> inhibitors cannot be developed into effective drugs due to their unqualified potency, promiscuity, toxicity, side effects, or poor ADME properties. Current inhibitors with drug development potential fall mostly in the class of peptidomimetic covalent inhibitors. The most promising ones are nitrile-containing inhibitor PF-07321332 and HMK inhibitor PF-00835231. Both of them are now in clinical trials. In particular, PF-07321332 is projected to reach the market relatively soon. Aldehyde bisulfite GC376 was also reported to have druggable potential but may require further evaluation to determine if aldehyde bisulfates offer the selectivity profile needed for clinical development.

High-throughput screening efforts have identified many hits, which have resulted in many rapid reports. Unfortunately, this has also resulted in the identification of many known PAINS as possible drug leads. For example, there are several non-peptidomimetic covalent inhibitors that contain the classic isothiazolone scaffold. These isothiazolones have also been labeled as some of the worst offenders as PAINS due to their high promiscuity. Toxoflavin is another well-known offender in the arena of PAINS. A reactive aldehyde functionality could possibly render promiscuity, too. Therefore, caution should be taken in the pursuit of these agents as SARS-CoV-2 M<sup>Pro</sup> inhibitors.

**3.2. M<sup>Pro</sup> Mutation Impact on Inhibitor Efficacy.** We collected 1 983 328 complete SARS-CoV-2 sequences with exact collection dates submitted to GISAID up to September 20, 2021. After applying the multiple sequence alignment (MSA) technique, we obtained the single nucleotide polymorphism (SNP) information on these 1 983 328 complete SARS-CoV-2 sequences, in which a total of 28 780 unique single mutations on the whole SARS-CoV-2 genome were identified. Among them, 1395 unique single mutations were detected on M<sup>Pro</sup>, where 906 unique single mutations were missense mutations and 489 unique single mutations were silent mutations.

Although SARS-CoV-2 M<sup>Pro</sup> admits more than ten different inhibitor binding sites, there is only one major inhibition site.<sup>30</sup> The crystal structure of SARS-CoV-2 M<sup>Pro</sup> in complex with boceprevir is available with PDB ID 7C6S. We identify the binding domain of M<sup>Pro</sup> to be the residues located in the sphere of 10 Å radius around the center of small molecule boceprevir. Then, the number of silent mutations ( $N_{\text{silent}}$ ) and missense mutations ( $N_{\text{Missense}}$ ) in the binding domain can be found in Table 2. A total of 78 missense mutations were detected in the

**Table 2. Number of the Silent Mutations ( $N_{\text{silent}}$ ), Missense Mutations ( $N_{\text{missense}}$ ), and Unique Single Mutations ( $N_{\text{total}}$ ) on the M<sup>Pro</sup>, Binding Domain of M<sup>Pro</sup>, and Non-binding Domain of M<sup>Pro</sup>**

location	$N_{\text{silent}}$	$N_{\text{missense}}$	$N_{\text{total}}$
M <sup>Pro</sup>	489	906	1395
binding domain	59	78	137
non-binding domain	430	828	1258

binding domain of M<sup>Pro</sup>, and we list the top 10 highest frequency missense mutations in the binding domain and nonbinding domain of M<sup>Pro</sup> in Table 3 and Table 4. It can be seen that the

**Table 3. Top 10 Missense Mutations on the Binding Domain of M<sup>Pro</sup><sup>a</sup>**

SNP	protein mutation	total frequency	ratio
10202C→T	L50F	969	0.00049
10610G→T	V186F	749	0.00038
10188C→T	T45I	636	0.00032
10623C→T	T190I	601	0.00030
10201G→T	M49I	427	0.00022
10191C→T	S46F	416	0.00021
10128C→T	T25I	93	0.00005
10617G→A	R188K	77	0.00004
10190T→C	S46P	52	0.00003
10196G→A	D48N	51	0.00003

<sup>a</sup>The frequency is the number of complete SARS-CoV-2 sequences that carry a specific mutation, and the ratio is defined by the frequency of a specific mutation over the total number of complete SARS-CoV-2 sequences.

**Table 4. Top 10 Missense Mutations in the Nonbinding Domain of M<sup>Pro</sup><sup>a</sup>**

SNP	protein mutation	total frequency	ratio
10319C→T	L89F	60078	0.03029
10323A→G	K90R	38117	0.01922
10097G→A	G15S	9695	0.00489
10833C→T	A260V	5068	0.00256
10376C→T	P108S	4837	0.00244
10667T→G	L205V	4135	0.00208
10193G→A	E47K	3947	0.00199
10195A→T	E47D	3880	0.00196
10277C→T	L75F	2985	0.00151
10533G→T	C160F	2904	0.00146

<sup>a</sup>The frequency is the number of complete SARS-CoV-2 sequences that carry a specific mutation, and the ratio is defined by the frequency of a specific mutation over the total number of complete SARS-CoV-2 sequences.

frequency of missense mutations in the binding domain of  $M^{P_{70}}$  is much lower than that in the nonbinding domain of  $M^{P_{70}}$ , indicating that the binding domain is more conserved than the nonbinding domain. The 10202C→T-(L50F) mutation with the highest frequency in the binding domain of  $M^{P_{70}}$  only has a ratio of 0.00049.

## ■ ASSOCIATED CONTENT

### SI Supporting Information

The Supporting Information is available free of charge at <https://pubs.acs.org/doi/10.1021/acs.jmedchem.1c00409>.

Prediction of ADMET, PK, and druggability properties and summary of the 817 SARS-CoV-2 and SARS-CoV  $M^{P_{70}}$  inhibitors with SMILES strings, potency information, cytotoxicity, structure availability with PDB ID, names, and references (PDF)

## ■ AUTHOR INFORMATION

### Corresponding Author

**Guo-Wei Wei** – Department of Mathematics, Department of Biochemistry and Molecular Biology, and Department of Electrical and Computer Engineering, Michigan State University, East Lansing, Michigan 48824, United States; [orcid.org/0000-0002-5781-2937](https://orcid.org/0000-0002-5781-2937); Email: [wei@math.msu.edu](mailto:wei@math.msu.edu)

### Authors

**Kaifu Gao** – Department of Mathematics, Michigan State University, East Lansing, Michigan 48824, United States; [orcid.org/0000-0001-7574-4870](https://orcid.org/0000-0001-7574-4870)

**Rui Wang** – Department of Mathematics, Michigan State University, East Lansing, Michigan 48824, United States; [orcid.org/0000-0002-7402-6372](https://orcid.org/0000-0002-7402-6372)

**Jiahui Chen** – Department of Mathematics, Michigan State University, East Lansing, Michigan 48824, United States; [orcid.org/0000-0001-5416-6231](https://orcid.org/0000-0001-5416-6231)

**Jetze J. Tepe** – Department of Chemistry and Pharmacology & Toxicology, Michigan State University, East Lansing, Michigan 48824, United States; [orcid.org/0000-0001-5467-5589](https://orcid.org/0000-0001-5467-5589)

**Faqing Huang** – Department of Chemistry and Biochemistry, University of Southern Mississippi, Hattiesburg, Mississippi 39406, United States

Complete contact information is available at: <https://pubs.acs.org/10.1021/acs.jmedchem.1c00409>

### Notes

The authors declare no competing financial interest.

### Biographies

**Kaifu Gao** obtained his Ph.D. degree in physical chemistry from Chinese Academy of Sciences and completed his postdoctoral studies at the University of California, San Diego, under the guidance of Prof. Michael Gilson. His Ph.D. and postdoctoral studies focused on MD simulations of protein conformational transitions and binding free energy calculations. Now, he is a research associate in Prof. Guo-Wei Wei's group at Michigan State University. His current research concerns the application of deep learning to biological science and drug discovery, especially, automated drug-like compound generation and drug property prediction. His deep learning models have already been applied to the design and screening of SARS-CoV-2  $M^{P_{70}}$  inhibitors.

**Rui Wang** received her B.S. degree in mathematics at Xian Jiaotong University in 2017. Later, she joined Dr. Guo-Wei Wei's group at Michigan State University (MSU). Currently, she is a fifth-year Ph.D. candidate in the Department of Mathematics at MSU, and she expects to finish her Ph.D. study in July 2022. Her methodological research focuses on the development of mathematical tools for the descriptive and predictive modeling of biomolecules. She has also worked on genomics analysis and mathematical modeling of infectious diseases. She is highly interested in integrating AI, mathematics, genomics, biophysics, bioinformatics, and experimental data to tackle challenges in biological sciences, human diseases, and infectious pathogens.

**Jiahui Chen** received his Ph.D. degree from Southern Methodist University, where his research focused on the implementation of mathematical methods for biophysics, including the Poisson–Boltzmann equation. After graduation, he joined the Department of Mathematics at Michigan State University as a research associate in Professor Guo-Wei Wei's group. His current research focuses on topological and geometrical data analysis and machine learning algorithms with their modeling and application to biomolecules. His model studies were applied to prediction of mutation-induced binding free energy changes of the SARS-CoV-2 spike protein binding to ACE2 and antibodies.

**Jetze J. Tepe** is a Professor at the Department of Chemistry and Pharmacology & Toxicology at Michigan State University. He received his Ph.D. in chemistry from the University of Virginia (T.L. Macdonald) and completed his postdoctoral studies at Colorado State University (R. M. Williams). Research in his lab is focused on the synthesis of marine sponge metabolites and their unnatural drug-like analogs as antagonists or agonists of proteasome function. By development of new synthetic methodologies, drug-like derivatives of natural products are prepared and interrogated for their clinical significance in vitro, in cell culture, and in animal models, with a therapeutic focus on oncology and neurodegenerative diseases.

**Faqing Huang** received his Ph.D. degree in 1994 from Duke University, where he investigated the incorporation of boron into nucleic acids under the direction of Dr. Barbara Ramsay Shaw. As an NIH postdoctoral fellow under the mentorship of Dr. Michael Yarus at the University of Colorado at Boulder, he focused on the isolation of novel ribozymes that may shed light on the origin of life. He joined the faculty of the Department of Chemistry and Biochemistry at the University of Southern Mississippi in 1998. His interdisciplinary research interests include the origin and early evolution of life, RNA catalysis, chemical biology, targeted cancer therapeutics, antiviral strategies, innate immunity, novel cloning strategies, and self-amplifying mRNA based vaccines.

**Guo-Wei Wei** earned his Ph.D. degree from the University of British Columbia in 1996. He was awarded a fellowship from the NSERC of Canada to pursue his postdoctoral work at the University of Houston. In 1998, he joined the faculty of the National University of Singapore and was promoted to Associate Professor in 2001. In 2002, he relocated to Michigan State University, where he is an MSU Foundation Professor of Mathematics, Electrical and Computer Engineering, and Biochemistry and Molecular Biology. His current research interests include mathematical biosciences, deep learning, drug discovery, and computational geometry, topology, and graphing. He has advised over 150 research students, postdoctoral associates, and visiting scientists. Dr. Wei has served extensively on a wide variety of national and international panels, committees, and journal editorships.

## ACKNOWLEDGMENTS

This work was supported in part by NIH grant GM126189, NSF Grants DMS-2052983, DMS-1761320, and IIS-1900473, NASA 80NSSC21M0023, Michigan Economic Development Corporation, George Mason University award PD45722, Bristol-Myers Squibb 65109, and Pfizer.

## ABBREVIATIONS

3CL<sup>pro</sup>, 3-chymotrypsin-like protease; ADMET, absorption, distribution, metabolism, excretion, and toxicity; AUC, area under the curve; COVID-19, Coronavirus Disease 2019; CRFK, Crandell–Rees feline kidney cells; CYP, cytochrome P450; FIP, feline infectious peritonitis; FRET, fluorescence resonance energy transfer; GISAID, global initiative on sharing all influenza data; hERG, human *ether-a-go-go*; HIV, human immunodeficiency virus; HMK, hydroxymethylketone; MERS-CoV, Middle East respiratory syndrome coronavirus; M<sup>pro</sup>, main protease; NI, no inhibition; NIH, National Institutes of Health; NSP, nonstructural protein; ORF, open-reading frame; PAINS, pan-assay interference compounds; PDB, protein data bank; PK, pharmacokinetics; PL<sup>pro</sup>, papain-like protease; RT-PCR, reverse transcription polymerase chain reaction; SAR, structure–activity relationship; SARS-CoV, severe acute respiratory syndrome coronavirus; SARS-CoV-2, severe acute respiratory syndrome coronavirus 2; SNP, single nucleotide polymorphism

## REFERENCES

- (1) Shin, M. D.; Shukla, S.; Chung, Y. H.; Beiss, V.; Chan, S. K.; Ortega-Rivera, O. A.; Wirth, D. M.; Chen, A.; Sack, M.; Pokorski, J. K.; Steinmetz, N. F. COVID-19 vaccine development and a potential nanomaterial path forward. *Nat. Nanotechnol.* **2020**, *15*, 646–655.
- (2) Zimmer, C.; Corum, J.; Wee, S.-L. Coronavirus Vaccine Tracker. <https://www.nytimes.com/interactive/2020/science/coronavirus-vaccine-tracker.html>, 2020.
- (3) Wang, R.; Chen, J.; Gao, K.; Wei, G.-W. Vaccine-escape and fast-growing mutations in the United Kingdom, the United States, Singapore, Spain, India, and other COVID-19-devastated countries. *Genomics* **2021**, *113*, 2158–2170.
- (4) Jo, S.; Kim, S.; Yoo, J.; Kim, M.-S.; Shin, D. H. A study of 3CLpro as promising targets against SARS-CoV and SARS-CoV-2. *Microorganisms* **2021**, *9*, 756.
- (5) Halford, B. Pfizer unveils its oral SARS-CoV-2 inhibitor. <https://cen.acs.org/acs-news/acs-meeting-news/Pfizer-unveils-oral-SARS-CoV/99/i13>, 2020.
- (6) Halford, B. Pfizer's novel COVID-19 antiviral heads to clinical trials. <https://cen.acs.org/pharmaceuticals/drug-discovery/Pfizers-novel-COVID-19-antiviral/98/web/2020/09>, 2020.
- (7) Lansdowne, L. E. Exploring the Drug Development Process. <https://www.technologynetworks.com/drug-discovery/articles/exploring-the-drug-development-process-331894>, 2020.
- (8) Lu, R.; Zhao, X.; Li, J.; Niu, P.; Yang, B.; Wu, H.; Wang, W.; Song, H.; Huang, B.; Zhu, N.; Bi, Y.; Ma, X.; Zhan, F.; Wang, L.; Hu, T.; Zhou, H.; Hu, Z.; Zhou, W.; Zhao, L.; Chen, J.; Meng, Y.; Wang, J.; Lin, Y.; Yuan, J.; Xie, Z.; Ma, J.; Liu, W. J.; Wang, D.; Xu, W.; Holmes, E. C.; Gao, G. F.; Wu, G.; Chen, W.; Shi, W.; Tan, W. Genomic characterisation and epidemiology of 2019 novel coronavirus: implications for virus origins and receptor binding. *Lancet* **2020**, *395*, 565–574.
- (9) Walls, A. C.; Park, Y.-J.; Tortorici, M. A.; Wall, A.; McGuire, A. T.; Velesler, D. Structure, function, and antigenicity of the SARS-CoV-2 spike glycoprotein. *Cell* **2020**, *181*, 281–292.
- (10) Wrapp, D.; Wang, N.; Corbett, K. S.; Goldsmith, J. A.; Hsieh, C.-L.; Abiona, O.; Graham, B. S.; McLellan, J. S. Cryo-EM structure of the 2019-nCoV spike in the prefusion conformation. *Science* **2020**, *367*, 1260–1263.
- (11) Gao, K.; Wang, R.; Chen, J.; Cheng, L.; Frishcosy, J.; Huzumi, Y.; Qiu, Y.; Schluckbier, T.; Wei, G.-W. Methodology-centered review of molecular modeling, simulation, and prediction of SARS-CoV-2. *arXiv preprint*, arXiv:2102.00971, 2021, <https://arxiv.org/abs/2102.00971>.
- (12) Ghosh, A. K.; Brindisi, M.; Shahabi, D.; Chapman, M. E.; Mesecar, A. D. Drug development and medicinal chemistry efforts toward SARS-coronavirus and Covid-19 therapeutics. *ChemMedChem* **2020**, *15*, 907–932.
- (13) Cannalire, R.; Cerchia, C.; Beccari, A. R.; Di Leva, F. S.; Summa, V. Targeting SARS-CoV-2 proteases and polymerase for COVID-19 treatment: state of the art and future opportunities. *J. Med. Chem.* **2020**, DOI: 10.1021/acs.jmedchem.0c01140.
- (14) Ullrich, S.; Nitsche, C. The SARS-CoV-2 main protease as drug target. *Bioorg. Med. Chem. Lett.* **2020**, *30*, 127377.
- (15) Paul, A.; Sarkar, A.; Saha, S.; Maji, A.; Janah, P.; Kumar Maity, T. Synthetic and computational efforts towards the development of peptidomimetics and small-molecule SARS-CoV 3CLpro inhibitors: a review. *Bioorg. Med. Chem.* **2021**, *46*, 116301.
- (16) Amin, S. A.; Banerjee, S.; Gayen, S.; Jha, T. Protease targeted COVID-19 drug discovery: What we have learned from the past SARS-CoV inhibitors? *Eur. J. Med. Chem.* **2021**, *215*, 113294.
- (17) Pillaiyar, T.; Manickam, M.; Namasivayam, V.; Hayashi, Y.; Jung, S.-H. An overview of severe acute respiratory syndrome-coronavirus (SARS-CoV) 3CL protease inhibitors: peptidomimetics and small molecule chemotherapy. *J. Med. Chem.* **2016**, *59*, 6595–6628.
- (18) Kumar, V.; Jung, Y.-S.; Liang, P.-H. Anti-SARS coronavirus agents: a patent review (2008–present). *Expert Opin. Ther. Pat.* **2013**, *23*, 1337–1348.
- (19) Wang, H.-M.; Liang, P.-H. Pharmacophores and biological activities of severe acute respiratory syndrome viral protease inhibitors. *Expert Opin. Ther. Pat.* **2007**, *17*, 533–546.
- (20) Liang, P.-H. Characterization and inhibition of SARS-coronavirus main protease. *Curr. Top. Med. Chem.* **2006**, *6*, 361–376.
- (21) Wu, F.; Zhao, S.; Yu, B.; Chen, Y.-M.; Wang, W.; Song, Z.-G.; Hu, Y.; Tao, Z.-W.; Tian, J.-H.; Pei, Y.-Y.; Yuan, M.-L.; Zhang, Y.-L.; Dai, F.-H.; Liu, Y.; Wang, Q.-M.; Zheng, J.-J.; Xu, L.; Holmes, E. C.; Zhang, Y.-Z. A new coronavirus associated with human respiratory disease in China. *Nature* **2020**, *579*, 265–269.
- (22) Marra, M. A.; Jones, S. J. M.; Astell, C. R.; Holt, R. A.; Brooks-Wilson, A.; Butterfield, Y. S. N.; Khattra, J.; Asano, J. K.; Barber, S. A.; Chan, S. Y.; Cloutier, A.; Coughlin, S. M.; Freeman, D.; Girn, N.; Griffith, O. L.; Leach, S. R.; Mayo, M.; Mc-Donald, H.; Montgomery, S. B.; Pandoh, P. K.; Petrescu, A. S.; Robertson, A. G.; Schein, J. E.; Siddiqui, A.; Smailus, D. E.; Stott, J. M.; Yang, G. S.; Plummer, F.; Andonov, A.; Artsob, H.; Bastien, N.; Bernard, K.; Booth, T. F.; Bowness, D.; Czub, M.; Drebot, M.; Fernando, L.; Flick, R.; Garbutt, M.; Gray, M.; Grolla, A.; Jones, S.; Feldmann, H.; Meyers, A.; Kabani, A.; Li, Y.; Normand, S.; Stroher, U.; Tipples, G. A.; Tyler, S.; Vogrig, R.; Ward, D.; Watson, B.; Brunham, R. C.; Krajden, M.; Petric, M.; Skowronski, D. M.; Upton, C.; Roper, R. L. The genome sequence of the SARS-associated coronavirus. *Science* **2003**, *300*, 1399–1404.
- (23) Forni, D.; Cagliani, R.; Clerici, M.; Sironi, M. Molecular evolution of human coronavirus genomes. *Trends Microbiol.* **2017**, *25*, 35–48.
- (24) Chen, S.; Chen, L.; Tan, J.; Chen, J.; Du, L.; Sun, T.; Shen, J.; Chen, K.; Jiang, H.; Shen, X. Severe acute respiratory syndrome coronavirus 3C-like proteinase N terminus is indispensable for proteolytic activity but not for enzyme dimerization: biochemical and thermodynamic investigation in conjunction with molecular dynamics simulations. *J. Biol. Chem.* **2005**, *280*, 164–173.
- (25) Lee, J.; Worrall, L. J.; Vuckovic, M.; Rosell, F. I.; Gentile, F.; Ton, A.-T.; Caveney, N. A.; Ban, F.; Cherkasov, A.; Paetzel, M.; Strynadka, N. C. J. Crystallographic structure of wild-type SARS-CoV-2 main protease acyl-enzyme intermediate with physiological C-terminal autoprocessing site. *Nat. Commun.* **2020**, *11*, 5877.
- (26) Hoffman, R. L.; Kania, R. S.; Brothers, M. A.; Davies, J. F.; Ferre, R. A.; Gajiwala, K. S.; He, M.; Hogan, R. J.; Kozminski, K.; Li, L. Y.; Lockner, J. W.; Lou, J.; Marra, M. T.; Mitchell, L. J.; Murray, B. W.; Nieman, J. A.; Noell, S.; Planken, S. P.; Rowe, T.; Ryan, K.; Smith, G. J.

- Solowiej, J. E.; Stepan, C. M.; Taggart, B. Discovery of ketone-based covalent inhibitors of coronavirus 3CL proteases for the potential therapeutic treatment of COVID-19. *J. Med. Chem.* **2020**, *63*, 12725–12747.
- (27) Anand, K.; Ziebuhr, J.; Wadhwani, P.; Mesters, J. R.; Hilgenfeld, R. Coronavirus main proteinase (3CLpro) structure: basis for design of anti-SARS drugs. *Science* **2003**, *300*, 1763–1767.
- (28) Matthews, D. A.; Dragovich, P. S.; Webber, S. E.; Fuhrman, S. A.; Patick, A. K.; Zalman, L. S.; Hendrickson, T. F.; Love, R. A.; Prins, T. J.; Marakovits, J. T.; Zhou, R.; Tikhe, J.; Ford, C. E.; Meador, J. W.; Ferre, R. A.; Brown, E. L.; Binford, S. L.; Brothers, M. A.; DeLisle, D. M.; Worland, S. T. Structure-assisted design of mechanism-based irreversible inhibitors of human rhinovirus 3C protease with potent antiviral activity against multiple rhinovirus serotypes. *Proc. Natl. Acad. Sci. U. S. A.* **1999**, *96*, 11000–11007.
- (29) Yang, H.; Xie, W.; Xue, X.; Yang, K.; Ma, J.; Liang, W.; Zhao, Q.; Zhou, Z.; Pei, D.; Ziebuhr, J.; Hilgenfeld, R.; Yuen, K. Y.; Wong, L.; Gao, G.; Chen, S.; Chen, Z.; Ma, D.; Bartlam, M.; Rao, Z. Design of wide-spectrum inhibitors targeting coronavirus main proteases. *PLoS Biol.* **2005**, *3*, e324.
- (30) Nguyen, D. D.; Gao, K.; Chen, J.; Wang, R.; Wei, G.-W. Unveiling the molecular mechanism of SARS-CoV-2 main protease inhibition from 137 crystal structures using algebraic topology and deep learning. *Chem. Sci.* **2020**, *11*, 12036–12046.
- (31) Gao, K.; Nguyen, D. D.; Chen, J.; Wang, R.; Wei, G.-W. Repositioning of 8565 existing drugs for COVID-19. *J. Phys. Chem. Lett.* **2020**, *11*, 5373–5382.
- (32) Gao, K.; Nguyen, D. D.; Wang, R.; Wei, G.-W. Machine intelligence design of 2019-nCoV drugs. *bioRxiv* **2020**, DOI: 10.1101/2020.01.30.927889.
- (33) Powers, J. C.; Asgian, J. L.; Ekici, Ö. D.; James, K. E. Irreversible inhibitors of serine, cysteine, and threonine proteases. *Chem. Rev.* **2002**, *102*, 4639–4750.
- (34) Zhang, L.; Lin, D.; Kusov, Y.; Nian, Y.; Ma, Q.; Wang, J.; von Brunn, A.; Leyssen, P.; Lanko, K.; Neyts, J.; de Wilde, A.; Snijder, E. J.; Liu, H.; Hilgenfeld, R.  $\alpha$ -Ketoamides as broad-spectrum inhibitors of coronavirus and enterovirus replication: structure-based design, synthesis, and activity assessment. *J. Med. Chem.* **2020**, *63*, 4562–4578.
- (35) Zhang, L.; Lin, D.; Sun, X.; Curth, U.; Drosten, C.; Sauerhering, L.; Becker, S.; Rox, K.; Hilgenfeld, R. Crystal structure of SARS-CoV-2 main protease provides a basis for design of improved  $\alpha$ -ketoamide inhibitors. *Science* **2020**, *368*, 409–412.
- (36) Zhu, L.; George, S.; Schmidt, M. F.; Al-Gharabli, S. I.; Rademann, J.; Hilgenfeld, R. Peptide aldehyde inhibitors challenge the substrate specificity of the SARS-coronavirus main protease. *Antiviral Res.* **2011**, *92*, 204–212.
- (37) Tan, J.; George, S.; Kusov, Y.; Perbandt, M.; Anemüller, S.; Mesters, J. R.; Norder, H.; Coutard, B.; Lacroix, C.; Leyssen, P.; Neyts, J.; Hilgenfeld, R. 3C protease of enterovirus 68: structure-based design of Michael acceptor inhibitors and their broad-spectrum antiviral effects against picornaviruses. *J. Virol.* **2013**, *87*, 4339–4351.
- (38) Konno, S.; Thanigaimalai, P.; Yamamoto, T.; Nakada, K.; Kakiuchi, R.; Takayama, K.; Yamazaki, Y.; Yakushiji, F.; Akaji, K.; Kiso, Y.; Kawasaki, Y.; Chen, S.-E.; Freire, E.; Hayashi, Y. Design and synthesis of new tripeptide-type SARS-CoV 3CL protease inhibitors containing an electrophilic arylketone moiety. *Bioorg. Med. Chem.* **2013**, *21*, 412–424.
- (39) Thanigaimalai, P.; Konno, S.; Yamamoto, T.; Koiwai, Y.; Taguchi, A.; Takayama, K.; Yakushiji, F.; Akaji, K.; Chen, S.-E.; Naser-Tavakolian, A.; Schön, A.; Freire, E.; Hayashi, Y. Development of potent dipeptide-type SARS-CoV 3CL protease inhibitors with novel P3 scaffolds: design, synthesis, biological evaluation, and docking studies. *Eur. J. Med. Chem.* **2013**, *68*, 372–384.
- (40) Thanigaimalai, P.; Konno, S.; Yamamoto, T.; Koiwai, Y.; Taguchi, A.; Takayama, K.; Yakushiji, F.; Akaji, K.; Kiso, Y.; Kawasaki, Y.; Chen, S.-E.; Naser-Tavakolian, A.; Schön, A.; Freire, E.; Hayashi, Y. Design, synthesis, and biological evaluation of novel dipeptide-type SARS-CoV 3CL protease inhibitors: Structure-activity relationship study. *J. Med. Chem.* **2013**, *65*, 436–447.
- (41) Konno, S.; Kobayashi, K.; Senda, M.; Funai, Y.; Seki, Y.; Tamai, I.; Schäkel, L.; Sakata, K.; Pillaiyer, T.; Taguchi, A.; Taniguchi, A.; Gütschow, M.; Müller, C. E.; Takeuchi, K.; Hirohama, M.; Kawaguchi, A.; Kojima, M.; Senda, T.; Shirasaka, Y.; Kamitani, W.; Hayashi, Y. 3CL Protease Inhibitors with an Electrophilic Arylketone Moiety as Anti-SARS-CoV-2 Agents. *J. Med. Chem.* **2021**, DOI: 10.1021/acs.jmedchem.1c00665.
- (42) Boras, B.; Jones, R. M.; Anson, B. J.; Arenson, D.; Aschenbrenner, L.; Bakowski, M. A.; Beutler, N.; Binder, J.; Chen, E.; Eng, H.; Hammond, H.; Hammond, J.; Haupt, R. E.; Hoffman, R.; Kadar, E. P.; Kania, R.; Kimoto, E.; Kirkpatrick, M. G.; Lanyon, L.; Lendy, E. K.; Lillis, J. R.; Logue, J.; Luthra, S. A.; Ma, C.; Mason, S. W.; McGrath, M. E.; Noell, S.; Obach, R. S.; O'Brien, M. N.; O'Connor, R.; Ogilvie, K.; Owen, D.; Pettersson, M.; Reese, M. R.; Rogers, T. F.; Rossulek, M. I.; Sathish, J. G.; Shirai, N.; Stepan, C.; Ticehurst, M.; Updyke, L. W.; Weston, S.; Zhu, Y.; Wang, J.; Chatterjee, A. K.; Mesecar, A. D.; Frieman, M. B.; Anderson, A. S.; Allerton, C. Discovery of a novel inhibitor of coronavirus 3CL protease as a clinical candidate for the potential treatment of COVID-19. *BioRxiv* **2021**, DOI: 10.1101/2020.09.12.293498.
- (43) Owen, D. R.; Allerton, C. M. N.; Anderson, A. S.; Aschenbrenner, L.; Avery, M.; Berritt, S.; Boras, B.; Cardin, R. D.; Carlo, A.; Coffman, K. J.; Dantonio, A.; Di, L.; Eng, H.; Ferre, R.; Gajiwala, K. S.; Gibson, S. A.; Greasley, S. E.; Hurst, B. L.; Kadar, E. P.; Kalgutkar, A. S.; Lee, J. C.; Lee, J.; Liu, W.; Mason, S. W.; Noell, S.; Novak, J. J.; Obach, R. S.; Ogilvie, K.; Patel, N. C.; Pettersson, M.; Rai, D. K.; Reese, M. R.; Sammons, M. F.; Sathish, J. G.; Singh, R. S. P.; Stepan, C. M.; Stewart, A. E.; Tuttle, J. B.; Updyke, L.; Verhoest, P. R.; Wei, L.; Yang, Q.; Zhu, Y. An Oral SARS-CoV-2 Mpro Inhibitor Clinical Candidate for the Treatment of COVID-19. *medRxiv* **2021**, DOI: 10.1101/2021.07.28.21261232.
- (44) Beer, T. Pfizer CEO Says Antiviral Pill To Treat Covid Could Be Ready By The End Of The Year. <https://www.forbes.com/sites/tommybeer/2021/04/27/pfizer-ceo-says-antiviral-pill-to-treat-covid-could-be-ready-by-end-of-the-year/?sh/244a1e012a0d>, 2021.
- (45) Qiao, J.; Li, Y.-S.; Zeng, R.; Liu, F.-L.; Luo, R.-H.; Huang, C.; Wang, Y.-F.; Zhang, J.; Quan, B.; Shen, C.; Mao, X.; Liu, X.; Sun, W.; Yang, W.; Ni, X.; Wang, K.; Xu, L.; Duan, Z.-L.; Zou, Q.-C.; Zhang, H.-L.; Qu, W.; Long, Y.-H.-P.; Li, M.-H.; Yang, R.-C.; Liu, X.; You, J.; Zhou, Y.; Yao, R.; Li, W.-P.; Liu, J.-M.; Chen, P.; Liu, Y.; Lin, G.-F.; Yang, X.; Zou, J.; Li, L.; Hu, Y.; Lu, G.-W.; Li, W.-M.; Wei, Y.-Q.; Zheng, Y.-T.; Lei, J.; Yang, S. SARS-CoV-2 Mpro inhibitors with antiviral activity in a transgenic mouse model. *Science* **2021**, *371*, 1374–1378.
- (46) Ganguly, H. K.; Basu, G. Conformational landscape of substituted prolines. *Biophys. Rev.* **2020**, *12*, 25–39.
- (47) Raboisson, P.; Rognan, D.; Aldous, D.; Wermuth, C. G. *The Practice of Medicinal Chemistry*; Elsevier, 2015.
- (48) Dai, W.; Zhang, B.; Jiang, X.-M.; Su, H.; Li, J.; Zhao, Y.; Xie, X.; Jin, Z.; Peng, J.; Liu, F.; Li, C.; Li, Y.; Bai, F.; Wang, H.; Cheng, X.; Cen, X.; Hu, S.; Yang, X.; Wang, J.; Liu, X.; Xiao, G.; Jiang, H.; Rao, Z.; Zhang, L.-K.; Xu, Y.; Yang, H.; Liu, H. Structure-based design of antiviral drug candidates targeting the SARS-CoV-2 main protease. *Science* **2020**, *368*, 1331–1335.
- (49) Rathnayake, A. D.; Zheng, J.; Kim, Y.; Perera, K. D.; Mackin, S.; Meyerholz, D. K.; Kashipathy, M. M.; Battaile, K. P.; Lovell, S.; Perlman, S.; Groutas, W. C.; Chang, K.-O. 3C-like protease inhibitors block coronavirus replication in vitro and improve survival in MERS-CoV-infected mice. *Sci. Transl. Med.* **2020**, *12*, eabc5332.
- (50) Vuong, W.; Khan, M. B.; Fischer, C.; Arutyunova, E.; Lamer, T.; Shields, J.; Saffran, H. A.; McKay, R. T.; van Belkum, M. J.; Joyce, M. A.; Young, H. S.; Tyrrell, D. L.; Vederas, J. C.; Lemieux, M. J. Feline coronavirus drug inhibits the main protease of SARS-CoV-2 and blocks virus replication. *Nat. Commun.* **2020**, *11*, 5409.
- (51) Kumar, V.; Shin, J. S.; Shie, J.-J.; Ku, K. B.; Kim, C.; Go, Y. Y.; Huang, K.-F.; Kim, M.; Liang, P.-H. Identification and evaluation of potent Middle East respiratory syndrome coronavirus (MERS-CoV) 3CLPro inhibitors. *Antiviral Res.* **2017**, *141*, 101–106.

- (52) Wang, H.; He, S.; Deng, W.; Zhang, Y.; Li, G.; Sun, J.; Zhao, W.; Guo, Y.; Yin, Z.; Li, D.; Shang, L. Comprehensive insights into the catalytic mechanism of middle east respiratory syndrome 3C-Like protease and severe acute respiratory syndrome 3C-Like protease. *ACS Catal.* **2020**, *10*, 5871–5890.
- (53) Yang, S.; Chen, S.-J.; Hsu, M.-F.; Wu, J.-D.; Tseng, C.-T. K.; Liu, Y.-F.; Chen, H.-C.; Kuo, C.-W.; Wu, C.-S.; Chang, L.-W.; Chen, W.-C.; Liao, S.-Y.; Chang, T.-Y.; Hung, H.-H.; Shr, H.-L.; Liu, C.-Y.; Huang, Y.-A.; Chang, L.-Y.; Hsu, J.-C.; Peters, C. J.; Wang, A. H.-J.; Hsu, M.-C. Synthesis, crystal structure, structure-activity relationships, and antiviral activity of a potent SARS coronavirus 3CL protease inhibitor. *J. Med. Chem.* **2006**, *49*, 4971–4980.
- (54) Sharun, K.; Tiwari, R.; Dhama, K. Protease inhibitor GC376 for COVID-19: Lessons learned from feline infectious peritonitis. *Ann. Med.* **2021**, *61*, 122–125.
- (55) Ma, C.; Sacco, M. D.; Hurst, B.; Townsend, J. A.; Hu, Y.; Szeto, T.; Zhang, X.; Tarbet, B.; Marty, M. T.; Chen, Y.; Wang, J. Boceprevir, GC-376, and calpain inhibitors II, XII inhibit SARS-CoV-2 viral replication by targeting the viral main protease. *Cell Res.* **2020**, *30*, 678–692.
- (56) Pedersen, N. C.; Kim, Y.; Liu, H.; Galasiti Kankanamalage, A. C.; Eckstrand, C.; Groutas, W. C.; Bannasch, M.; Meadows, J. M.; Chang, K.-O. Efficacy of a 3C-like protease inhibitor in treating various forms of acquired feline infectious peritonitis. *J. Feline Med. Surg.* **2018**, *20*, 378–392.
- (57) Kim, Y.; Liu, H.; Galasiti Kankanamalage, A. C.; Weerasekera, S.; Hua, D. H.; Groutas, W. C.; Chang, K.-O.; Pedersen, N. C. Reversal of the progression of fatal coronavirus infection in cats by a broad-spectrum coronavirus protease inhibitor. *PLoS Pathog.* **2016**, *12*, e1005531.
- (58) Kim, Y.; Lovell, S.; Tiew, K.-C.; Mandadapu, S. R.; Alliston, K. R.; Battaile, K. P.; Groutas, W. C.; Chang, K.-O. Broad-spectrum antivirals against 3C or 3C-like proteases of picornaviruses, noroviruses, and coronaviruses. *J. Virol.* **2012**, *86*, 11754–11762.
- (59) Cat got your SARS-CoV-2 antiviral? <https://www.genengnews.com/news/cat-got-your-sars-cov-2-antiviral/>, 2020.
- (60) Dampalla, C. S.; Zheng, J.; Perera, K. D.; Wong, L.-Y. R.; Meyerholz, D. K.; Nguyen, H. N.; Kashipathy, M. M.; Battaile, K. P.; Lovell, S.; Kim, Y.; Perlman, S.; Groutas, W. C.; Chang, K.-O. Postinfection treatment with a protease inhibitor increases survival of mice with a fatal SARS-CoV-2 infection. *Proc. Natl. Acad. Sci. U. S. A.* **2021**, *118*, e2101555118.
- (61) Ahmed Laskar, A.; Younus, H. Aldehyde toxicity and metabolism: the role of aldehyde dehydrogenases in detoxification, drug resistance and carcinogenesis. *Drug Metab. Rev.* **2019**, *51*, 42–64.
- (62) Uchida, K. Role of reactive aldehyde in cardiovascular diseases. *Free Radical Biol. Med.* **2000**, *28*, 1685–1696.
- (63) Steuten, K.; Kim, H.; Widen, J. C.; Babin, B. M.; Onguka, O.; Lovell, S.; Bolgi, O.; Cerikan, B.; Neufeldt, C. J.; Cortese, M.; Muir, R. K.; Bennett, J. M.; Geiss-Friedlander, R.; Peters, C.; Bartenschlager, R.; Bogyo, M. Challenges for targeting SARS-CoV-2 proteases as a therapeutic strategy for COVID-19. *ACS Infect. Dis.* **2021**, *7*, 1457–1468.
- (64) Lee, C.-C.; Kuo, C.-J.; Ko, T.-P.; Hsu, M.-F.; Tsui, Y.-C.; Chang, S.-C.; Yang, S.; Chen, S.-J.; Chen, H.-C.; Hsu, M.-C.; Shih, S.-R.; Liang, P.-H.; Wang, A. H.-J. Structural basis of inhibition specificities of 3C and 3C-like proteases by zinc-coordinating and peptidomimetic compounds. *J. Biol. Chem.* **2009**, *284*, 7646–7655.
- (65) Iketani, S.; Forouhar, F.; Liu, H.; Hong, S. J.; Lin, F.-Y.; Nair, M. S.; Zask, A.; Huang, Y.; Xing, L.; Stockwell, B. R.; Chavez, A.; Ho, D. D. Lead compounds for the development of SARS-CoV-2 3CL protease inhibitors. *Nat. Commun.* **2021**, *12*, 2016.
- (66) Shie, J.-J.; Fang, J.-M.; Kuo, T.-H.; Kuo, C.-J.; Liang, P.-H.; Huang, H.-J.; Wu, Y.-T.; Jan, J.-T.; Cheng, Y.-S. E.; Wong, C.-H. Inhibition of the severe acute respiratory syndrome 3CL protease by peptidomimetic  $\alpha$ ,  $\beta$ -unsaturated esters. *Bioorg. Med. Chem.* **2005**, *13*, 5240–5252.
- (67) Ryu, Y. B.; Park, S.-J.; Kim, Y. M.; Lee, J.-Y.; Seo, W. D.; Chang, J. S.; Park, K. H.; Rho, M.-C.; Lee, W. S. SARS-CoV 3CLpro inhibitory effects of quinone-methide triterpenes from *Tripterygium regelii*. *Bioorg. Med. Chem. Lett.* **2010**, *20*, 1873–1876.
- (68) Sreeramulu, S.; Gande, S. L.; Göbel, M.; Schwalbe, H. Molecular mechanism of inhibition of the human protein complex Hsp90-Cdc37, a kinome chaperone-cochaperone, by triterpene celastrol. *Angew. Chem., Int. Ed.* **2009**, *48*, 5853–5855.
- (69) Jackson, P. A.; Widen, J. C.; Harki, D. A.; Brummond, K. M. Covalent modifiers: A chemical perspective on the reactivity of  $\alpha$ ,  $\beta$ -unsaturated carbonyls with thiols via hetero-Michael addition reactions. *J. Med. Chem.* **2017**, *60*, 839–885.
- (70) Shang, J.; Wan, Y.; Luo, C.; Ye, G.; Geng, Q.; Auerbach, A.; Li, F. Cell entry mechanisms of SARS-CoV-2. *Proc. Natl. Acad. Sci. U. S. A.* **2020**, *117*, 11727–11734.
- (71) Liu, T.; Luo, S.; Libby, P.; Shi, G.-P. Cathepsin L-selective inhibitors: A potentially promising treatment for COVID-19 patients. *Pharmacol. Ther.* **2020**, *213*, 107587.
- (72) Ou, X.; Liu, Y.; Lei, X.; Li, P.; Mi, D.; Ren, L.; Guo, L.; Guo, R.; Chen, T.; Hu, J.; Xiang, Z.; Mu, Z.; Chen, X.; Chen, J.; Hu, K.; Jin, Q.; Wang, J.; Qian, Z. Characterization of spike glycoprotein of SARS-CoV-2 on virus entry and its immune cross-reactivity with SARS-CoV. *Nat. Commun.* **2020**, *11*, 1620.
- (73) Sacco, M. D.; Ma, C.; Lagarias, P.; Gao, A.; Townsend, J. A.; Meng, X.; Dube, P.; Zhang, X.; Hu, Y.; Kitamura, N.; Hurst, B.; Tarbet, B.; Marty, M. T.; Kolocouris, A.; Xiang, Y.; Chen, Y.; Wang, J. Structure and inhibition of the SARS-CoV-2 main protease reveal strategy for developing dual inhibitors against Mpro and cathepsin L. *Sci. Adv.* **2020**, *6*, eabe0751.
- (74) Ghosh, A. K.; Gong, G.; Grum-Tokars, V.; Mulhearn, D. C.; Baker, S. C.; Coughlin, M.; Prabhakar, B. S.; Sleeman, K.; Johnson, M. E.; Mesecar, A. D. Design, synthesis and antiviral efficacy of a series of potent chloropyridyl ester-derived SARS-CoV 3CLpro inhibitors. *Bioorg. Med. Chem. Lett.* **2008**, *18*, 5684–5688.
- (75) Wu, C.-Y.; King, K.-Y.; Kuo, C.-J.; Fang, J.-M.; Wu, Y.-T.; Ho, M.-Y.; Liao, C.-L.; Shie, J.-J.; Liang, P.-H.; Wong, C.-H. Stable benzotriazole esters as mechanism-based inactivators of the severe acute respiratory syndrome 3CL protease. *Chem. Biol.* **2006**, *13*, 261–268.
- (76) Zhang, J.; Pettersson, H. I.; Huitema, C.; Niu, C.; Yin, J.; James, M. N.; Eltis, L. D.; Vederas, J. C. Design, synthesis, and evaluation of inhibitors for severe acute respiratory syndrome 3C-like protease based on phthalhydrazide ketones or heteroaromatic esters. *J. Med. Chem.* **2007**, *50*, 1850–1864.
- (77) Niu, C.; Yin, J.; Zhang, J.; Vederas, J. C.; James, M. N. Molecular docking identifies the binding of 3-chloropyridine moieties specifically to the S1 pocket of SARS-CoV Mpro. *Bioorg. Med. Chem.* **2008**, *16*, 293–302.
- (78) Wu, C.-Y.; Jan, J.-T.; Ma, S.-H.; Kuo, C.-J.; Juan, H.-F.; Cheng, Y.-S. E.; Hsu, H.-H.; Huang, H.-C.; Wu, D.; Brik, A.; Liang, F.-S.; Liu, R.-S.; Fang, J.-M.; Chen, S.-T.; Liang, P.-H.; Wong, C.-H. Small molecules targeting severe acute respiratory syndrome human coronavirus. *Proc. Natl. Acad. Sci. U. S. A.* **2004**, *101*, 10012–10017.
- (79) Blanchard, J. E.; Elowe, N. H.; Huitema, C.; Fortin, P. D.; Cechetto, J. D.; Eltis, L. D.; Brown, E. D. High-throughput screening identifies inhibitors of the SARS coronavirus main proteinase. *Chem. Biol.* **2004**, *11*, 1445–1453.
- (80) Sun, L.-Y.; Chen, C.; Su, J.; Li, J.-Q.; Jiang, Z.; Gao, H.; Chigan, J.-Z.; Ding, H.-H.; Zhai, L.; Yang, K.-W. Ebsulfur and Ebselen as highly potent scaffolds for the development of potential SARS-CoV-2 antivirals. *Bioorg. Chem.* **2021**, *112*, 104889.
- (81) Jin, Z.; Du, X.; Xu, Y.; Deng, Y.; Liu, M.; Zhao, Y.; Zhang, B.; Li, X.; Zhang, L.; Peng, C.; Duan, Y.; Yu, J.; Wang, L.; Yang, K.; Liu, F.; Jiang, R.; Yang, X.; You, T.; Liu, X.; Yang, X.; Bai, F.; Liu, H.; Liu, X.; Guddat, L. W.; Xu, W.; Xiao, G.; Qin, C.; Shi, Z.; Jiang, H.; Rao, Z.; Yang, H. Structure of M pro from SARS-CoV-2 and discovery of its inhibitors. *Nature* **2020**, *582*, 289–293.
- (82) Ma, C.; Hu, Y.; Townsend, J. A.; Lagarias, P. I.; Marty, M. T.; Kolocouris, A.; Wang, J. Ebselen, Disulfiram, Carmofur, PX-12, Tideglusib, and Shikonin are nonspecific promiscuous SARS-CoV-2

- main protease inhibitors. *ACS Pharmacol. Transl. Sci.* **2020**, *3*, 1265–1277.
- (83) Renson, M.; Etschenberg, E.; Winkelmann, J. 2-Phenyl-1, 2-benzoselenazol-3 (2H)-one containing pharmaceutical preparations and process for the treatment of rheumatic diseases. US Patent 4,352,799, 1982.
- (84) Haritha, C.; Sharun, K.; Jose, B. Ebselen, a new candidate therapeutic against SARS-CoV-2. *International Journal of Surgery (London, England)* **2020**, *84*, 53.
- (85) Baell, J.; Walters, M. A. Chemistry: Chemical con artists foil drug discovery. *Nature* **2014**, *513*, 481.
- (86) Bacha, U.; Barrila, J.; Velazquez-Campoy, A.; Leavitt, S. A.; Freire, E. Identification of novel inhibitors of the SARS coronavirus main protease 3CLpro. *Biochemistry* **2004**, *43*, 4906–4912.
- (87) Liu, P.; Liu, H.; Sun, Q.; Liang, H.; Li, C.; Deng, X.; Liu, Y.; Lai, L. Potent inhibitors of SARS-CoV-2 3C-like protease derived from N-substituted isatin compounds. *European. Eur. J. Med. Chem.* **2020**, *206*, 112702.
- (88) Zhou, L.; Liu, Y.; Zhang, W.; Wei, P.; Huang, C.; Pei, J.; Yuan, Y.; Lai, L. Isatin compounds as noncovalent SARS coronavirus 3C-like protease inhibitors. *J. Med. Chem.* **2006**, *49*, 3440–3443.
- (89) Chen, L.-R.; Wang, Y.-C.; Lin, Y. W.; Chou, S.-Y.; Chen, S.-F.; Liu, L. T.; Wu, Y.-T.; Kuo, C.-J.; Chen, T. S.-S.; Juang, S.-H. Synthesis and evaluation of isatin derivatives as effective SARS coronavirus 3CL protease inhibitors. *Bioorg. Med. Chem. Lett.* **2005**, *15*, 3058–3062.
- (90) Turlington, M.; Chun, A.; Tomar, S.; Eggler, A.; Grum-Tokars, V.; Jacobs, J.; Daniels, J. S.; Dawson, E.; Saldanha, A.; Chase, P.; Baez-Santos, Y. M.; Lindsley, C. W.; Hodder, P.; Mesecar, A. D.; Stauffer, S. R. Discovery of N-(benzo [1, 2, 3] triazol-1-yl)-N-(benzyl) acetamido phenyl) carboxamides as severe acute respiratory syndrome coronavirus (SARS-CoV) 3CLpro inhibitors: identification of ML300 and noncovalent nanomolar inhibitors with an induced-fit binding. *Bioorg. Med. Chem. Lett.* **2013**, *23*, 6172–6177.
- (91) Shie, J.-J.; Fang, J.-M.; Kuo, C.-J.; Kuo, T.-H.; Liang, P.-H.; Huang, H.-J.; Yang, W.-B.; Lin, C.-H.; Chen, J.-L.; Wu, Y.-T.; Wong, C.-H. Discovery of potent antide inhibitors against the severe acute respiratory syndrome 3CL protease. *J. Med. Chem.* **2005**, *48*, 4469–4473.
- (92) Akaji, K.; Konno, H.; Mitsui, H.; Teruya, K.; Shimamoto, Y.; Hattori, Y.; Ozaki, T.; Kusunoki, M.; Sanjoh, A. Structure-based design, synthesis, and evaluation of peptide-mimetic SARS 3CL protease inhibitors. *J. Med. Chem.* **2011**, *54*, 7962–7973.
- (93) Shao, Y.-M.; Yang, W.-B.; Peng, H.-P.; Hsu, M.-F.; Tsai, K.-C.; Kuo, T.-H.; Wang, A. H.-J.; Liang, P.-H.; Lin, C.-H.; Yang, A.-S.; Wong, C.-H. Structure-based design and synthesis of highly potent SARS-CoV 3CL protease inhibitors. *ChemBioChem* **2007**, *8*, 1654–1657.
- (94) Coelho, C.; Gallo, G.; Campos, C. B.; Hardy, L.; Würtele, M. Biochemical screening for SARS-CoV-2 main protease inhibitors. *PLoS One* **2020**, *15*, e0240079.
- (95) Clanton, D.; Moran, R.; McMahon, J.; Weislow, O.; Buckheit, R., Jr; Hollingshead, M.; Ciminale, V.; Felber, B.; Pavlakis, G.; Bader, J. Sulfonic acid dyes: inhibition of the human immunodeficiency virus and mechanism of action. *J. Acquired Immune Defic. Syndr.* **1992**, *5*, 771–781.
- (96) Xiao, Y.; Liu, C.; Tang, W.; Zhang, H.; Chen, X. Evans blue inhibits hbv replication through a dual antiviral mechanism by targeting virus binding and capsid assembly. *Front. Microbiol.* **2019**, *10*, 2638.
- (97) Lu, L.-L.; Mahindroo, N.; Liang, P.-H.; Peng, Y.-H.; Kuo, C.-J.; Tsai, K.-C.; Hsieh, H.-P.; Chao, Y.-S.; Wu, S.-Y. Structure-based drug design and structural biology study of novel nonpeptide inhibitors of severe acute respiratory syndrome coronavirus main protease. *J. Med. Chem.* **2006**, *49*, 5154–5161.
- (98) Wang, L.; Bao, B.-B.; Song, G.-Q.; Chen, C.; Zhang, X.-M.; Lu, W.; Wang, Z.; Cai, Y.; Li, S.; Fu, S.; Song, F.-H.; Yang, H.; Wang, J.-G. Discovery of unsymmetrical aromatic disulfides as novel inhibitors of SARS-CoV main protease: chemical synthesis, biological evaluation, molecular docking and 3D-QSAR study. *Eur. J. Med. Chem.* **2017**, *137*, 450–461.
- (99) Zhang, D.; Fourie-O'Donohue, A.; Dragovich, P. S.; Pillow, T. H.; Sadowsky, J. D.; Kozak, K. R.; Cass, R. T.; Liu, L.; Deng, Y.; Liu, Y.; Hop, C. E.; Khojasteh, S. C. Catalytic cleavage of disulfide bonds in small molecules and linkers of Antibody–Drug conjugates. *Drug Metab. Dispos.* **2019**, *47*, 1156–1163.
- (100) Zhu, W.; Xu, M.; Chen, C. Z.; Guo, H.; Shen, M.; Hu, X.; Shinn, P.; Klumpp-Thomas, C.; Michael, S. G.; Zheng, W. Identification of SARS-CoV-2 3CL protease inhibitors by a quantitative high-throughput screening. *ACS Pharmacol. Transl. Sci.* **2020**, *3*, 1008–1016.
- (101) Jain, R. P.; Pettersson, H. L.; Zhang, J.; Aull, K. D.; Fortin, P. D.; Huitema, C.; Eltis, L. D.; Parrish, J. C.; James, M. N. G.; Wishart, D. S.; Vederas, J. C. Synthesis and evaluation of keto-glutamine analogues as potent inhibitors of severe acute respiratory syndrome 3CLpro. *J. Med. Chem.* **2004**, *47*, 6113–6116.
- (102) Su, H.-x.; Yao, S.; Zhao, W.-f.; Li, M.-j.; Liu, J.; Shang, W.-j.; Xie, H.; Ke, C.-q.; Hu, H.-c.; Gao, M.-n.; Yu, K.-q.; Liu, H.; Shen, J.-s.; Tang, W.; Zhang, L.-k.; Xiao, G.-f.; Ni, L.; Wang, D.-w.; Zuo, J.-p.; Jiang, H.-l.; Bai, F.; Wu, Y.; Ye, Y.; Xu, Y.-c. Anti-SARS-CoV-2 activities in vitro of Shuanghuanglian preparations and bioactive ingredients. *Acta Pharmacol. Sin.* **2020**, *41*, 1167–1177.
- (103) Zandi, K.; Musall, K.; Oo, A.; Cao, D.; Liang, B.; Hassandarvish, P.; Lan, S.; Slack, R. L.; Kirby, K. A.; Bassit, L.; Amblard, F.; Kim, B.; AbuBakar, S.; Sarafianos, S. G.; Schinazi, R. F. Baicalein and baicalin inhibit SARS-CoV-2 RNA-dependent-RNA polymerase. *Microorganisms* **2021**, *9*, 893.
- (104) Lee, C.-C.; Kuo, C.-J.; Hsu, M.-F.; Liang, P.-H.; Fang, J.-M.; Shie, J.-J.; Wang, A. H.-J. Structural basis of mercury- and zinc-conjugated complexes as SARS-CoV 3C-like protease inhibitors. *FEBS Lett.* **2007**, *581*, 5454–5458.
- (105) Hsu, J. T.-A.; Kuo, C.-J.; Hsieh, H.-P.; Wang, Y.-C.; Huang, K.-K.; Lin, C. P.-C.; Huang, P.-F.; Chen, X.; Liang, P.-H. Evaluation of metal-conjugated compounds as inhibitors of 3CL protease of SARS-CoV. *FEBS Lett.* **2004**, *574*, 116–120.
- (106) Bacha, U.; Barrila, J.; Gabelli, S. B.; Kiso, Y.; Mario Amzel, L.; Freire, E. Development of broad-spectrum halomethyl ketone inhibitors against coronavirus main protease 3CLpro. *Chem. Biol. Drug Des.* **2008**, *72*, 34–49.
- (107) Shao, Y.-M.; Yang, W.-B.; Kuo, T.-H.; Tsai, K.-C.; Lin, C.-H.; Yang, A.-S.; Liang, P.-H.; Wong, C.-H. Design, synthesis, and evaluation of trifluoromethyl ketones as inhibitors of SARS-CoV 3CL protease. *Bioorg. Med. Chem.* **2008**, *16*, 4652–4660.
- (108) Regnier, T.; Sarma, D.; Hidaka, K.; Bacha, U.; Freire, E.; Hayashi, Y.; Kiso, Y. New developments for the design, synthesis and biological evaluation of potent SARS-CoV 3CLpro inhibitors. *Bioorg. Med. Chem. Lett.* **2009**, *19*, 2722–2727.
- (109) Sydnese, M. O.; Hayashi, Y.; Sharma, V. K.; Hamada, T.; Bacha, U.; Barrila, J.; Freire, E.; Kiso, Y. Synthesis of glutamic acid and glutamine peptides possessing a trifluoromethyl ketone group as SARS-CoV 3CL protease inhibitors. *Tetrahedron* **2006**, *62*, 8601–8609.
- (110) Zhang, H.-Z.; Zhang, H.; Kemnitzer, W.; Tseng, B.; Cinatl, J., Jr; Michaelis, M.; Doerr, H. W.; Cai, S. X. Design and synthesis of dipeptidyl glutaminy fluoromethyl ketones as potent severe acute respiratory syndrome coronavirus (SARS-CoV) inhibitors. *J. Med. Chem.* **2006**, *49*, 1198–1201.
- (111) Lee, T.-W.; Cherney, M. M.; Huitema, C.; Liu, J.; James, K. E.; Powers, J. C.; Eltis, L. D.; James, M. N. Crystal structures of the main peptidase from the SARS coronavirus inhibited by a substrate-like azapeptide epoxide. *J. Mol. Biol.* **2005**, *353*, 1137–1151.
- (112) Chuck, C.-P.; Chen, C.; Ke, Z.; Wan, D. C.-C.; Chow, H.-F.; Wong, K.-B. Design, synthesis and crystallographic analysis of nitrile-based broad-spectrum peptidomimetic inhibitors for coronavirus 3C-like proteases. *Eur. J. Med. Chem.* **2013**, *59*, 1–6.
- (113) Fu, L.; Ye, F.; Feng, Y.; Yu, F.; Wang, Q.; Wu, Y.; Zhao, C.; Sun, H.; Huang, B.; Niu, P.; Song, H.; Shi, Y.; Li, X.; Tan, W.; Qi, J.; Gao, G. F. Both Boceprevir and GC376 efficaciously inhibit SARS-CoV-2 by targeting its main protease. *Nat. Commun.* **2020**, *11*, 4417.
- (114) Kaeppler, U.; Stiefl, N.; Schiller, M.; Vicik, R.; Breuning, A.; Schmitz, W.; Rupprecht, D.; Schmuck, C.; Baumann, K.; Ziebuhr, J.; Schirmweiser, T. A new lead for nonpeptidic active-site-directed



inhibitors of the severe acute respiratory syndrome coronavirus main protease discovered by a combination of screening and docking methods. *J. Med. Chem.* **2005**, *48*, 6832–6842.

(115) Ghosh, A. K.; Xi, K.; Grum-Tokars, V.; Xu, X.; Ratia, K.; Fu, W.; Houser, K. V.; Baker, S. C.; Johnson, M. E.; Mesecar, A. D. Structure-based design, synthesis, and biological evaluation of peptidomimetic SARS-CoV 3CLpro inhibitors. *Bioorg. Med. Chem. Lett.* **2007**, *17*, 5876–5880.

(116) Ghosh, A. K.; Xi, K.; Ratia, K.; Santarsiero, B. D.; Fu, W.; Harcourt, B. H.; Rota, P. A.; Baker, S. C.; Johnson, M. E.; Mesecar, A. D. Design and synthesis of peptidomimetic severe acute respiratory syndrome chymotrypsin-like protease inhibitors. *J. Med. Chem.* **2005**, *48*, 6767–6771.

(117) Breidenbach, J.; Lemke, C.; Pillaiyar, T.; Schäkel, L.; Al Hamwi, G.; Dieltz, M.; Gedtschold, R.; Geiger, N.; Lopez, V.; Mirza, S.; Namasivayam, V.; Schiedel, A. C.; Sylvester, K.; Thimm, D.; Vielmuth, C.; Phuong Vu, L.; Zylina, M.; Bodem, J.; Gütschow, M.; Müller, C. E. Targeting the main protease of SARS-CoV-2: from the establishment of high throughput screening to the design of tailored inhibitors. *Angew. Chem., Int. Ed.* **2021**, *60*, 10423–10429.

(118) Liu, W.; Zhu, H.-M.; Niu, G.-J.; Shi, E.-Z.; Chen, J.; Sun, B.; Chen, W.-Q.; Zhou, H.-G.; Yang, C. Synthesis, modification and docking studies of 5-sulfonyl isatin derivatives as SARS-CoV 3C-like protease inhibitors. *Bioorg. Med. Chem.* **2014**, *22*, 292–302.

(119) Jacobs, J.; Grum-Tokars, V.; Zhou, Y.; Turlington, M.; Saldanha, S. A.; Chase, P.; Egger, A.; Dawson, E. S.; Baez-Santos, Y. M.; Tomar, S.; Mielech, A. M.; Baker, S. C.; Lindsley, C. W.; Hodder, P.; Mesecar, A.; Stauffer, S. R. Discovery, synthesis, and structure-based optimization of a series of N-(tert-butyl)-2-(N-arylamido)-2-(pyridin-3-yl) acetamides (ML188) as potent noncovalent small molecule inhibitors of the severe acute respiratory syndrome coronavirus (SARS-CoV) 3CL protease. *J. Med. Chem.* **2013**, *56*, 534–546.

(120) Lee, H.; Mittal, A.; Patel, K.; Gatz, J. L.; Truong, L.; Torres, J.; Mulhearn, D. C.; Johnson, M. E. Identification of novel drug scaffolds for inhibition of SARS-CoV 3-Chymotrypsin-like protease using virtual and high-throughput screenings. *Bioorg. Med. Chem.* **2014**, *22*, 167–177.

(121) Ahn, T.-Y.; Kuo, C.-J.; Liu, H.-G.; Ha, D.-C.; Liang, P.-H.; Jung, Y.-S. Synthesis and evaluation of benzoquinolinone derivatives as sars-cov 3cl protease inhibitors. *Bull. Korean Chem. Soc.* **2010**, *31*, 87–91.

(122) Chen, L.; Chen, S.; Gui, C.; Shen, J.; Shen, X.; Jiang, H. Discovering severe acute respiratory syndrome coronavirus 3CL protease inhibitors: virtual screening, surface plasmon resonance, and fluorescence resonance energy transfer assays. *J. Biomol. Screening* **2006**, *11*, 915–921.

(123) Ryu, Y. B.; Jeong, H. J.; Kim, J. H.; Kim, Y. M.; Park, J.-Y.; Kim, D.; Nguyen, T. T. H.; Park, S.-J.; Chang, J. S.; Park, K. H.; Rho, M.-C.; Lee, W. S. Biflavonoids from *Torreya nucifera* displaying SARS-CoV 3CLpro inhibition. *Bioorg. Med. Chem.* **2010**, *18*, 7940–7947.

(124) Li, Y.; Zhang, J.; Wang, N.; Zhang, Y.; Yang, Y.; Yuan, Y.; Jing, H.; Liu, X.; Wu, S.; Luo, P.; Zhang, W.; Lu, D.; Zeng, H.; Guo, G.; Zou, Q. High-throughput Screening and Experimental Identification of Potent Drugs Targeting SARS-CoV-2 Main Protease. *Research square* **2020**, DOI: 10.21203/rs.3.rs-40014/v1.

(125) Park, J.-Y.; Kim, J. H.; Kim, Y. M.; Jeong, H. J.; Kim, D. W.; Park, K. H.; Kwon, H.-J.; Park, S.-J.; Lee, W. S.; Ryu, Y. B. Tanshinones as selective and slow-binding inhibitors for SARS-CoV cysteine proteases. *Bioorg. Med. Chem.* **2012**, *20*, 5928–5935.

(126) Chen, L.; Li, J.; Luo, C.; Liu, H.; Xu, W.; Chen, G.; Liew, O. W.; Zhu, W.; Puah, C. M.; Shen, X.; Jiang, H. Binding interaction of quercetin-3- $\beta$ -galactoside and its synthetic derivatives with SARS-CoV 3CLpro: structure-activity relationship studies reveal salient pharmacophore features. *Bioorg. Med. Chem.* **2006**, *14*, 8295–8306.

(127) Kuo, C.-J.; Liu, H.-G.; Lo, Y.-K.; Seong, C.-M.; Lee, K.-I.; Jung, Y.-S.; Liang, P.-H. Individual and common inhibitors of coronavirus and picornavirus main proteases. *FEBS Lett.* **2009**, *583*, 549–555.

(128) Martina, E.; Stiefl, N.; Degel, B.; Schulz, F.; Breuning, A.; Schiller, M.; Vicik, R.; Baumann, K.; Ziebuhr, J.; Schirmeister, T. Screening of electrophilic compounds yields an aziridinyl peptide as

new active-site directed SARS-CoV main protease inhibitor. *Bioorg. Med. Chem. Lett.* **2005**, *15*, 5365–5369.

(129) Hamill, P.; Hudson, D.; Kao, R. Y.; Chow, P.; Raj, M.; Xu, H.; Richer, M. J.; Jean, F. Development of a red-shifted fluorescence-based assay for SARS-coronavirus 3CL protease: identification of a novel class of anti-SARS agents from the tropical marine sponge *Axinella corrugata*. *Biol. Chem.* **2006**, *387*, 1063–1074.

(130) Liu, Y.-C.; Huang, V.; Chao, T.-C.; Hsiao, C.-D.; Lin, A.; Chang, M.-F.; Chow, L.-P. Screening of drugs by FRET analysis identifies inhibitors of SARS-CoV 3CL protease. *Biochem. Biophys. Res. Commun.* **2005**, *333*, 194–199.

(131) Goetz, D.; Choe, Y.; Hansell, E.; Chen, Y.; McDowell, M.; Jonsson, C.; Roush, W.; McKerrow, J.; Craik, C. Substrate specificity profiling and identification of a new class of inhibitor for the major protease of the SARS coronavirus. *Biochemistry* **2007**, *46*, 8744–8752.

(132) Xue, X.; Yang, H.; Shen, W.; Zhao, Q.; Li, J.; Yang, K.; Chen, C.; Jin, Y.; Bartlam, M.; Rao, Z. Production of authentic SARS-CoV Mpro with enhanced activity: application as a novel tag-cleavage endopeptidase for protein overproduction. *J. Mol. Biol.* **2007**, *366*, 965–975.

(133) Kao, R. Y.; To, A. P.; Ng, L. W.; Tsui, W. H.; Lee, T. S.; Tsoi, H.-W.; Yuen, K.-Y. Characterization of SARS-CoV main protease and identification of biologically active small molecule inhibitors using a continuous fluorescence-based assay. *FEBS Lett.* **2004**, *576*, 325–330.

(134) Chen, C.-N.; Lin, C. P.; Huang, K.-K.; Chen, W.-C.; Hsieh, H.-P.; Liang, P.-H.; Hsu, J. T.-A. Inhibition of SARS-CoV 3C-like protease activity by theaflavin-3, 3'-digallate (TF3). *Evid. Based Complementary Altern. Med.* **2005**, *2*, 209–215.

(135) Karypidou, K.; Ribone, S. R.; Quevedo, M. A.; Persoons, L.; Pannecouque, C.; Helsen, C.; Claessens, F.; Dehaen, W. Synthesis, biological evaluation and molecular modeling of a novel series of fused 1, 2, 3-triazoles as potential anti-coronavirus agents. *Bioorg. Med. Chem. Lett.* **2018**, *28*, 3472–3476.

(136) Baker, J. D.; Uhrich, R. L.; Kraemer, G. C.; Love, J. E.; Kraemer, B. C. A drug repurposing screen identifies hepatitis C antivirals as inhibitors of the SARS-CoV2 main protease. *PLoS One* **2021**, *16*, e0245962.

(137) Tripathi, P. K.; Upadhyay, S.; Singh, M.; Raghavendhar, S.; Bhardwaj, M.; Sharma, P.; Patel, A. K. Screening and evaluation of approved drugs as inhibitors of main protease of SARS-CoV-2. *Int. J. Biol. Macromol.* **2020**, *164*, 2622–2631.

(138) Zhang, J.; Huitema, C.; Niu, C.; Yin, J.; James, M. N.; Eltis, L. D.; Vederas, J. C. Aryl methylene ketones and fluorinated methylene ketones as reversible inhibitors for severe acute respiratory syndrome (SARS) 3C-like proteinase. *Bioorg. Chem.* **2008**, *36*, 229–240.

(139) Chen, L.; Gui, C.; Luo, X.; Yang, Q.; Günther, S.; Scandella, E.; Drost, C.; Bai, D.; He, X.; Ludewig, B.; Chen, J.; Luo, H.; Yang, Y.; Yang, Y.; Zou, J.; Thiel, V.; Chen, K.; Shen, J.; Shen, X.; Jiang, H. Cinanserin is an inhibitor of the 3C-like proteinase of severe acute respiratory syndrome coronavirus and strongly reduces virus replication in vitro. *J. Virol.* **2005**, *79*, 7095–7103.

(140) Tsai, K.-C.; Chen, S.-Y.; Liang, P.-H.; Lu, I.-L.; Mahindroo, N.; Hsieh, H.-P.; Chao, Y.-S.; Liu, L.; Liu, D.; Lien, W.; Lin, T.-H.; Wu, S.-Y. Discovery of a novel family of SARS-CoV protease inhibitors by virtual screening and 3D-QSAR studies. *J. Med. Chem.* **2006**, *49*, 3485–3495.

(141) Kao, R. Y.; Tsui, W. H.; Lee, T. S.; Tanner, J. A.; Watt, R. M.; Huang, J.-D.; Hu, L.; Chen, G.; Chen, Z.; Zhang, L.; He, T.; Chan, K.-H.; Tse, H.; To, A. P.; Ng, L. W.; Wong, B. C.; Tsoi, H.-W.; Yang, D.; Ho, D. D.; Yuen, K.-Y. Identification of novel small-molecule inhibitors of severe acute respiratory syndrome-associated coronavirus by chemical genetics. *Chem. Biol.* **2004**, *11*, 1293–1299.

(142) Ramajayam, R.; Tan, K.-P.; Liu, H.-G.; Liang, P.-H. Synthesis and evaluation of pyrazolone compounds as SARS-coronavirus 3C-like protease inhibitors. *Bioorg. Med. Chem.* **2010**, *18*, 7849–7854.

(143) Yoshizawa, S.-i.; Hattori, Y.; Kobayashi, K.; Akaji, K. Evaluation of an octahydroisochromene scaffold used as a novel SARS 3CL protease inhibitor. *Bioorg. Med. Chem.* **2020**, *28*, 115273.

(144) Shimamoto, Y.; Hattori, Y.; Kobayashi, K.; Teruya, K.; Sanjoh, A.; Nakagawa, A.; Yamashita, E.; Akaji, K. Fused-ring structure of

decahydroisoquinolin as a novel scaffold for SARS 3CL protease inhibitors. *Bioorg. Med. Chem.* **2015**, *23*, 876–890.

(145) Gurard-Levin, Z. A.; Liu, C.; Jekle, A.; Jaisinghani, R.; Ren, S.; Vandyck, K.; Jochmans, D.; Leyssen, P.; Neyts, J.; Blatt, L. M.; Beigelman, L.; Symons, J. A.; Raboisson, P.; Scholle, M. D.; Deval, J. Evaluation of SARS-CoV-2 3C-like protease inhibitors using self-assembled monolayer desorption ionization mass spectrometry. *Antiviral Res.* **2020**, *182*, 104924.

(146) Hanh Nguyen, T. T.; Ryu, H.-J.; Lee, S.-H.; Hwang, S.; Breton, V.; Rhee, J. H.; Kim, D. Virtual screening identification of novel severe acute respiratory syndrome 3C-like protease inhibitors and in vitro confirmation. *Bioorg. Med. Chem. Lett.* **2011**, *21*, 3088–3091.

(147) Mukherjee, P.; Desai, P.; Ross, L.; White, E. L.; Avery, M. A. Structure-based virtual screening against SARS-3CLpro to identify novel non-peptidic hits. *Bioorg. Med. Chem.* **2008**, *16*, 4138–4149.

(148) Wen, C.-C.; Kuo, Y.-H.; Jan, J.-T.; Liang, P.-H.; Wang, S.-Y.; Liu, H.-G.; Lee, C.-K.; Chang, S.-T.; Kuo, C.-J.; Lee, S.-S.; Hou, C.-C.; Hsiao, P.-W.; Chien, S.-C.; Shyur, L.-F.; Yang, N.-S. Specific plant terpenoids and lignoids possess potent antiviral activities against severe acute respiratory syndrome coronavirus. *J. Med. Chem.* **2007**, *50*, 4087–4095.

(149) He, Z.; Zhao, W.; Niu, W.; Gao, X.; Gao, X.; Gong, Y.; Gao, X. Molecules inhibit the enzyme activity of 3-chymotrypsin-like cysteine protease of SARS-CoV-2 virus: the experimental and theory studies. *bioRxiv* **2020**, DOI: [10.1101/2020.05.28.120642](https://doi.org/10.1101/2020.05.28.120642).

(150) Verschueren, K. H.; Pumpor, K.; Anemüller, S.; Chen, S.; Mesters, J. R.; Hilgenfeld, R. A structural view of the inactivation of the SARS coronavirus main proteinase by benzotriazole esters. *Chem. Biol.* **2008**, *15*, 597–606.

(151) Du, R.; Cooper, L.; Chen, Z.; Lee, H.; Rong, L.; Cui, Q. Discovery of Chebulagic Acid and Punicalagin as Novel Allosteric Inhibitors of SARS-CoV-2 3CLpro. *Antiviral Res.* **2021**, *190*, 105075.

(152) Rizzuti, B.; Grande, F.; Conforti, F.; Jimenez-Alesanco, A.; Ceballos-Laita, L.; Ortega-Alarcon, D.; Vega, S.; Reyburn, H. T.; Abian, O.; Velazquez-Campoy, A. Rutin Is a Low Micromolar Inhibitor of SARS-CoV-2 Main Protease 3CLpro: Implications for Drug Design of Quercetin Analogs. *Biomedicines* **2021**, *9*, 375.

(153) Abian, O.; Ortega-Alarcon, D.; Jimenez-Alesanco, A.; Ceballos-Laita, L.; Vega, S.; Reyburn, H. T.; Rizzuti, B.; Velazquez-Campoy, A. Structural stability of SARS-CoV-2 3CLpro and identification of quercetin as an inhibitor by experimental screening. *Int. J. Biol. Macromol.* **2020**, *164*, 1693–1703.

(154) Alhakamy, N. A.; Ahmed, O. A.; Ibrahim, T. S.; Aldawsari, H. M.; Eljaaly, K.; Fahmy, U. A.; Alaofi, A. L.; Caraci, F.; Caruso, G. Evaluation of the Antiviral Activity of Sitagliptin-Glatiramer Acetate Nano-Conjugates against SARS-CoV-2 Virus. *Pharmaceuticals* **2021**, *14*, 178.

(155) Abdallah, H. M.; El-Halawany, A. M.; Sirwi, A.; El-Araby, A. M.; Mohamed, G. A.; Ibrahim, S. R.; Koshak, A. E.; Asfour, H. Z.; Awan, Z. A.; Elfaky, M. A. Repurposing of some natural product isolates as SARS-COV-2 main protease inhibitors via in vitro cell free and cell-based antiviral assessments and molecular modeling approaches. *Pharmaceuticals* **2021**, *14*, 213.